BOSE-EINSTEIN CONDENSATION AND QUANTIZED FLOW OF MICROCAVITY POLARITONS WITH LONG LIFETIME

by

Gangqiang Liu

B. S., Physics, Wuhan University, 2008

M. S., Physics, University of Pittsburgh, 2011

Submitted to the Graduate Faculty of

the Kenneth P. Dietrich School of Arts and Sciences in partial fulfillment

of the requirements for the degree of

Doctor of Philosophy

University of Pittsburgh

2015

UNIVERSITY OF PITTSBURGH

DEPARTMENT OF PHYSICS AND ASTRONOMY

This dissertation was presented

by

Gangqiang Liu

It was defended on

September 24th 2015

and approved by

David W. Snoke, Physics and Astronomy

Andrew Daley, Physics and Astronomy

Gurudev Dutt, Physics and Astronomy

Tao Han, Physics and Astronomy

David Waldeck, Chemistry

Dissertation Director: David W. Snoke, Physics and Astronomy

BOSE-EINSTEIN CONDENSATION AND QUANTIZED FLOW OF MICROCAVITY POLARITONS WITH LONG LIFETIME

Gangqiang Liu, PhD

University of Pittsburgh, 2015

Over the last two decades, the system of exciton-polaritons (polaritons) in a semiconductor microcavity has become an important platform for studying the physics of quantum fluids in a solid-state system. Polaritons are formed by the strong coupling between photons and a sharp electronic resonance (e.g. an exciton resonance) in a cavity. They are interacting bosonic particles with a small effective mass due to their half-light and half-matter nature. Spontaneous coherence phenomena, such as the superfluid transition and Bose-Einstein condensation (BEC), have been observed in polariton systems at temperatures in the range from several Kelvin to room temperature. This dissertation focuses on new methods of trapping polaritons and the BEC and superfluidity of polaritons in these new traps. The first part of this dissertation describes experiments on trapping polaritons with an optically generated potential barrier. When the polariton density increases, there is a transition from ballistic motion to coherent motion of polaritons over hundreds of micrometers. At even higher particle density, there is a very sharp transition from the coherent motion state to the ground state of the trap. The second part of this dissertation explores the superfluid properties of polaritons in a ring-shaped trap. This ring trap is formed by combining a stress-induced harmonic trap with an optically created barrier at the trap center. This trapping method enables fine control of the trap profile as well as the properties of the polaritons in the trap. The formation of a polariton ring condensate is observed in this trap. The phase and polarization measurement of the ring condensate reveals that it is in a half-quantized circulation state which features a phase shift of π and a polarization vector rotation of π of the polari-

tons around a closed path in the ring. The direction of the circulation of the flow around the ring fluctuates randomly between clockwise and counter-clockwise from one shot to the next. In contrast, the rotation of the polarization of polaritons is very stable. This property is experimentally studied, and it is found that the stable spatial polarization pattern may relate to the optical spin Hall effect.

Keywords: Microcavity Polaritons, Bose-Einstein Condensation, Exciton Barrier, Stress Trap, Ring Trap, Quantized Flow.

TABLE OF CONTENTS

1.0 INTRODUCTION 1

1.1 Overview 1

1.2 Outline of the Thesis 3

1.3 List of Publications 4

2.0 MICROCAVITY POLARITONS 5

2.1 Excitons in Semiconductors 5

2.1.1 Excitons in bulk semiconductor 5

2.1.2 Excitons in quantum well 9

2.2 Semiconductor Microcavity 11

2.3 Microcavity Exciton-Polaritons 13

2.3.1 Strong coupling of excitons and photons in a microcavity 13

2.3.2 Important Properties of Exciton-Polariton 15

2.4 Bose-Einstein Condensation and Superfluid 17

2.4.1 Bose-Einstein Condensation 17

2.4.2 Superfluid and Vortices 21

2.4.3 BEC of Polaritons and the Generalized Gross-Pitaevskii Equation 23

3.0 MICROCAVITY SAMPLE AND EXPERIMENTAL METHODS . . 25

3.1 Long-lifetime Polariton Sample 25

3.1.1 Properties of the Sample 25

3.1.2 Dislocations in the Long-Lifetime Polariton Sample 28

3.2 Creating Polaritons with Optical Excitation 33

3.3 Optical Detection of Polaritons 36

3.3.1 Real space spectroscopy . . . 36
3.3.2 Momentum space spectroscopy . . . 38
3.3.3 Coherence Measurement . . . 40
3.4 Stress Trap for Polaritons . . . 44
3.4.1 Background Physics of Stress Trapping . . . 44
3.4.2 Advantages of Stress Trapping . . . 46
3.5 Exciton Barrier for Polaritons . . . 52
4.0 COHERENT FLOW AND BEC OF POLARITONS WITH LONG LIFETIME . . . 56
4.1 Experimental Method . . . 57
4.2 Ballistic Motion of Polaritons Over Macroscopic Distance . . . 57
4.3 Transition to Coherent Flow . . . 62
4.4 Sharp Transition to Trapped State . . . 66
5.0 CONDENSATION OF POLARITONS IN A RING TRAP . . . 68
5.1 Creating Ring Trap for Polaritons . . . 69
5.2 Early Attempts to Create Polariton Ring Condensate . . . 73
5.2.1 Polaritons in a Deep Ring Trap . . . 73
5.2.2 Polaritons in a Shallow Ring Trap . . . 82
5.3 Observation of a Polariton Ring Condensate . . . 86
6.0 HALF-QUANTUM CIRCULATION OF POLARITON RING CONDENSATE . . . 91
6.1 Circulation in the Ring Condensate . . . 92
6.2 Polarization Rotation of the Ring Condensate . . . 92
6.3 Half-Quantized Circulation State of the Ring Condensate . . . 98
6.4 Momentum-Space Images of the Ring Condensate . . . 101
7.0 EXPERIMENTAL STUDY ON THE ORIGIN OF THE STABLE POLARIZATION PATTERN . . . 106
7.1 Stable Polarization Pattern in the Ring Trap . . . 106
7.1.1 Effect of the Lattice Pinning . . . 108
7.1.2 Effect of the Pump Laser Polarization . . . 108

7.1.3 Effect of the Polariton Density Variation . . . 110
7.2 A Possible Mechanism for the Polarization Pattern . . . 112
7.2.1 Optical Spin Hall Effect . . . 112
7.2.2 Optical Spin Hall Effect In the Ring Trap . . . 113
8.0 CONCLUSION AND FUTURE DIRECTIONS . . . 122
8.1 Conclusion . . . 122
8.2 Future Directions . . . 124
8.2.1 Time Resolving the Jump of the Flow Direction of the Ring Condensate . . . 124
8.2.2 Generating Quantized Circulation State on Demand . . . 124
APPENDIX A. DEPHASING OF A CLOSED INTERACTING MANY-BODY SYSTEM . . . 128
A.1 Summary of the Quantum Boltzmann Equation . . . 129
A.2 Irreversibility in Quantum Boltzmann Equation and Dephasing . . . 131
A.2.1 Irreversibility in Quantum Boltzmann Equation . . . 131
A.3 Calculation of the Off-Diagonal Time Evolution . . . 133
A.3.1 Zero-Order Off-Diagonal Evolution . . . 135
A.3.2 First-Order Off-Diagonal Evolution . . . 135
A.3.3 Second-Order Off-Diagonal Evolution . . . 137
A.3.4 Summary of Dephasing Calculation Results . . . 141
APPENDIX B. INTENSITY STABILIZED TI:SAPPHIRE LASER WITH FEEDBACK FROM A GRATING . . . 142
APPENDIX C. NUMERICAL METHOD OF RETRIEVING THE PHASE OF RING CONDENSATE FROM INTERFERENCE PATTERN . . . 147
BIBLIOGRAPHY . . . 149

LIST OF FIGURES

1 Exciton in Direct Band Gap Semiconductor 6
2 Band Structure of GaAs and Corresponding Optical Transitions 8
3 Quantum Well 10
4 Semiconductor Microcavity 12
5 Dispersion of Polaritons at Different Detunings 16
6 Long-Lifetime Microcavity Sample 26
7 Cavity Thickness Gradient 29
8 Lower Polariton Dispersion at Different Locations on Sample 30
9 Misfit Dislocations in Long-Lifetime Sample 31
10 Trapping of Polaritons by Misfit Dislocations in Long-Lifetime Sample 32
11 Resonant and Non-Resonant Pumping Methods 34
12 Real-Space Imaging Setup 37
13 Real-Space Image and Energy of Polaritons 38
14 Momentum-Space Imaging Setup 39
15 2D and Energy-Resolve Momentum-Space Image of Polaritons 40
16 Coherence Time Measurement Setup and Typical Data 41
17 Coherence Length Measurement Setup and Typical Data 42
18 Setup for Stress Trapping 47
19 Calculated Exciton Energy and Polaritons Energy under Stress 48
20 Experimental Stress Trap Profile 49
21 Momentum-Space image of Polaritons Before and After Stress Applied 49
22 Temperature of Polaritons in the Stress Trap 50

23 Polarization Splitting in Stress Trap 53
24 Exciton Barrier for Polaritons 54
25 Real- and Momentum-Space Images of the Ballistic Motion of Polaritons . . . 58
26 Momentum-Space Evolution of Polariton States 59
27 Real- and Momentum-Space images of the Coherent Flow of Polaritons 63
28 Coherence Measurement of Flowing Polaritons 65
29 Real- and Momentum-Space Images of Trapped polaritons 67
30 Illustration of a Ring Trap 70
31 Stress Trap and Ring Trap 71
32 Energy of Polaritons in the Stress Trap 74
33 Real-Space Image and Energy of Polaritons at Different Pump Powers in the Ring Trap 75
34 Energy of Polaritons at Different Parts of the Ring 76
35 Spatial Coherence Measurement and Data of The Ring Condensate 78
36 Time Evolution of Laser Intensity 80
37 Polariton Ring Cloud and Its Interference Pattern Generated by the Intensity Stabilized Laser 80
38 Ring Trap at New Location 83
39 Harmonic Osicllator States of Polaritons in the Stress Trap 84
40 Real-Space Images and Energy of Polaritons in the Ring Trap Below and Above the Condensation Threshold. 88
41 Energy of Polaritons at Different Parts of the Ring 89
42 Spatial Coherence Measurement of the Ring Condensate 90
43 Interference Patterns of the Ring Condensate 93
44 Polarization Resolved Real-Space Image of the Ring Condensate and the Measured Stokes Parameters 95
45 Polarization Pattern of the Ring Condensate 96
46 Polarization Patter and Interference Pattern Predicted by the Theory 99
47 Momentum-Space Images of Polaritons in the Ring Trap at Different Pump Powers 102

48 Schematic of the Profile of the Ring trap and the Trapping of Polaritons . . . 103
49 Polarization of Ring Condensates Created by Lasers with Different Polarizations 107
50 Polarization Map of a Ring Condensate and a Condensate that Fills Part of the Ring Trap . . . 111
51 Effective Magnetic Field in Optical Spin Hall Effect . . . 114
52 Simulated Circular Polarization Degree in Momentum- and Real-Space . . . 115
53 Polarization of Polaritons at the Pump Spot . . . 117
54 Average Polarization in the Ring Trap at Different Pump Powers . . . 119
55 Polarization of Polaritons in the Ring Trap for Different Pump Powers . . . 120
56 Time Resolving the Jump of the Circulation Direction . . . 125
57 Methods of Generating Quantized Flow State on Demand . . . 127
58 Homemade CW Ti:Sapphire Laser . . . 144
59 Grating Feedback for Stabilizing the Laser Intensity . . . 145
60 Procedure of Retrieving Phase from Interference Pattern . . . 148

ACKNOWLEDGEMENT

When looking back on my graduate study and life in the past six years, I feel grateful to many wonderful people. First of all, I would like to thank my advisor David Snoke. I thank him for his consistent support over the last five years and the guidance, inspiration and encouragement that he gave to me. He gave me the freedom to work on the things that are most interesting to me, and to work in a style that I am most comfortable with. He was always there whenever I need suggestions on problems in my experiments or the understanding of a textbook sentence. Most of the time, our conversation would evolve from a particular question into a discussion on the research directions that relate to the question. My knowledge and understanding of the current frontiers of physics are mostly from such conversations. I thank him for giving me extremely valuable advices when I need to make important decisions in my career. I also want to thank him for the movie night discussions he organized which covered a wild range of topics such as history, philosophy, human civilization and so on. Those discussions enriched me intellectually.

I thank Andrew Daley for being my mentor and friend since 2011. He ignited my enthusiasm in quantum optics by a fantastic series of lectures in the spring of 2011. I thank him for introducing me the wonderful DAMOP meetings and the AMO community. I am very impressed by the competition and friendship between top researchers in this community. This sets the standard and guideline for my own career. I thank him for the invitation and arrangements he made for my visit to the Department of Physics and Astronomy at the University Strathclyde. It was a great experience. I thank him for all the advices and encouragements over the years.

I thank my other committee members – Tao Han, Gurudev Dutt, David Waldeck and Christina Woods – for monitoring my progress and providing critical feedbacks. I thank them for being very responsive and encouraging over the years. Many of my PhD friends and colleagues have complained to me about how difficult it was for them to schedule meetings with their committees. I am really lucky that I did not have such a problem. I thank the committee for carefully reading my thesis and helping me make revisions.

I am very grateful to both the former and current members of our lab. I thank Botao

Zhang for teaching me how to build a Ti:Sapphire laser. The joy and the feeling of fulfillment I obtained from this experience ensured me that I can be a experimental physicist. I also thank him for teaching me how to work intelligently and efficiently. I thank Bryan Nelsen for designing the long-lifetime polariton sample that I used for my thesis. I also thank him for writing the software 'BryanSpec' for the polariton experiments. All the data in my thesis was taken with this software. I was and am still impressed by the vast knowledge that Bryan has. From him, I learnt many tricks of doing electronics and machine shop. I thank Nicholas Sinclair and Jeffery Wenschell for their assistance and patience whenever I have questions about exctions. I thank Mark Steger for designing the sample holder that I used in my experiments. Mark gave me numerous suggestions on my experiments over the years. He helped me identifying loopholes in my experiment design and data analysis. I thank Chitra Gautham for her help of the course works and experiments. Most importantly, I thank her for her cheerful spirit, which brought a lot joy into our lab. I thank David Meyers and Jonathan Beaumariage for their assistance in the experiments.

Without the high quality of the long-lifetime polariton sample, it will be impossible for me to observe all the interesting phenomena, which will be presented in this thesis. Therefore, I would like to thank our sample grower – Loren Pfeiffer and Kenneth West – for their extraordinary work.

I also want to thank the people in the main office of the Physics department. In particular, I want to thank our graduate secretary Leyla Hirschfeld for keeping me on track of all the administrative things. Thanks to Leyla's emails, phone calls and summons on various deadlines, I was able to maintain my status as a registered student of the university and avoid depleting my bank account by the late fees. I also want to thank our department buyer Laura Provolt for ordering various things for our lab. I cannot remember how many times Laura helped me order liquid helium after the normal hours. My appreciation extends to all the staff members of the Physics department. Your efforts kept me away from the daily distractions and provided a very nice working environment to me in the past six years.

I want to thank my friends for their support over the years. I thank Hejun Xiong, Xiaochuan Tang, Xiang Zhou, Zhuoran Liu, Baiyu Li, Dongdong Li, Xiben Li, Xiong Zhang, Qi Zhang for being very supportive to me. Last but not least, I want to thank my family for

their unconditional love, support and understanding. I want to thank my parents for their love and support since I was born. Being farmers from a less developed region in China, my parents had to work extremely hard to support my education over the years. It is their hard work and encouragement make it possible for me to pursuit my dream and live a happy life. I thank them for their constant support and the optimistic attitude that I inherit from them. I want to thank my wife Lujia for bringing me love and a wonderful life. For some mysterious reasons, I started to have better luck in my research since we started spending time together. My first paper on polaritons was accepted when we were traveling together for the first time. In the last two years, when I had to run overnight experiments, she would come to deliver food to me in the evenings and drive me back when I was done in the early mornings. She always has confidence in me even when I started to double myself. I thank her for her unconditional support. I also want to thank our daughter who will come to this world by the end of this year. I thank her for being healthy, therefore I can focus on the writing of this thesis over the last few months.

I thank all the people who have helped me to accomplish this great endeavor!

1.0 INTRODUCTION

1.1 OVERVIEW

Bose-Einstein condensation (BEC), predicted by Einstein in 1925 [1], is at the heart of our current understanding of some of the most fascinating phenomena in quantum many-body physics. For example, the superconductivity of conventional superconductors is explained by the Bose-Einstein condensation of electron pairs [2, 3]. Bose-Einstein condensation is also responsible for the superfluid behaviors of ^{4}He below the λ point [4, 5]; this connection, suggested by London in 1938, has became the basis of our current understanding of superfluid [6] . However, the first direction observation of Bose-Einstein condensation only becomes available in 1995 when physicists were able to cool alkali atoms down to 10^{-9} K above absolute zero. Since then, Bose-Einstein condensation has become the subject of an explosion of research. Currently, it has evolved into a field that combines atomic physics, condensed matter physics and quantum optics.

In the mean time, great efforts have been devoted to the pursuit of Bose-Einstein condensation in solid state systems, such as excitons in semiconductors [7, 8, 9, 10, 11, 12], and exciton-polaritons in semiconductor microcavities [13, 14, 15, 17]. Clear evidence of BEC in solid state systems was first observed in 2006 and 2007 in exciton-polariton systems [15, 17]. The exciton-polaritons are superpositions of quantum-well excitons and photons in a semiconductor microcavity [18, 19]. The photon component of a polariton gives it a very small effective mass, on the order of 10^{-4} of the free electron mass. Therefore, polaritons can reach the Bose-Einstein condensation threshold at temperatures in the range from several Kelvin to room temperature [15, 16, 17]. The exciton component of polaritons leads to interaction between polaritons, as well as interactions with excitons and lattice phonons. These

interactions are crucial for the thermalization of polaritons; they also allow the possibility of manipulating polaritons through their interaction with excitons [20, 21, 22, 23].

Polaritons have finite lifetimes, typically on the order of a few picoseconds [13, 14, 15, 17], due to the leakage of photons into the environment outside the microcavity. Both the particle-particle interaction strength and the lifetime of a polariton can be tuned by changing the exciton fraction of the polariton. It has been shown that when the exciton fraction is large enough, polaritons can reach thermal equilibrium with each other [25]. When the exciton fraction is small, polaritons behave like photons and are unable to thermalize with each other. Therefore, by changing the exciton fraction of a polariton, the system can be tuned into or out of equilibrium. This provides unique opportunities for studying a wide range of interesting questions of Bose-Einstein condensation.

Over the last few years, superfluid behavior of polaritons has been extensively studied [26, 27, 28, 29, 31, 32, 33, 34]. Frictionless flow of polaritons is observed when the flow velocity is below a critical velocity [27, 28]. As the flow velocity goes above the critical velocity, excitations in the form of vortex and anti-vortex pairs are observed [26, 29, 33]. These works proved the existence of vortices in polariton superfluid, but they have not demonstrated the ability of controlling the vortices. In experiments reported in Refs. [26, 29], the vortices are randomly generated by polariton flow against defects in the sample. In this case, both the handedness and the position of the vortices are pinned by the defects. On the other hand, when there are many fewer defects in the sample, which is the case in Refs. [31, 33], vortices drift randomly with high speed in the polariton fluid. None of these works show any control of the vortices.

It is the goal of this thesis to develop methods for generating and manipulationg polariton superfluids in a controlled manner. In order to do so, we created a ring-shaped trap for polaritons by combining an optically generated potential barrier and a stress-induced harmonic trap. Above a critical density, a ring-shaped polariton condensate is formed in this trap, and it circulates around with a quantized angular momentum. By measuring the phase and polarization of the condensate, it is found that the polaritons are in a state with half-integer angular momentum and a π rotation of its spin. It is also found that the flow direction of the polaritons in the ring fluctuates randomly between clockwise and counterclockwise. In

contrast, the spatial spin pattern is very stable. These properties are experimentally studied, and there is evidence showing that they are related to the optical spin Hall effect [122].

1.2 OUTLINE OF THE THESIS

- In Chapter 2, I introduce the background physics of microcavity exciton-polaritons, including the concepts of excitons in semiconductors, microcavity photons, and the strong coupling regime of exciton-photon interaction. The concept of Bose-Einstein condensate is also discussed.
- In Chapter 3, I describe the long-lifetime polariton sample and the experimental methods. We introduce the experiment setup for real-space and momentum-space imaging, as well as the coherence measurement. The method of trapping polaritons with stress and with an exciton barrier are also explained.
- In Chapter 4, I present experimental data with the long-lifetime polaritons in an optically generated quasi-1D trap. The polaritons exhibits very interesting dynamics at different particle densities. When the density is above a critical value, a BEC of polaritons is formed in the quasi-1D trap created by the exciton barrier and the potential slope due to the cavity-width gradient.
- In Chapter 5, I discuss the method of creating a ring-shaped trap for polaritons. I also present and analyze the results of my early attempts to create a ring condensate of polaritons with long lifetime. The important implications of these results are also discussed. I present the experiment in which a fully coherent ring condensate of long-lifetime polaritons is created.
- In Chapter 6, I present a quantitative analysis of the interference pattern and the polarization pattern of the ring condensate. It is found that the ring condensate is in a new type of quantized flow state which features a half integer angular momentum and a flip of the spin of the polaritons from one side of the ring to the other side of the ring.
- In Chapter 7, I describe experimental investigations into the mechanism responsible for the stable polarization pattern of the ring condensate. We found that it is very likely

related to the optical spin Hall effect.

- In Chapter 8, I give the conclusion for the experiments discussed in this thesis, and discuss our thoughts on future experiments.
- In Appendix A, I present my work on a theoretical study of the decoherence in a many-body system. We have shown that the phase coherence is lost in a closed many-body system due to particle scatterings, except in the case of a boson gas near condensation.
- In Appendix B, I describe the grating feedback method that I used to stabilized the output power of the homemade Ti:Sapphire laser.
- In Appendix C, I explain the numerical method that I used to retrieve the phase of the ring condensate from the interference pattern.

1.3 LIST OF PUBLICATIONS

The work presented in this thesis has been published in several research articles, here is a list of them:

1. "Dissipationless flow and sharp threshold of a polariton condensate with long lifetime," Physical Review X **3**, 041015 (2013). The results that will be shown in Chapter 4 are published in this article.
2. "Long-range ballistic motion and coherent flow of long-lifetime polaritons," Physical Review B **88**, 235314 (2013). Part of the results in Chapter 4 are published in this article.
3. "A new type of half-quantum flow in a macroscopic polariton spinor ring condensate," Proceedings of the National Academy of Science of the United States of American, **112**, 2676 (2015). The results that will be presented in Chapter 5 and Chapter 6 are published in this article.
4. "The basis of the Second Law of thermodynamics in quantum field theory," Annals of Physics **327(7)**, 1825 (2012). The results that will be presented in Appendix A are published in this article.

2.0 MICROCAVITY POLARITONS

2.1 EXCITONS IN SEMICONDUCTORS

2.1.1 Excitons in bulk semiconductor

In a semiconductor, when an electron is excited from the valence band into the conduction band it leaves a vacancy in the valence band (Fig. 1). This vacancy can be treated as a positively charged particle in the valence band, which is known as a hole. When the energy of the electron and hole is low enough, they can form a bound state through Coulomb attraction. This bound electron-hole pair is called an exciton. In semiconductor crystals, excitons typically have a size of the order of tens of lattice sites and are often referred to as Wannier-Mott excitons [36, 37]. In a Wannier-Mott exciton, the electron and hole orbit each other analogous to the electron and proton in a hydrogen atom. The Schrödinger equation for the wavefunction $f(\rho)$ of the relative motion between electron and hole of a Wannier-Mott exciton is [38]:

$$-\frac{\hbar^2}{2m_{ex}}\nabla^2 f(\rho) - \frac{e^2}{4\pi\epsilon\epsilon_0\rho}f(\rho) = Ef(\rho) \tag{2.1}$$

where $m_{ex} = m_e m_h/(m_e + m_h)$ is the effective mass of exciton, m_e and m_h are the effective masses of electron and hole, and $\rho = |\vec{r}_e - \vec{r}_h|$ is the distance between the electron and hole. Eq. (2.1) has the same form as the Schrödinger equation for the hydrogen atom. Its solutions therefore have the same form as that of the hydrogen atom. For example, the wavefunction of the ground state of the exciton is:

$$f_1 = \frac{1}{\sqrt{\pi a_{ex}^3}} e^{-\rho/a_{ex}}, \tag{2.2}$$

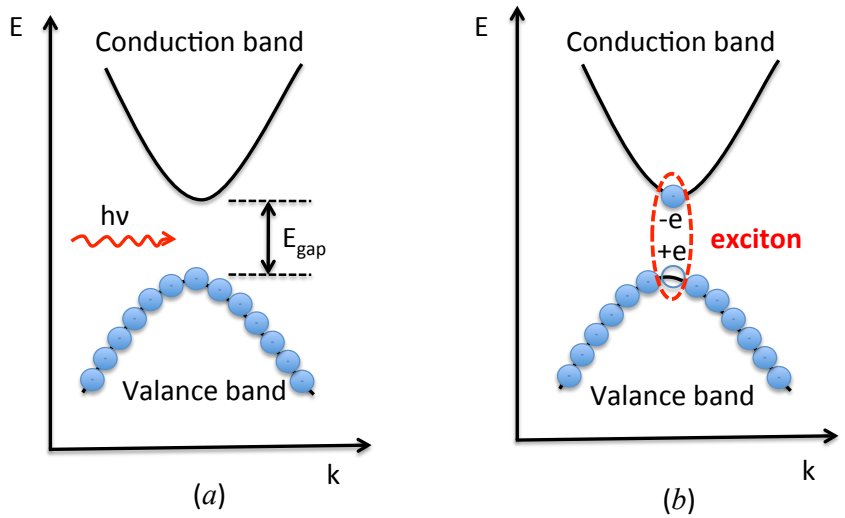

Figure 1: Schematic of an exciton created by absorbing a photon in a direct band gap semiconductor near zone center. (a) The ground state of the system as the valence band is fully occupied and the conduction band is empty; E_{gap} is band gap energy. Electrons can be excited from the valence band into the conduction band, for example by absorbing photons with energy $h\nu \geq E_{gap}$. (b) An electron is excited into the conduction band. It leaves a vancancy (hole) in the conduction band, with is positively charged. When the energy of the electron and the hole is low enough, they can form a bound pair due to Coulomb attraction.

with a_{ex} the exciton Bohr radius given by:

$$a_{ex} = \frac{4\pi\hbar^2\epsilon\epsilon_0}{m_{ex}e^2}. \tag{2.3}$$

The corresponding energy is:

$$E_1 = -\frac{m_{ex}}{2\hbar^2}(\frac{e^2}{4\pi\epsilon\epsilon_0})^2 = -\frac{\hbar^2}{2m_{ex}a_{ex}^2}. \tag{2.4}$$

The binding energy of the ground state exciton, therefore, is:

$$E_B = -E_1 = \frac{\hbar^2}{2m_{ex}a_{ex}^2}, \tag{2.5}$$

The total energy of the ground state exciton is:

$$E_{ex} = E_g - E_B + \frac{\hbar^2k^2}{2m_{ex}}. \tag{2.6}$$

with E_g the band gap energy, i.e. the minimum energy needed to excite an electron from the upper most valence band into the conduction band. Table 2.1.1 gives the band gap energies (E_g), electron mass (m_e), binding energies (E_B) and Bohr radii (a_{ex}) of Wannier-Mott excitons in several semiconductor materials [38].

Semiconductor crystal	E_g(eV)	$m_e(m_0)$	E_B(meV)	a_{ex}(Å)
GaAs	1.519	0.066	4.1	150
CdTe	1.606	0.089	10.6	80
InP	1.423	0.078	5.0	140
GaN	3.51	0.13	22.7	40

The electron and hole in an exciton form a dipole that can interact with the electromagnetic field. The strength of this interaction is described by the exciton oscillator strength F [39],

$$F = \frac{2m_{ex}\omega}{\hbar}|\langle u_c|\vec{x}|u_v\rangle|^2 \tag{2.7}$$

where ω is frequency of the electromagnetic field, $|u_v\rangle$ and $|u_c\rangle$ are the valence band and conduction band Bloch function, $\vec{x} = \vec{r}_h - \vec{r}_e$ is the displacement vector from the electron to the hole.

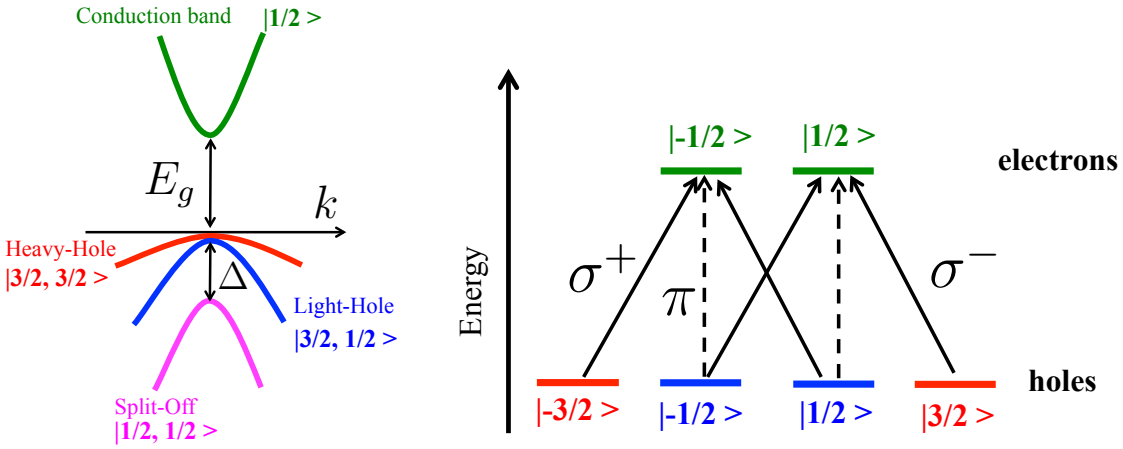

(a) (b)

Figure 2: Schematic band structure of GaAs and interband optical transitions near the zone center. (a) The conduction band (green) is s-like. The valence band is $p-$like; it splits into three sub-bands with different angular momentum due to spin-orbit coupling: (red) heavy-hole ($|3/2, 3/2\rangle$) band, (blue) light-hole ($|3/2, 1/2\rangle$) band and (purple) split-off band ($|1/2, 1/2\rangle$). Each of the three sub-bands is two-fold degenerate. The heavy-hole band and the light-hole band are degenerate at $k = 0$, with the split-off band being $\Delta = 0.34$ eV below them. (b) Band gap transitions in GaAs. Transitions represented by solid arrows involve circularly polarized light (σ^+, σ^-); the dashed arrows represent transitions that involve linearly polarized light (π).

In most III-V semiconductor materials, such as GaAs, the valence-band states have a p-state symmetry ($L = 1$). The spin-orbit coupling splits the valence band into several sub-bands with different total angular momentum and effective mass. In GaAs, the valence band splits into three sub-bands referred to as the heavy-hole, light-hole and spilt-off bands (see Fig. 2(a)). With the $|J, J_z\rangle$ notation, the heavy-hole states are $|3/2, \pm 3/2\rangle$, the light-hole states $|3/2, \pm 1/2\rangle$ and split-off states $|1/2, \pm 1/2\rangle$. In bulk GaAs, the heavy-hole and light-hole bands are degenerate at $k = 0$ while the split-off band is about 0.34 eV below them [40]. Therefore, only the heavy-hole and light-hole bands contribute to the interband optical transitions near the band gap (see Fig. 2(b)). The heavy hole couples more strongly to the light than the light holes due to a larger oscillator strength.

2.1.2 Excitons in quantum well

Artificial potentials for excitons can be created by growing heterostructures using different semiconductor materials. The band offsets at the interface between different materials create potentials for the electrons and holes. One of the simplest examples of a semiconductor heterostructure is the quantum well (QW), which is formed by placing a layer of material into another material with higher band gap energy. For example, in our sample the QW consists of a 70 Å GaAs ($E_g = 1.52$ eV) layer placed in between two 30Å AlAs ($E_g = 3.16$ eV) layers (Fig. 3). As the AlAs has a larger band gap, electrons and holes are trapped in the GaAs layer, as well as the excitons. The strong confinement along the growth direction of the QW leads to quantization of the motion of excitons along this direction. In the QW plane, however, excitons can move freely. If only one quantized state is concerned, usually the ground state, QW excitons behave like two-dimensional quasiparticles in the QW plane. The quantization of the exciton motion also lifts the degeneracy of the heavy-hole and light-hole states because they have different effective mass (Fig. 3(a)), and the ground state of excitons in the QW is the heavy-hole excitons in the 1s state.

The quantum confinement also changes the optical properties of excitons. In a QW, only the momentum in the QW plane needs to be conserved in an optical transition. Therefore, excitons in a QW can couple to photons with the same in-plane momentum and arbitrary

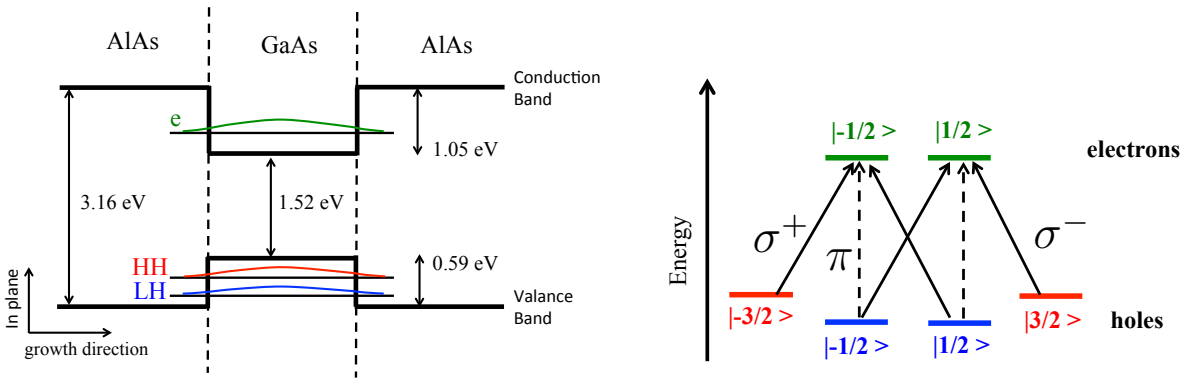

(a) (b)

Figure 3: Schematic GaAs/AlAs quantum well with the ground states of the electron and holes, and optical transitions inside the quantum well. Due to the quantum confinement, the degeneracy of the heavy hole (HH, red) and light hole (LH, blue) is lifted. The light hole is pushed to higher energy. (b) Interband optical transitions of GaAs quantum well. The transitions from heavy-hole band to the conduction band have lower energy than the light-hole to conduction band transition due to quantum confinement.

transverse momentum. In addition, due to the confinement, an exciton inside a QW has smaller Bohr radius, which leads to an enhancement of the oscillator strength. A smaller Bohr radius also gives an exciton higher binding energy. In an ideal 2D system, the binding energy of the ground state exciton is $E_B^{2D} = 4E_B$ with E_B the binding energy in 3D (see Eq. (2.5)) [38]. In practice, however, the binding energy is a function of the well width [41, 42, 43]. In our QW, the binding energy of the ground state exciton is about 10 meV. On the other hand, the energy difference between the first two quantized levels of a heavy-hole exciton in our QW is about 10 meV. Therefore, at a temperature of T $\sim$ 10K, we only need to be concerned about the the heavy-hole exciton 1s state.

2.2 SEMICONDUCTOR MICROCAVITY

A typical semiconductor microcavity is illustrated in Fig. 4. It is formed by two distributed Bragg reflectors (DBRs) and quantum wells in the cavity between the DBRs. The DBR is made of alternating layers of two materials with different indices of refraction. Light reflected from each interface constructively interferes, leading to very high reflectivity of the DBR. Propagation of light in this structure can be calculated with the transfer matrix method [44]. Near-perfect reflection over the desirable wavelength range can be achieved by carefully choosing the thickness and index of refraction of DBR materials. The quantum wells are placed at the antinodes of the cavity mode in order to maximize the coupling with light. In a microcavity of length L, the energy dispersion of the photon is given by

$$E_{cav}(k_\parallel, k_\perp) = \hbar(\frac{c}{n})\sqrt{k_\parallel^2 + k_\perp^2} \tag{2.8}$$

where n is the index of refraction of the cavity, $k_\parallel$ is the in-plane wave vector, $k_\perp = n2\pi/\lambda$, and $\lambda \sim 2L/m$ is wavelength of the m-th cavity mode. They are related by the emission angle θ

$$\frac{k_\parallel}{k_\perp} = \tan\left[\arcsin\left(\frac{\sin\theta}{n}\right)\right]. \tag{2.9}$$

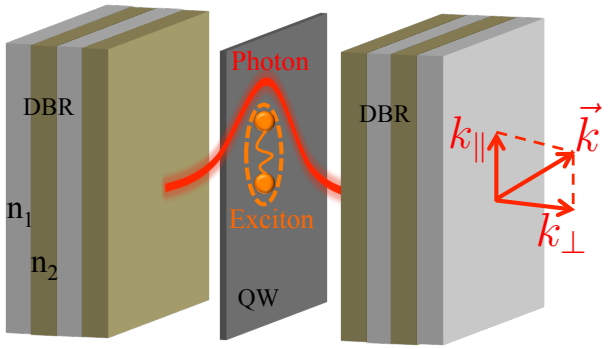

Figure 4: Schematic of the semiconductor microcavity and the photon and exciton inside the cavity. The cavity is formed by two distributed Bragg reflectors (DBRs) which are made of alternating layers of two different material with indices of refraction n_1 (gray) and n_2 (brown) respectively. Inside the cavity, a quantum well (gray slab) is placed at the antinode of the cavity mode (red curve). An exciton (orange) is a free particle in the 2D plane of the quantum well.

In the limit $k_{\|} \ll k_{\perp}$, the cavity photon energy can be written as

$$E_{cav}(k_{\|}, k_{\perp}) \approx \frac{\hbar k_{\perp} c}{n}\left(1 + \frac{k_{\|}^2}{2k_{\perp}^2}\right) = E_{cav}(k_{\|} = 0) + \frac{\hbar^2 k_{\|}^2}{2m_{cav}}, \tag{2.10}$$

where $m_{cav} = E_{cav}(k_{\|} = 0)/(c/n)^2$, is the effective mass of the photon, which is typically a few times 10^{-5} of the free electron mass (m_0) in GaAs-based microcavity. For example, in our sample (see Section 3.1) $m_{cav} = 3.1 \times 10^{-35}$ kg which is 3.45×10^{-5} times of the free electron mass ($m_0 = 9.1 \times 10^{-31}$ kg). Thus photons inside the cavity become free particles with a very small effective mass m_{cav} in the cavity plane. Due to the large energy spacing between the adjacent cavity modes (~ 1 eV), only one cavity mode that is resonant with the exciton transition in the QW is excited.

2.3 MICROCAVITY EXCITON-POLARITONS

2.3.1 Strong coupling of excitons and photons in a microcavity

In a microcavity, the coupling between excitons and photons is greatly enhanced by the fact that the oscillator strength of an exciton is increased due to the reduced Bohr radius in 2D, and the intensity of the light field is maximized at the antinodes. The maximum coupling can be achieved by placing the QWs at the antinodes of the cavity photon field (see Fig. 4 for example). When the spin degree of freedom of both excitons and photons is neglected, and only the coupling between the ground state heavy-hole exciton and the cavity photon is considered, the Hamiltonian of the system is [38]:

$$\begin{aligned}\hat{H} &= \sum_{\vec{k}_\parallel} E_{ex}(\vec{k}_\parallel)\hat{a}^\dagger_{\vec{k}_\parallel}\hat{a}_{\vec{k}_\parallel} + \sum_{\vec{k}_\parallel} E_{cav}(\vec{k}_\parallel,\vec{k}_\perp)\hat{b}^\dagger_{\vec{k}_\parallel,\vec{k}_\perp}\hat{b}_{\vec{k}_\parallel,\vec{k}_\perp} \\ &\quad + \sum_{\vec{k}_\parallel} g_0(\hat{b}^\dagger_{\vec{k}_\parallel,\vec{k}_\perp}\hat{a}_{\vec{k}_\parallel} + \hat{b}_{\vec{k}_\parallel,\vec{k}_\perp}\hat{a}^\dagger_{\vec{k}_\parallel}),\end{aligned} \tag{2.11}$$

where $(\hat{a}^\dagger_{\vec{k}_\parallel}, \hat{a}_{\vec{k}_\parallel})$ are the creation and destruction operators of an exciton with in-plane wave vector $\vec{k}_\parallel$, and $(\hat{b}^\dagger_{\vec{k}_\parallel,\vec{k}_\perp}, \hat{b}_{\vec{k}_\parallel,\vec{k}_\perp})$ are the creation and destruction operators of a cavity photon with wave vector $(\vec{k}_\parallel, \vec{k}_\perp)$, and g_0 is the exciton-photon coupling strength through the dipole interaction, which can also be interpreted as the rate of energy transferring between the exciton and the cavity photon. The diagonalization of the Hamiltonian can be realized by introducing the Hopfield transformation [18, 38]:

$$\hat{a}^U_{\vec{k}_\parallel} = C_{\vec{k}_\parallel}\hat{a}_{\vec{k}_\parallel} + X_{\vec{k}_\parallel}\hat{b}_{\vec{k}_\parallel,\vec{k}_\perp}, \tag{2.12}$$

$$\hat{a}^L_{\vec{k}_\parallel} = X_{\vec{k}_\parallel}\hat{a}_{\vec{k}_\parallel} - C_{\vec{k}_\parallel}\hat{b}_{\vec{k}_\parallel,\vec{k}_\perp}, \tag{2.13}$$

where $(X_{\vec{k}_\parallel}, C_{\vec{k}_\parallel})$ are the Hopfield coefficients, satisfying

$$|X_{\vec{k}_\parallel}|^2 + |C_{\vec{k}_\parallel}|^2 = 1. \tag{2.14}$$

They are determined by the energy detuning between the exciton and the photon (the $k_\perp$ dependence is dropped as only one transverse cavity mode is conerned)

$$\Delta(\vec{k}_\parallel) = E_{cav}(\vec{k}_\parallel) - E_{ex}(\vec{k}_\parallel), \tag{2.15}$$

and the coupling strength g_0:

$$|X_{\vec{k}_\parallel}|^2 = \frac{1}{2}\left(1 + \frac{\Delta(\vec{k}_\parallel)}{\sqrt{\left[\Delta(\vec{k}_\parallel)\right]^2 + 4{g_0}^2}}\right) \tag{2.16}$$

$$|C_{\vec{k}_\parallel}|^2 = \frac{1}{2}\left(1 - \frac{\Delta(\vec{k}_\parallel)}{\sqrt{\left[\Delta(\vec{k}_\parallel)\right]^2 + 4{g_0}^2}}\right). \tag{2.17}$$

The diagonalized Hamiltonian is:

$$\hat{H} = \sum_{\vec{k}_\parallel} E_{UP}\hat{a}^{U\dagger}_{\vec{k}_\parallel}\hat{a}^{U}_{\vec{k}_\parallel} + \sum_{\vec{k}_\parallel} E_{LP}\hat{a}^{L\dagger}_{\vec{k}_\parallel}\hat{a}^{L}_{\vec{k}_\parallel}, \tag{2.18}$$

with

$$E_{UP,LP}(\vec{k}_\parallel) = \frac{E_{ex}(\vec{k}_\parallel) + E_{cav}(\vec{k}_\parallel) \pm \sqrt{4{g_0}^2 + \left[\Delta(\vec{k}_\parallel)\right]^2}}{2}, \tag{2.19}$$

where the $+$ correponds to the upper polariton (UP) and the $-$ sign refers to lower polariton (LP). The new operators $(\hat{a}^{U\dagger}_{\vec{k}_\parallel}, \hat{a}^{U}_{\vec{k}_\parallel})$ and $(\hat{a}^{L\dagger}_{\vec{k}_\parallel}, \hat{a}^{L}_{\vec{k}_\parallel})$, therefore, can be interpreted as the creation and destruction operators of the UP and LP, respectively. The ground state of the system is the LP at $\vec{k}_\parallel = 0$, as both the UP and LP at higher energies can relax down to this state. Notice that when the spin degree of polaritons is added into Eq. (2.18), both the UP and LP will be twofold degenerate.

2.3.2 Important Properties of Exciton-Polariton

Fig. 5 shows the dispersions of the UP and the LP for different values of the photon-exciton detuning at $\vec{k}_{\parallel} = 0$ (Δ_0). In the vicinity of $\vec{k}_{\parallel} = 0$, the dispersion of the lower polariton $E_{LP}(\vec{k}_{\parallel})$ can be written as

$$E_{LP}(\vec{k}_{\parallel}) = E_{LP}(0) + \frac{\hbar^2 k_{\parallel}^2}{2m_{LP}}, \tag{2.20}$$

where m_{LP} is the effective mass of the LP near $\vec{k}_{\parallel} = 0$, given by

$$\frac{1}{m_{LP}} = \frac{|C_{\vec{k}_{\parallel}}|^2}{m_{cav}} + \frac{|X_{\vec{k}_{\parallel}}|^2}{m_{ex}}. \tag{2.21}$$

Since $m_{cav} \sim 10^{-4} m_{ex}$, for $\vec{k}_{\parallel} \sim 0$

$$m_{LP} \approx \frac{m_{cav}}{|C_0|^2}, \tag{2.22}$$

with

$$|C_0|^2 = \frac{1}{2}\left(1 + \frac{\Delta_0}{\sqrt{\Delta_0^2 + 4{g_0}^2}}\right). \tag{2.23}$$

In experiments, Δ_0 typically varies between $-2g_0$ and $2g_0$ leading to m_{LP} being in the range from 6.7 m_{cav} to 1.2 m_{cav}, about 10^4 times lighter than the free electron mass.

In addition to effective mass, other properties of the polaritons such as lifetime and particle-particle interaction strength can also be tuned by changing the detuning. The lifetime of a polariton is given by

$$\frac{1}{\tau} = \frac{|C_{\vec{k}_{\parallel}}|^2}{\tau_{cav}} + \frac{|X_{\vec{k}_{\parallel}}|^2}{\tau_{ex}}, \tag{2.24}$$

where τ_{cav} and τ_{ex} are the cavity photon lifetime and the exciton lifetime, respectively. The cavity photon lifetime τ_{cav} is the time it takes a photon to escape from the cavity, which is determined by the Q-factor of the cavity. The lifetime of exciton τ_{ex} is the time it takes for the electron and hole to recombine nonradiatively, such as by emitting phonons and falling into defect state. The radiative recombination process in which a photon is emitted does not change the total number of polaritons inside the cavity, therefore it does not contribute

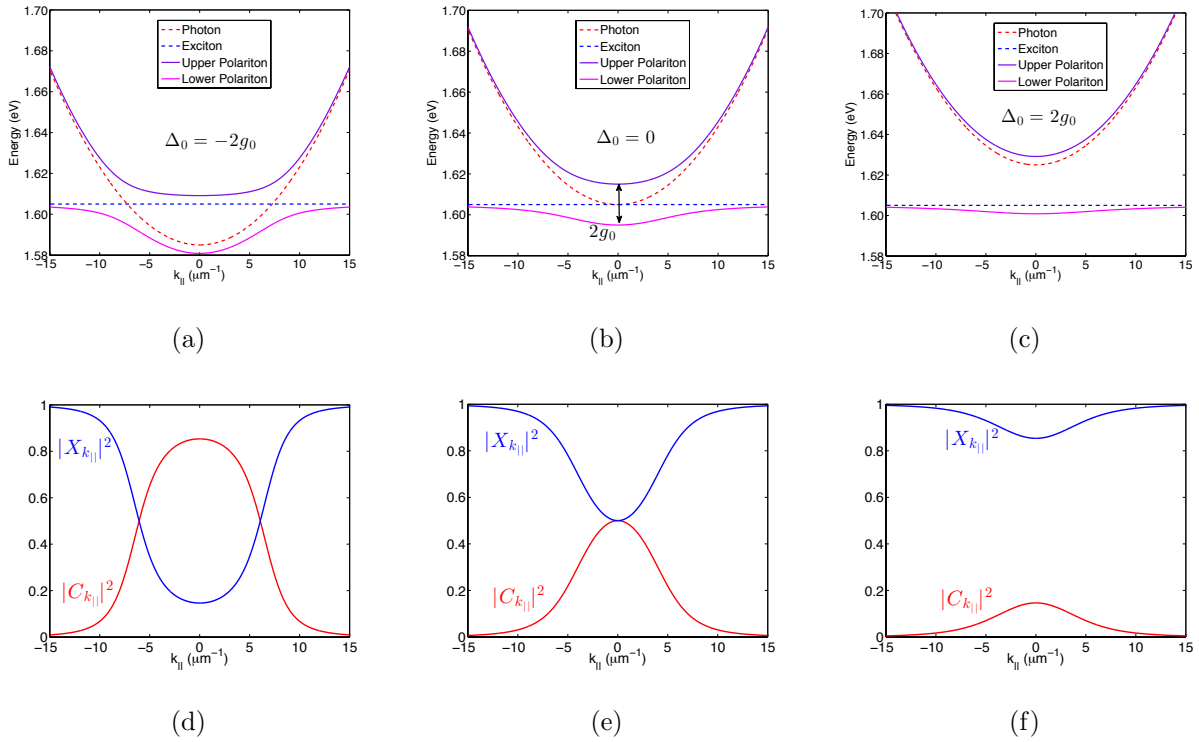

Figure 5: Disperion and Hopfield coefficients of upper- and lower polariton for different detunings at $k_{\|} = 0$. (a)-(c), disperions of the upper- (purple) and lower polaritons (pink) at different detunings: (a) $\Delta_0 = -2g_0$, (b)$\Delta_0 = 0$, (c)$\Delta_0 = 2g_0$. The dashed lines are the cavity photon dispersion (red) and exciton dispersion (blue). (d)-(f), Hopfield coefficients of the lower polaritons in (a)-(c), respectively. The red lines are the photon fraction of the lower polariton, and the blue lines are the exciton fraction.

to the polariton decay. As the time scale of non-radiative process is much larger than the cavity photon lifetime, namely $\tau_{ex} \gg \tau_{cav}$, the polariton lifetime becomes

$$\tau = \frac{\tau_{cav}}{|C_{\vec{k}_\parallel}|^2}. \tag{2.25}$$

Thus the polariton lifetime becomes longer when its photon fraction decreases. In early microcavity samples, the Q-factor was typically around 5000 [17], which gave a cavity photon lifetime $\tau_{cav} \sim 2$ ps, and the corresponding polariton lifetime at resonance was $\tau \sim 4$ ps.

A polariton interacts with other particles through its exciton component. At low temperature ($T \sim 10$ K), the scattering between polaritons and phonons is weak, and the polariton-exciton scattering and the polariton-polariton scattering are most relevant to the dynamics of the system [45]. The strengths of these interactions are given by

$$g_{pol-ex} = g_{ex}|X_{\vec{k}_\parallel}|^2, \quad g_{pol-pol} = g_{ex}|X_{\vec{k}_\parallel}|^4 \tag{2.26}$$

respectively, where g_{ex} is the exciton-exciton interaction strength. Polaritons can also strongly interact with electrons. When the exciton fraction is small (negative detuning) the polariton-polariton interaction is weak, and thermal equilibrium can not be established among polaritons. However, when the exciton fraction is large the interaction between polaritons becomes stronger. In addition, the polariton lifetime increases. It has been shown that under such conditions polaritons can reach thermal equilibrium with each other [25].

2.4 BOSE-EINSTEIN CONDENSATION AND SUPERFLUID

2.4.1 Bose-Einstein Condensation

In 1924 and 1925, Einstein developed the now-called Bose-Einstein statistics [1, 50] by extending Bose's statistics of indistinguishable photons [51] to material particles. Particles that obey the Bose-Einstein statistics are called bosons. It turns out that all the particles with integer spin, such as photons, excitons and hydrogen atoms, are bosons. Einstein predicted that for a macroscopic system of noninteracting bosons with conserved total number

of particle, a finite fraction of the particles will condense into a single particle state below a critical temperature. This phenomenon is referred to as Bose-Einstein condensation (BEC).

For a three-dimensional (3D) system of noninteracting bosons in the grand canonical ensemble, the total number of particles in the system is [52]

$$N = \sum_k n_B(\epsilon_k) = \int \rho(\epsilon) n_B(\epsilon) d\epsilon \tag{2.27}$$

where $n_B(\epsilon_k) = 1/\left\{\exp[\beta(\epsilon_k - \mu)] - 1\right\}$ is the Bose-Einstein distribution, $\beta = 1/k_B T$, μ is the chemical potential, and $\rho(\epsilon)$ is the density of states. The requirement that $n_B(\epsilon_k) \geq 0$ gives a constraint $\mu < \epsilon_0$, where ϵ_0 is the energy of the single-particle ground state. When $\mu \to \epsilon_0$, the occupation number of the ground state

$$N_0 = \frac{1}{\exp[\beta(\epsilon_0 - \mu)] - 1}. \tag{2.28}$$

becomes increasingly large. This is the mechanism of Bose-Einstein condensation. The total number of particles can be written as

$$N = N_0 + N_T, \tag{2.29}$$

where

$$N_T = \sum_{\epsilon_k > \epsilon_0} n_B(\epsilon_k) = \int_{\epsilon > \epsilon_0} \rho(\epsilon) n_B(\epsilon) d\epsilon \tag{2.30}$$

is the number of particles in the excited states which increases as temperature increases. At fixed temperature T, N_T is a smooth function of μ and reaches its maximum value, N_c, at $\mu = \epsilon_0$ [52]. On the other hand, N_0 is less than 1, except when $\mu \sim \epsilon_0$ where it diverges. If $N_c(T, \mu = \epsilon_0) > N$, then Eq. (2.29) can always be satisfied with $N_0 \to 0$. On the other hand, if $N_c(T, \mu = \epsilon) < N$, a finite fraction of all the particles has to go into the ground state in order to satisfy Eq. (2.29). Therefore, the critical temperature, T_c, at which particles start to condense to the ground state is defined by the relation

$$N_T(T_c, \mu = \epsilon_0) = N. \tag{2.31}$$

As temperature decreases, the number of particles going into the ground state will increase.

Let us first consider the system of N noninteracting bosons in a 3D box ($V = L^3$) as a concrete example [52]. The single-particle Hamiltonian is

$$H_1 = \frac{p^2}{2m} \tag{2.32}$$

Under the periodic boundary condition $\psi(x, y, z) = \psi(x + L, y, z)$, etc., the eigenfunction of H_1 is

$$\psi_{\vec{k}} = \frac{1}{\sqrt{V}} e^{i\vec{k}\cdot\vec{r}} \tag{2.33}$$

with energy $\epsilon_k = \hbar^2 k^2/2m$ and momentum $\hbar\vec{k} = \vec{n}2\pi\hbar/L$, where $\vec{n} = (n_x, n_y, n_z)$, $n_{x,y,z} = 0, \pm 1, \pm 2, ...$ The ground state of the system is the state with $n_x = n_y = n_z = 0$ and $\epsilon_0 = 0$. The density of states of this system is

$$\rho_{3D}(\epsilon_k) = \frac{dN_k}{dk}\frac{dk}{d\epsilon_k} = \frac{Vm^{3/2}}{\sqrt{2}\hbar^3\pi^2}\epsilon_k^{1/2}. \tag{2.34}$$

At critical temperature $T = T_c$, $\mu \to \epsilon_0$ and in Eq. (2.31) becomes

$$n \equiv \frac{N}{V} = 2.612 \left(\frac{mk_B T_c}{2\pi\hbar^2}\right)^{3/2}, \tag{2.35}$$

where n is the density of particles, from which the critical temperature is obtained as

$$T_c = 3.3\frac{\hbar^2}{mk_B} n^{2/3}. \tag{2.36}$$

Eq. (2.36) shows that the critical temperature is completely determined by the density and mass of the particle. Notice that the thermal de Broglie wavelength of the particle is

$$\lambda_T = \sqrt{\frac{2\pi\hbar^2}{mk_B T}}. \tag{2.37}$$

and Eq. (2.35) can be rewritten as

$$n = \frac{2.612}{\lambda_{T_c}^3} \tag{2.38}$$

Therefore, the critical temperature T_c is the temperature at which the thermal de Broglie wavelength λ_T becomes comparable to the particle spacing $r_{3D} \sim n^{-1/3}$. This interpretation provides a more intuitive picture of BEC: as the temperature decreases, the de Broglie wavelength of particle becomes increasingly large, when it becomes comparable to the particle

spacing the wavefunctions of particles start to overlap and eventually they merge into a single wavefunction with a macroscopic number of particles in it.

Now, let us consider the same system but in 2D ($A = L^2$). The single-particle Hamiltonian and its eigenstates have the same form as that of the 3D system, except the density of states now becomes

$$\rho_{2D}(\epsilon_k) = \frac{dN_k}{dk}\frac{dk}{d\epsilon_k} = \frac{Am}{2\pi\hbar^2}, \tag{2.39}$$

which is a constant. At temperature T, the total number of particles in the excited states becomes,

$$N_T = \sum_{\epsilon_k > \epsilon_0} n_B(\epsilon_k) = \frac{Am}{2\pi\hbar^2}\int_{\epsilon>\epsilon_0} \frac{d\epsilon}{\exp[\beta(\epsilon-\mu)]-1} \tag{2.40}$$

which diverges except for $T = 0$. Therefore, for $T > 0$ the occupation number of the ground state remains negligible as compared to N, thus BEC can never happen [53].

The situation changes dramatically, however, when a trapping potential is applied to the 2D noninteracting Bose gas [54, 55, 56, 57, 58]. For example, in a 2D harmonic trap, the density of states of the noninteracting Bose gas becomes $\rho_{2D} \sim \epsilon$, and the critical temperature is $T_c \sim \omega_0 N^{1/2}$ where ω_0 is the trapping frequency. The trapping potential modifies the density of states therefore removes the divergence in the integral in Eq. (2.40).

For a polariton system, which is a 2D system, there are often intrinsic trapping potentials due to disorders/defects in the crystal. In CdTe- and GaN-based microcavities, this trapping effect is so strong that polaritons are essentially localized and BECs are formed in it [15, 16]. In microcavities with less disorder, such as GaAs-based microcavity, polaritons move freely in the cavity plane, therefore external trapping potential is needed to trap them. Over the last few years, various trapping methods have been developed [59, 60]. In our experiment, we create trapping potential for polaritons with mechanical stress and laser generated barriers, which will be discussed in Section 3.4.

To get an idea about the temperature scales of the BEC experiments, let us estimate the critical temperatures for bosonic atoms and polaritons in 2D traps. We can estimate the critical temperature without worrying about the details of the trapping potential, because there is the universal argument: at the critical temperature the thermal de Broglie

wavelength becomes comparable to the particle spacing. For a 2D system, therefore,

$$n \sim \frac{1}{\lambda_{T_c}^2} = \frac{m k_B T_c}{2\pi\hbar^2}. \tag{2.41}$$

In the experiments with alkali atoms such as ^{87}Rb, the achievable particle densities are in the range from 10^8 cm^{-2} to 10^{10} cm^{-2}. This gives a critical temperature between 10^{-8} K and 10^{-6} K. To reach such low temperature, requires sophisticated techniques such as laser cooling and evaporative cooling [61]. This is why atomic BEC only become possible in experiments until 1995. For microcavity polaritons, the typical density that can be achieved is of the order of 10^8 cm^{-2} and the mass is 10^{-4} times of the free electron mass, or equivalently 10^{-9} times of the alkali atom mass. Therefore the critical temperature of polariton BEC is $T_c \sim 10$ K, which is very easy to get with traditional cryogenic methods. This value of critical temperature is in good agreement with the experimental results of polariton BECs [15, 17]. In fact, with higher pump intensity and larger exciton binding energy in materials such as GaN, features of polariton BEC has been observed at room temperature [16]

2.4.2 Superfluid and Vortices

As mentioned in the Introduction, there are fundamental connections between the Bose-Einstein condensate and the superfluid [6]. A system with a Bose-Einstein condensate is often called superfluid because of its special properties. In this section, I will follow the discussion on this topic in Chapter 11 of Ref. [39]. The wavefunction of a Bose-Einstein condensate can by written as,

$$\psi(\vec{r}, t) = \sqrt{n_0(\vec{r}, t)} e^{i\theta(\vec{r}, t)}, \tag{2.42}$$

where $n_0(\vec{r}, t)$ is the density of particles in the condensate, $\theta(\vec{r}, t)$ is the phase of the condensate. To write down Eq. (2.42), we have assumed that both n and θ do not change dramatically over short distances. The assumption about θ requires that there is long-range phase coherence in the condensate. This wavefunction plays the role of the order parameter of the BEC phase: below the BEC threshold, $n_0(\vec{r}, t) = 0$, thus $\psi(\vec{r}, t) = 0$; above the BEC threshold, $\psi(\vec{r}, t) \neq 0$ and long-range coherence spontaneously appears in the system.

The number current density in the condensate is given by

$$\vec{j} = \frac{i\hbar}{2m}(\psi\nabla\psi^* - \psi^*\nabla\psi). \tag{2.43}$$

Substituting in the condensate wavefunction (2.42), after carrying out the calculation, this becomes

$$\vec{j} = \frac{\hbar}{m} n_0(\vec{r},t)\nabla\theta(\vec{r},t), \tag{2.44}$$

which means the current is proportional to the gradient of the phase. Therefore, when the condensate phase is not a constant, there is current flow in the condensate. A direct consequence of this result is that a condensate with uniform density is irrotational. This is because

$$\begin{aligned} \nabla \times \vec{j} &= \frac{\hbar}{m}\left[n_0\nabla\times(\nabla\theta) - \nabla\theta\times(\nabla n_0)\right] \\ &= \frac{\hbar}{m} n_0 \nabla\times(\nabla\theta) \\ &= 0 \end{aligned} \tag{2.45}$$

since the curl of a gradient is 0. But if there are density singularities (at which $n_0 = 0$) in the condensate, then $\nabla n_0 \neq 0$ at the these positions, and $\nabla \times \vec{j} \neq 0$. When going around a closed loop L that encloses the singularities, we have

$$\begin{aligned} \oint_L \vec{j}\cdot d\vec{l} &= \frac{\hbar}{m}\oint_L \nabla\theta \cdot d\vec{l} \\ &= \frac{\hbar}{m} n_0(\theta_f - \theta_i), \end{aligned} \tag{2.46}$$

where θ_i and θ_f are the beginning and ending values of θ in going around the loop. The wave function must be single-valued, thus,

$$e^{i\theta_i} = e^{i\theta_f} \tag{2.47}$$

which indicates

$$\theta_f - \theta_i = 2\pi N \tag{2.48}$$

where N is an integer. The flow around any closed loop is therefore quantized,

$$\oint_L \vec{j}\cdot d\vec{l} = N\frac{h}{m} n_0. \tag{2.49}$$

N is identified as the number of vortices—that is density singularities in the superfluid.

2.4.3 BEC of Polaritons and the Generalized Gross-Pitaevskii Equation

All the discussion on BEC and superfluidity in previous sections are for a noninteracting Bose gas in thermal equilibrium. However, the ideal Bose gas is a pathological case (for example, see discussion in Chapter 11 in Ref. [39]). A more realistic system is the weakly interacting Bose gas, such as weakly interacting atomic gas and polaritons. Reviews of the theory and experiments of a weakly interacting atomic gas can be found in Refs. [62, 63, 64]. For polariton systems, nice reviews on recent theoretical and experimental developments can be found in Refs. [65, 66]. The theory that directly relates to the experiments of this thesis, polaritons in 2D traps, has has been worked out by Berman et. al. [67].

The feature that makes the polariton system fundamentally different from cold atoms is that it is intrinsically dissipative: polaritons are constantly decaying by emitting photons into the outside environment on the time scale of $4 \sim 200$ ps. When the microcavity is excited with a continuous-wave (CW) laser, however, the system can reach a steady state in which polaritons that decay out of the cavity are replaced by polaritons created by the pump laser. Therefore, when the decay and creation of polaritons are balanced, the system will have an approximately fixed number of particles in it. On the other hand, the short lifetime of polaritons seems to indicate that the system is also very far from thermal equilibrium. This is not the case, however, because the parameter that determines whether a system can reach thermal equilibrium is the ratio of the particle lifetime to the particle-particle scattering time, rather than the absolute value of the particle lifetime. It has been shown numerically and experimentally that a system of interacting Bosons can reach thermal equilibrium after $4 \sim 5$ scatterings [7, 68]. Therefore, the polaritons, with a scattering time of approximiate 0.5 ps and lifetime of $4 \sim 200$ ps, can reach thermal equilibrium with each other. This explains why BEC, originally defined for thermal equilibrium systems, has been observed in polariton systems. Now with the polariton lifetime reaching 270 ps, this system is even more close to a true equilibrium system.

As discussed above, in order to correctly describe the physics of polariton BEC, one needs to take into account both decay and external pumping of polaritons. The generalized Gross-Pitaevskii equation (gGPE) is by far the most successful model in describing both the

dynamics and stead-state properties of BEC in a polariton system. This equation is written as [47]

$$i\frac{\partial\psi}{\partial t} = \left\{-\frac{\hbar\nabla^2}{2m_{LP}} + \frac{i}{2}[R(n_R) - \gamma] + g_{pol-pol}|\psi|^2 + 2g_R n_R\right\}\psi, \tag{2.50}$$

where ψ is wavefunction of the polariton condensate, $R(n_R)$ is the gain rate of the condensate due to the Bose stimulated scattering of polaritons from the reservoir and pumping. γ is the decay rate of the polaritons through photon leaking. $g_{pol-pol}|\psi|^2$ describes the polariton-polariton interaction, $g_R n_R$ is the interaction between the condensate and the reservoir. This equation has been successfully used to explain various polaritons experiments, such as the excitation spectrum [30], and polariton superfluidity [27, 28].

3.0 MICROCAVITY SAMPLE AND EXPERIMENTAL METHODS

In this chapter I will describe the microcavity structure used in our experiments. In this microcavity, polaritons with a lifetime of 270 ps have been observed [48, 49], which is more than 10 times longer longer than the lifetime in other existing microcavity structures [15, 17, 20]. This sample also achieved a very high structural quality with very few defects in it. The extraordinary long lifetime and the absence of defects enable the polaritons to propagate over hundreds of microns, allowing the possibility of a whole new category of experiments. We will also introduce the optical methods that we used to generate, detect and manipulate polaritons. They include real-space and momentum-space imaging methods, temporal and spatial coherence measurement, and methods of trapping polaritons.

3.1 LONG-LIFETIME POLARITON SAMPLE

3.1.1 Properties of the Sample

The microcavity used in our experiments is a GaAs-based microcavity grown by Loren Pfeiffer's group at Princeton with molecular beam epitaxy (MBE) method. The whole structure is grown on a 2-inch diameter GaAs substrate along the [001] direction. As shown in Fig. 6(a), the microcavity consists of two distributed Bragg reflectors (DBRs) and a $3\lambda/2$ cavity between them. The DBRs are made of alternating layers of AlAs and $Al_{0.2}Ga_{0.8}As$, which are also used as spacers inside the cavity. These two materials are chosen for two reasons. First, they have the same crystal symmetry and approximately the same lattice constant. Therefore, the strain due to lattice mismatch between these two materials is minimized which

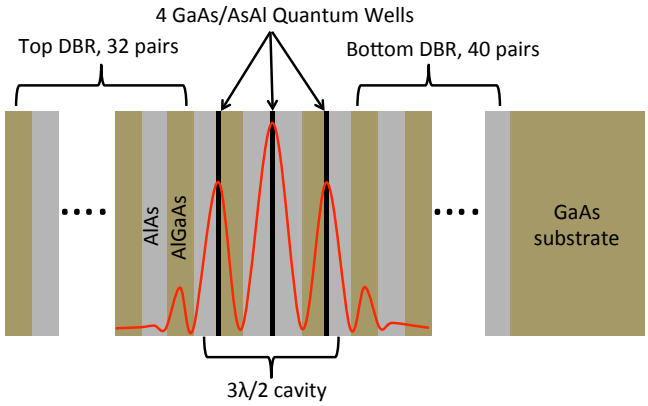

(a)

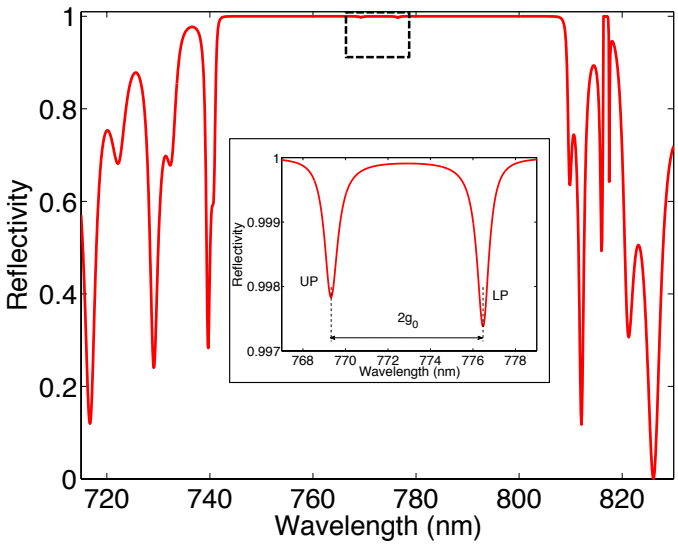

(b)

Figure 6: Schematic microcavity structure used in our experiments and the calculated reflectivity spectrum. (a) There are 32 pairs of AlAs/AlGaAs layers in the top DBR and 40 pairs of them in the bottom DBR. The distance between the DBRs is chosen to make a $3\lambda/2$ cavity, with $\lambda = 772.48$ nm. The red curve represents the intensity distribution of the cavity mode inside the cavity. Three sets of 4 GaAs/AlAs quantum wells are placed at the antinodes of the cavity mode. The whole structure is grown on a GaAs substrate. (b) The reflectivity spectrum (red) of the microcavity calculated with transfer matrix method. The inset shows a section of reflectivity spectrum enclosed by the dashed rectangle. The two reflectivity minima in the stop band of the microcavity, at 769.2 nm and 776.5 nm, correspond to the upper polartion (UP) and lower polariton (LP).

ensures very high quality of the microcavity structure. Second, the band gap of $Al_{0.2}Ga_{0.8}As$ is about 690 nm at 10 K, and AlAs has even larger band gap; thus they are both transparent to longer wavelengths.

Inside the cavity, three sets of 4 GaAs/AlAs quantum wells are placed at the antinodes of the cavity mode, maximizing the coupling with the cavity photons. The quantum well is formed by a 7-nm-thick GaAs layer sandwiched between two 3-nm-thick AlAs layers. The wavelength of the cavity mode is chosen to be $\lambda = 772.48$ nm (1.6050 eV), in resonance with the quantum well exciton. Fig. 6(b) shows the reflectivity spectrum of the microcavity (red), in the wavelength range from 715 nm to 830nm, calculated by the transfer matrix method. As one can see, the reflectivity is 1 over about 70 nm range. The inset shows a section of the reflectivity spectrum enclosed by the dashed rectangle. The two dips seen in the stop band, at 769.2 nm and 776.5 nm, correspond to the upper and lower polaritons; they are separated by 14.9 meV in energy (see the inset), which is Rabi splitting. Because the line width of theses two dips are much narrower than the step size of our numerical calculation, they appear as two very shallow dips in the reflectivity spectrum.

In order to increase the lifetime of the polaitons, we doubled the number of layers in the DBRs compared to the structure in our previous experiments [17]. The current microcavity has 32 pairs of $AlAs/Al_{0.2}Ga_{0.8}As$ $\lambda/4$ layers in the top DBR, and 40 pairs of those layers in the bottom DBR. The cavity photon lifetime in this sample is measured to be 135 ps [48, 49], which gives a polariton lifetime of 270 ps at resonance. By comparison, in the old sample the cavity photon lifetime was 2 ps and the polariton lifetime at resonance was 4 ps.

During the growth process, the thickness of the microcavity is tapered along the radial direction of the wafer (inset (a) of Fig. 7), leading to a continuous increase of the cavity photon energy towards the edge of the wafer. The exciton energy also changes, but its gradient is much smaller than that of the photon energy. We designed the sample in such a way that the detuning is negative at the center of the wafer, and it becomes positive approaching the edge of the wafer. The resonance region, where the detuning is 0, is about 19 mm away from the center of the wafer. A larger area of resonance region can be obtained by making the resonance position further away from the center. But there is a tradeoff between the size of the resonance region and the density of defects in that region. Strain accumulates

at the edge of the sample, as it is the place where the crystal structure terminates. Therefore, the density of defects increases as one gets closer to the edge. Our design gives us a large enough area to work with in which the effects of defect are negligible.

The position at which the excitons are in resonance with cavity photons is determined by measuring the intensity of the PL of the polaritons as a function of distance to the center of the wafer, when the sample is excited by a laser with a photon energy higher than the stop band energy of the DBRs. The excitation laser creates excitons inside the microcavity, which couple to the cavity photon mode, forming polaritons. The coupling is the strongest when the exciton energy is in resonance with the cavity photon energy, and the intensity of the PL also reaches its maximum value for a fixed pump power. The resonance position found with this method is 19.3 mm away from the center of the sample wafer. The LP energy at this position is 1.5995 eV, indicating a Rabi splitting ($2g_0$) of 11 meV between the UP and LP. The effective mass of the cavity photon is 3.42×10^{-5} m_0, which gives a polariton effective mass of 6.84×10^{-5} m_0 at resonance, where $m_0 = 9.1 \times 10^{-31}$ kg is the free electron mass.

Fig. 7 shows the energy of the lower polariton with $k_{\parallel} = 0$ in the region near the resonance position of sample. On the negative detuning side of the resonance, the LP energy gradient is 9.7 meV/mm, from which a cavity photon energy gradient of 12.69 meV/mm is extracted. The cavity photon energy gradient across the sample provides a large range of detuning to work with. As discussed in Section 2.3, the properties of polaritons can be tuned by changing the detuning. Therefore, by moving to different spots on the sample we can study polaritons with very different properties. For example, Fig. 8 shows the energy dispersion data of polaritons at three different locations on the sample: where the detunings are -24.8 meV, 0 meV and +8.5 meV. The corresponding effective mass of the polaritons, obtained by fitting the data with Eq. (2.20), are 3.52×10^{-5} m_0, 6.84×10^{-5} m_0 and 1.77×10^{-4} m_0 respectively.

3.1.2 Dislocations in the Long-Lifetime Polariton Sample

It is remarkable that very high quality is achieved in this long-lifetime microcavity sample which requires over 30 hours of continuous MBE growth. The very low density of disor-

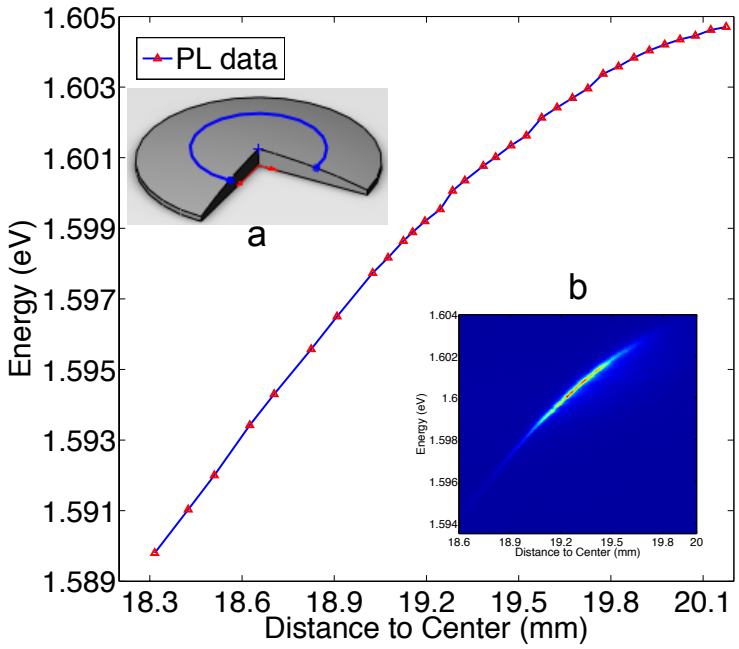

Figure 7: LP energy as a function of distance to the center of the wafer. The PL at different locations is taking by scanning the sample along the cavity gradient with a focused laser beam (20 μm in diameter) from the diode laser, which is working at 705 nm and the pump power is 4 mW. The sample temperature is between 6 K to 7 K. The inset (a) illustrates the shape of the sample, and the blue arc on the surface indicates the position where exciton energy and cavity photon energy are in resonance. The inset (b) shows the PL near the resonance position when the sample is illuminated by a defocused laser beam.

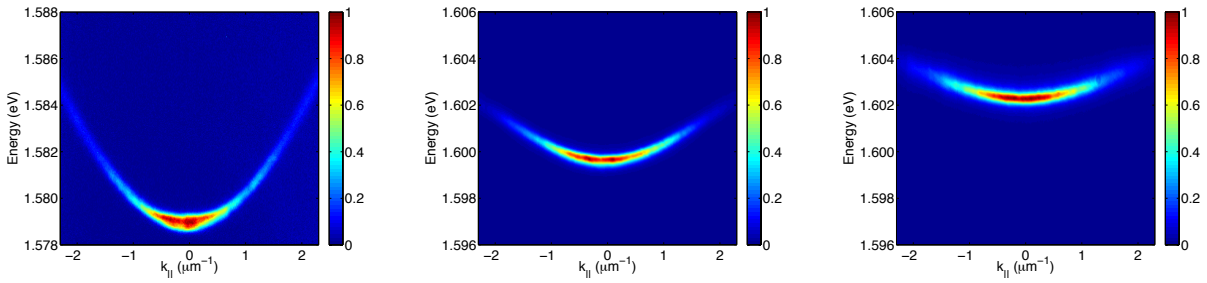

Figure 8: Energy dispersion of polaritons at different locations on the sample where the detuning is (a) $\Delta_0 = -24.8$ meV, (b) $\Delta_0 = 0$ meV, and (c) $\Delta_0 = +8.5$ meV. The corresponding effective of the polariton are (a) $m_{LP} = 3.52 \times 10^{-5}\ m_0$, (b) $m_{LP} = 6.84 \times 10^{-5}\ m_0$, and (c) $m_{LP} = 1.77 \times 10^{-4}\ m_0$.

ders/defects in this sample allows the polaritons to propagate over macroscopic distances, which will be discussed in Chapter 4. While the sample is nearly free of disorder/defects of submicron size, there are dislocations in the sample caused by the misfits at the interfaces between the epitaxial layers of different materials. Fig. 9(a) is a schematic of a misfit dislocation formed at the interface of two epitaxial layers with different lattice constants. Fig. 9(b) is a real-space image of a region on the sample where there are several dislocations. For example, there are two dislocations going along the [110] direction in the central part of this region. Even though the lattice mismatches between the materials in our sample are very small, 0.1% for GaAs and AlAs and 0.08% for AlAs and $Al_{0.2}Ga_{0.8}As$, the number and the thickness of the layers are large, leading to the production of misfit dislocatons [69, 70, 71]. As the total thickness of the microcavity increases, more and more misfit disolcations are formed. Fig. 9(c) shows the real-space image of an region on another long-lifetime sample. This sample is about 5% thicker than the one shown in Fig. 9(b). As one can see, in Fig. 9(c) the density of dislocations is higher than that in Fig. 9(b). By contrast, in our old samples where the thickness of the microcavity structure was only 1/2 of the current sample, the misfit dislocations were very rare. It has also been observed that many of these dislocations

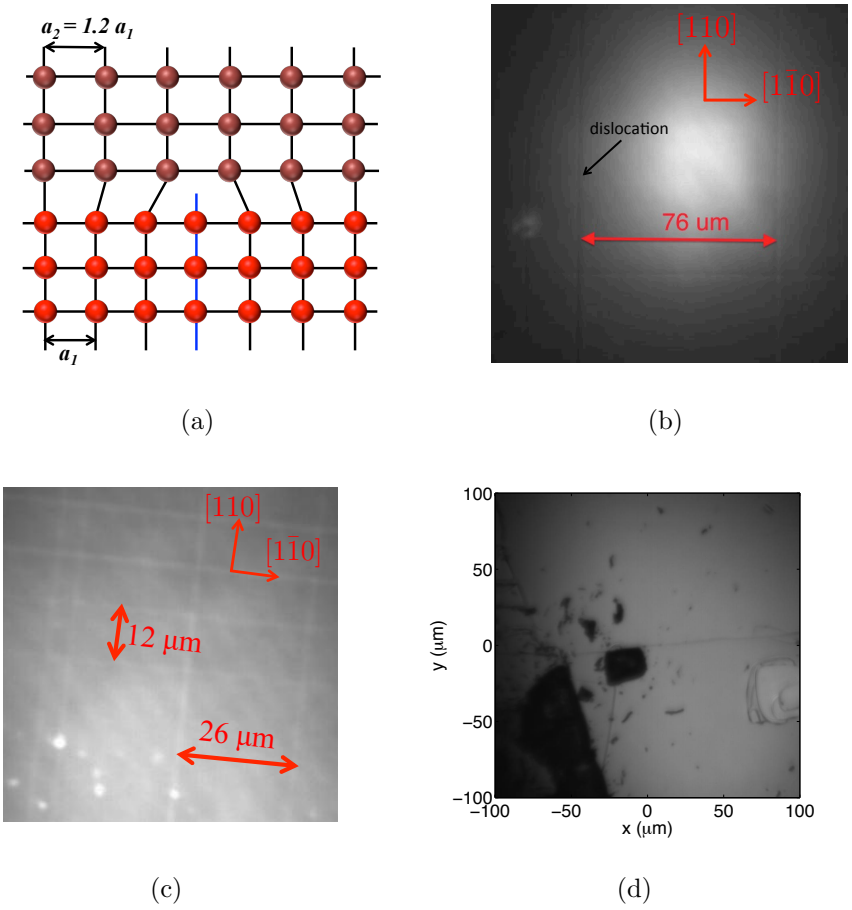

Figure 9: (a) Schematic of a misfit (blue line) at the interface between two epitaxial layers with different lattice constants (a_1 and a_2). (b) Real-space image of a region on the sample when it is illuminated with a defocused laser beam. There are two dislocations going along the [110] direction in the central part of this image. (c) Real-space image of a region on another long-lifetime microcavity sample which is 5% thicker than the one shown in (b). (d) Real-space image of the surface of the sample near one edge of the sample. The black pockets correspond to the regions in which the surface of the sample is destroyed by oxidization.

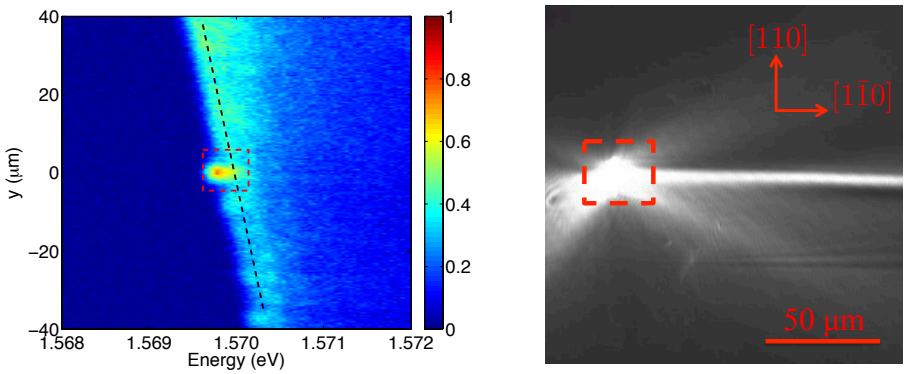

(a) (b)

Figure 10: (a) Energy-resolved real-space image of polaritons in a region where there is a dislocation going through $y = 0$ μm. The red box encloses polaritons trapped in the dislocation. The energy of these polaritons is about 0.15 meV lower than those outside the dislocation. (b) Propagation of polaritons in the channel formed by a dislocation. The polaritons are created non-resonantly by focusing a laser beam at one end of the dislocation (red dashed box), which goes from left to right.

start from the edges of the sample where the sample was cleaved (Fig. 9(d)). Strain built up at the edges when the sample was cleaved and generated dislocations that run into the sample. They edges were also oxidized over time as they were exposed to the atmosphere, and started breaking apart after many thermal cycles. These processes all lead to the generation of dislocations in the sample. Fig. 9(d) shows a real-space image of the sample surface near one edge of the sample. The dark pockets in on the sample surface are the regions in which the sample surface is destroyed by oxidization and accumulated strain when the sample was cleaved.

The dislocations spoil the DBRs and reduce the confinement of the cavity photon in the regions where they are. As a consequence, the energy of the cavity photons as well as the energy of the polaritons are lower in these regions. Polaritons can be trapped in these local energy minima. Fig. 10(a) shows the energy-resolved real-space image of polaritons created by a defocused laser beam in a region where there is a dislocation at y = 0 μm. As one can see, the energy of the polaritons in the dislocation (red dashed box) is about 0.15 meV lower than that of the polaritons outside the dislocation.

Polaritons can also propagate along the dislocation when they have non-zero in-plane momentum along the dislocation. Fig. 10(b) shows the propagation of polaritons in a dislocation when the polaritons are created by a focused laser beam near the end of the dislocation. In this case, the dislocation plays the same role as microcavity wires which are produced by etching the microcavity sample into strips of a few microns wide [24]. Thus, it might be possible to use the dislocations as 1D channels for the study of the polaritons in 1D. For example, one of our on-going effort is to study the interaction of two independent polariton droplets by colliding them at the intersection of two microcavity wires. In principle, we can do the same experiment with two crossed dislocations.

3.2 CREATING POLARITONS WITH OPTICAL EXCITATION

In our experiments, the polaritons are generated through optical excitation with laser. In order to get light to transmit into the cavity, the pump laser photon energy needs to be

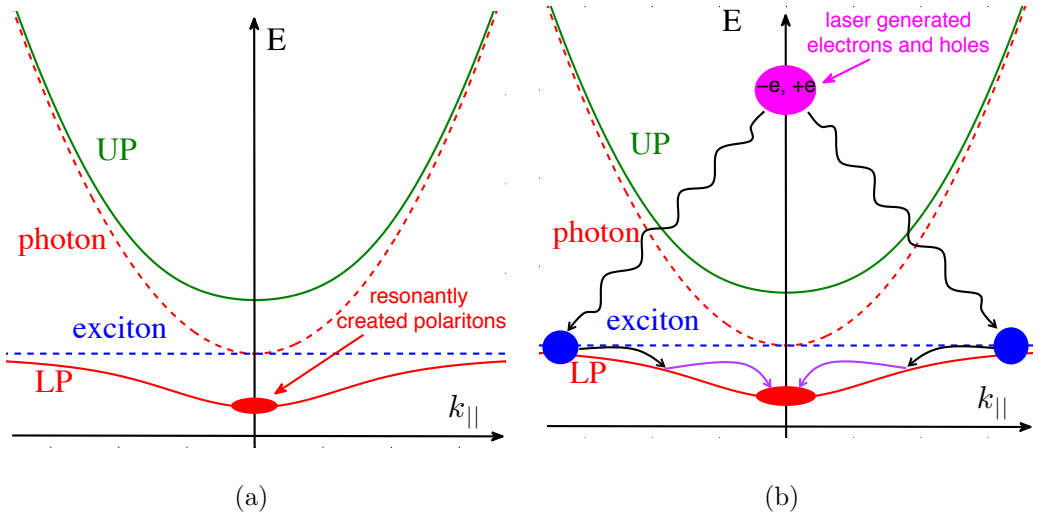

Figure 11: Optical methods for creating polaritons. (a) Illustration of resonant pumping method. The polaritons (red oval) are directly created by the excitation laser which is in resonance of the polariton mode. (b) Illustration of non-resonant pumping method. The excitation laser is at a energy much higher than the polaritons. It creates high energy electrons and holes in the quantum well. The electrons and holes cool down through scattering with each and with lattice by emitting phonons (black wavy line). At low enough energy, they form excitons which can couple to cavity photons to form polaritons with high in-plane momentum (blue spots). These polaritons relax to lower energy states by emitting phonons (dark arrow) and scattering with each (purple arrow).

either in resonance with the polariton mode or at photon energy above the stop band edge (see Fig. 6(b)). When the pump laser is in resonance with the polariton mode, it directly creates polaritons in the cavity and this process is known as resonant pumping (Fig. 11(a)). In this case, the polaritons inherit all the properties from the laser photons, such as in-plane momentum, energy, polarization and phase coherence. Thus the properties of the polaritons are precisely controlled by the pumping laser, which is crucial for applications such as information process with polaritons. But the coherence of polaritons created by resonant pumping method can not be regarded as spontaneous coherence coming from quantum phase transition.

When the pump laser excites the microcavity with photon energy above the stop band edge (see Fig. 6(b)), it creates hot carriers, i.e. electrons and holes with high kinetic energies, in the quantum wells. The hot carriers cool down to form excitons by emitting phonons. After relaxing to low enough energy, excitons couple to cavity photons to form polaritons. Fig. 11(b) illustrates the non-resonant pumping method. The information originally carried by the laser photons, such as phase coherence and polarization, is lost in these processes. For this reason, it is advantageous to study spontaneous coherence of polaritons under a non-resonant pumping scheme. Another interesting effect of the non-resonant pumping method is that it creates an exciton reservoir at the pump spot, which can be used as a potential barrier for polaritons, as I will discuss later in this chapter. All the experiments presented in this thesis are done with the non-resonant pumping method. For the experiments that will be discussed in Chapter 4, an intensity-stabilized diode laser was used to excite the sample, which has a maximum output power of 50 mW and is wavelength tunable from 705 nm to 715 nm. For the experiments in other parts of the thesis, the excitation laser is a home-made continuous wave Ti:Sapphire laser. The wavelength of this laser can be tuned from 720 nm to 900 nm, and the maximum output power is about 500 mW when it is pumped by a 5 W green laser.

3.3 OPTICAL DETECTION OF POLARITONS

Polaritons decay by emitting photons out of the cavity; there is one-to-one correspondence between the polariton and the emitted photon. Thus, by collecting and analyzing photons coming out of the cavity, all the information about the polaritons can be obtained. A real-space image of the photons will tell us the properties of the polaritons as a function of position, such as particle density, energy and phase. The in-plane momentum of a polariton is mapped to the emission angle of the photon, so the distribution of the in-plane momentum of polaritons can be obtained by angle-resolved image of the PL. In this section, I will describe the optical setups for real-space imaging, momentum-space imaging, and phase coherence measurement.

3.3.1 Real space spectroscopy

Real space measurement is carried out with the setup in Fig. 12(a). The real space image of the polaritons is formed on the entrance slit of the imaging spectrometer by a combination of two lens. When the spectrometer is working in the imaging mode, it plays the role of a plane mirror, projecting the image on the entrance slit to the charge coupled device (CCD) camera mounted on the exit port of the spectrometer. The spectrometer is an SP2300 spectrometer from Princeton Instruments. It has a focal length of 300 mm, and a 1800 groves/mm grating is installed in the spectrometer. The CCD camera is a Cascade:1K camera from Photometrics. This camera uses a EMCCD which has an active area of 1004×1002 pixels with a pixel size of 8 μm $\times$ 8 μm. The EMCCD is cooled down to -30 C in operation by a peltier cooler to suppress thermal noise. This spectrometer and the CCD together give a spectral resolution of 0.056 nm, corresponding to an energy resolution of 0.1 meV at 776 nm.

Fig. 12(b) shows an image of the surface of the sample when a broad band light ("white" light) is used to illuminate the sample. Fig. 13(a) shows the spatially resolved luminescence of polaritons when the sample is excited with a defocused, non-resonant laser beam. The spectrum of the PL from the central slice ($x = 0$ μm) of Fig. 13(a) is shown in Fig. 13(b).

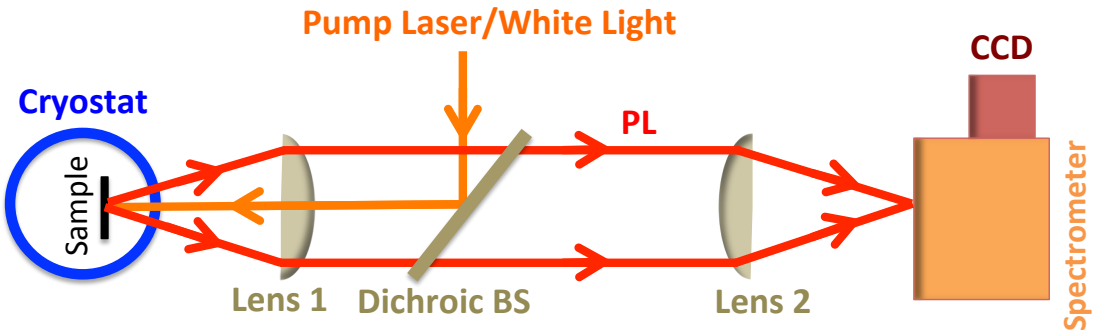

(a)

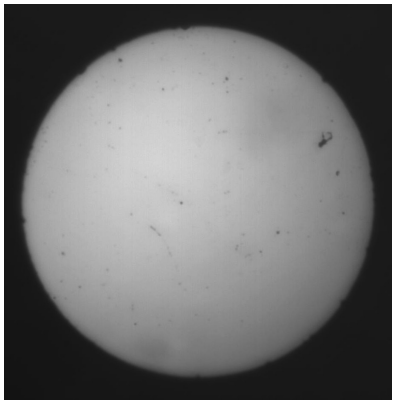

(b)

Figure 12: (a) Real-space imaging setup. The dichroic BS is a dichroic beamsplitter which is highly reflective for wavelength below 755 nm and highly transparent for wavelength above 755 nm. The luminescence from the sample is collected and collimated by the first lens and then refocused onto the entrance slit of the spectrometer. The spectrometer can either work in the imaging mode or the spectral mode. In the imaging mode, it projects the image on the entrance slit to its exit slit where a CCD is installed. In the spectral mode, it diffracts the wavelength resolved beam to the exit slit. (b) Real-space image of the sample surface obtained by illuminating the sample with a 'white' light lamp. The circular edge boundary of the sample is the aperture of the sample holder.

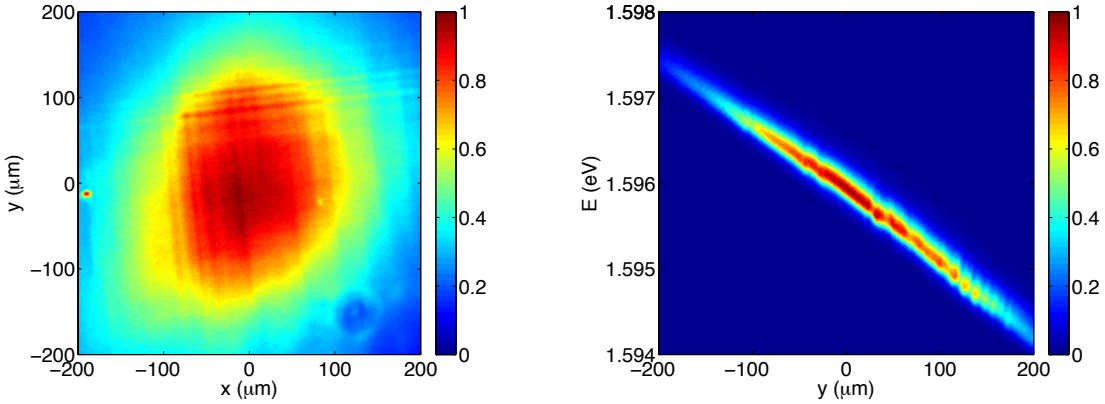

(a) (b)

Figure 13: Photoluminescence of lower polaritons and its energy spectrum. (a) Spatially resolved image of the polaritons created by a defocused pump beam from a laser working at 731 nm (1.696 eV) with a pump power. (b) Energy spectrum of the polariton luminescence from a slice at $x = 0$ μm of (a).

The energy of polaritons changes across the sample due to the cavity-width gradient.

3.3.2 Momentum space spectroscopy

The in-plane momentum of polaritons maps to the emission angle of the photons in the far-field. Thus the in-plane momentum of polaritons can be determined by measuring the emission angle of photons in the far-field. One way of getting the far-field image of polaritons, as illustrated in Fig. 14(b), is to use a lens to Fourier transform the near-field emission into the far-field. The polaritons are placed at the focal point of a convex lens, which focuses the photons emitted at the same angle to a single point on its focal plane. Therefore, the far-field image is formed on the focal plane and the in-plane momentum is mapped to coordinates on this plane. In our experiments, we implement this method with the setup illustrated in Fig. 14(b). Comparing to Fig. 12(a), a third lens is added into the system which uses the real space image formed by the first two lens as a source to form the far-field image on its

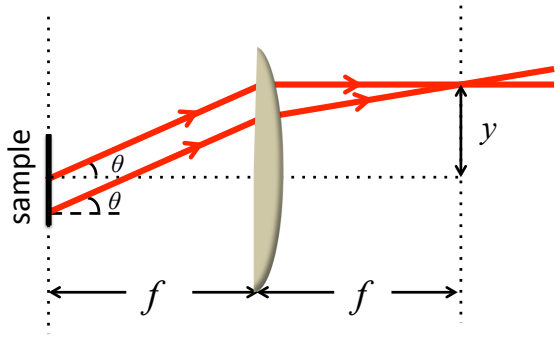

(a)

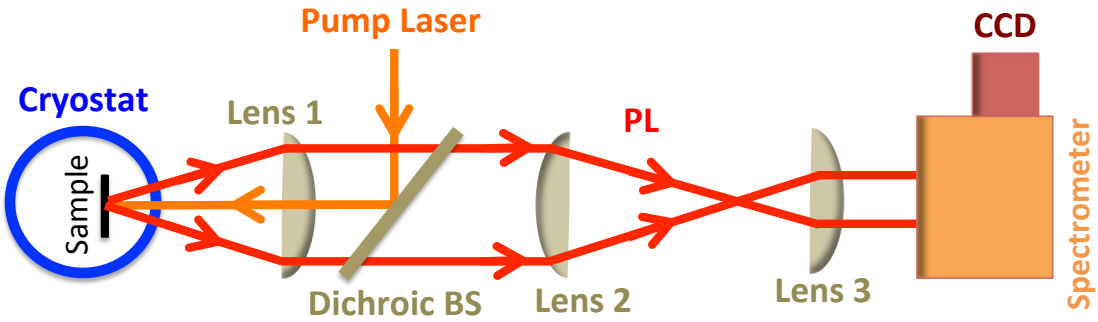

(b)

Figure 14: Momentum-space imaging setup. (a) When the sample is placed at the focal plane of the lens, the far-field image of the polaritons is formed on the other focal plane of the lens. The emission angle, θ, is mapped to the distance y to the to the center of the focal plane by $\tan\theta = y/f$. (b) Setup for the momentum-space imaging experiment. The image formed by the first two lens is used as a source for a third lens which projects the far-field image to the entrance slit of the imaging spectrometer.

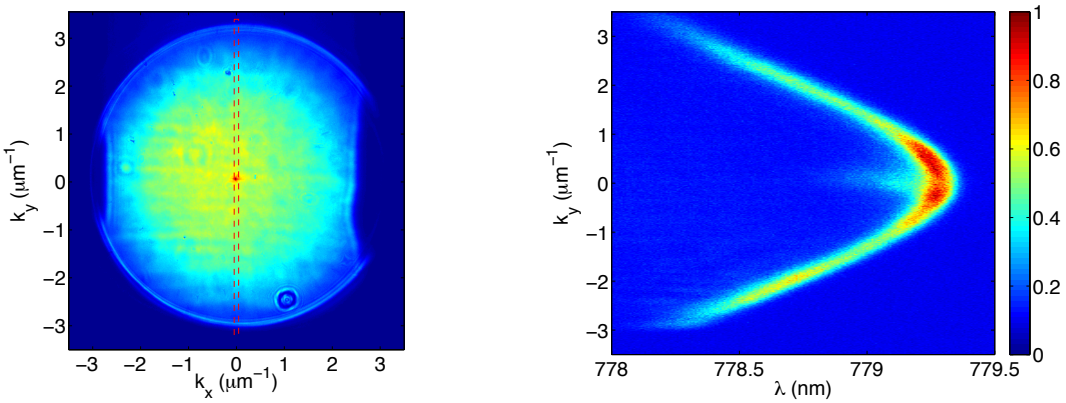

(a) (b)

Figure 15: Far-field image of polaritons and the spectrum. (a) Far-field image of the polaritons formed on the entrance slit of the spectrometer. (b) Energy spectrum of the central slice (enclosed by the red dashed box) of the far-field image.

focal plane. The entrance slit of the spectrometer is placed on the focal plane to collect the light. When the slit is fully open and the spectrometer is working in the imaging mode, a 2D far-field image is obtained (Fig. 15(a)). However, the energy can not be resolved in this mode. By closing down the slit, we can select a slice of the 2D far-field image and spectrally resolved it. Now, the horizontal axis becomes wavelength (energy) and the vertical axis becomes the vertical (y) component of the in-plane momentum. By doing this, a dispersion curve of the polariton is obtained.

3.3.3 Coherence Measurement

The first-order temporal coherence, or the coherence time (τ_c), of the polariton system is measured with a Michelson interferometer as shown in Fig. 16(a). Two plane mirrors (M2 and M3) are mounted on linear translation stages which have a travel range of 25 mm. Thus the maximum path length difference between the two arms is 100 mm, corresponding to a 333 ps time delay. The positions of the mirrors that give 0 time delay between the two

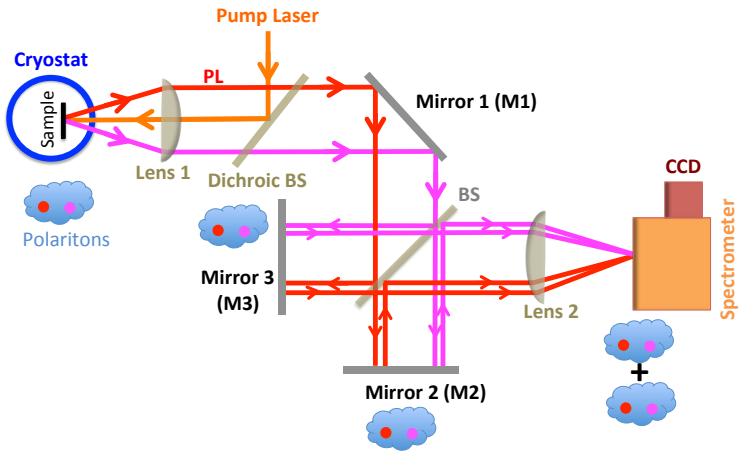

(a)

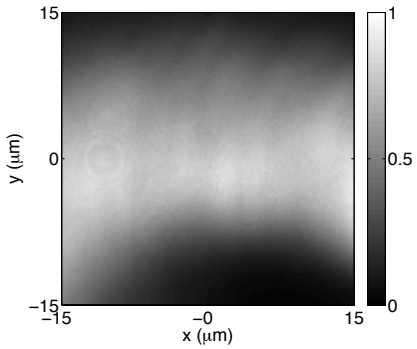

(b)

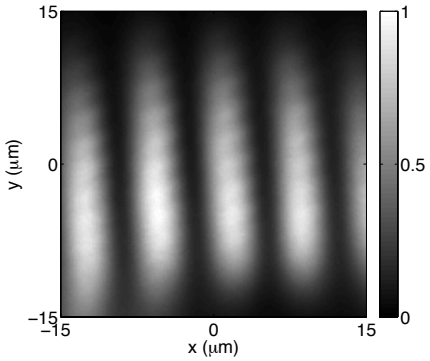

(c)

Figure 16: (a) Schematic of the setup for coherence time measurement. PL from the polaritons (red and purple dots) are collimated and then sent into the Michelson interferometer. In the drawing, the reflected beams are intentionally shifted from the beam path of the incident beam to make them visible to the eyes. In practice, the beam going through the beam splitter (BS) gets shifted due to the non-zero thickness of the BS. Lens 2 forms a real-space image of the polaritons for each beam from the interferometer, and overlaps them on the entrance slit of the interferometer. (b) Real-space image of a part of a polariton condensate. (c) The interference pattern recorded by the CCD camera. This data was recorded when the time delay between the two arms of the interferometer is 0.

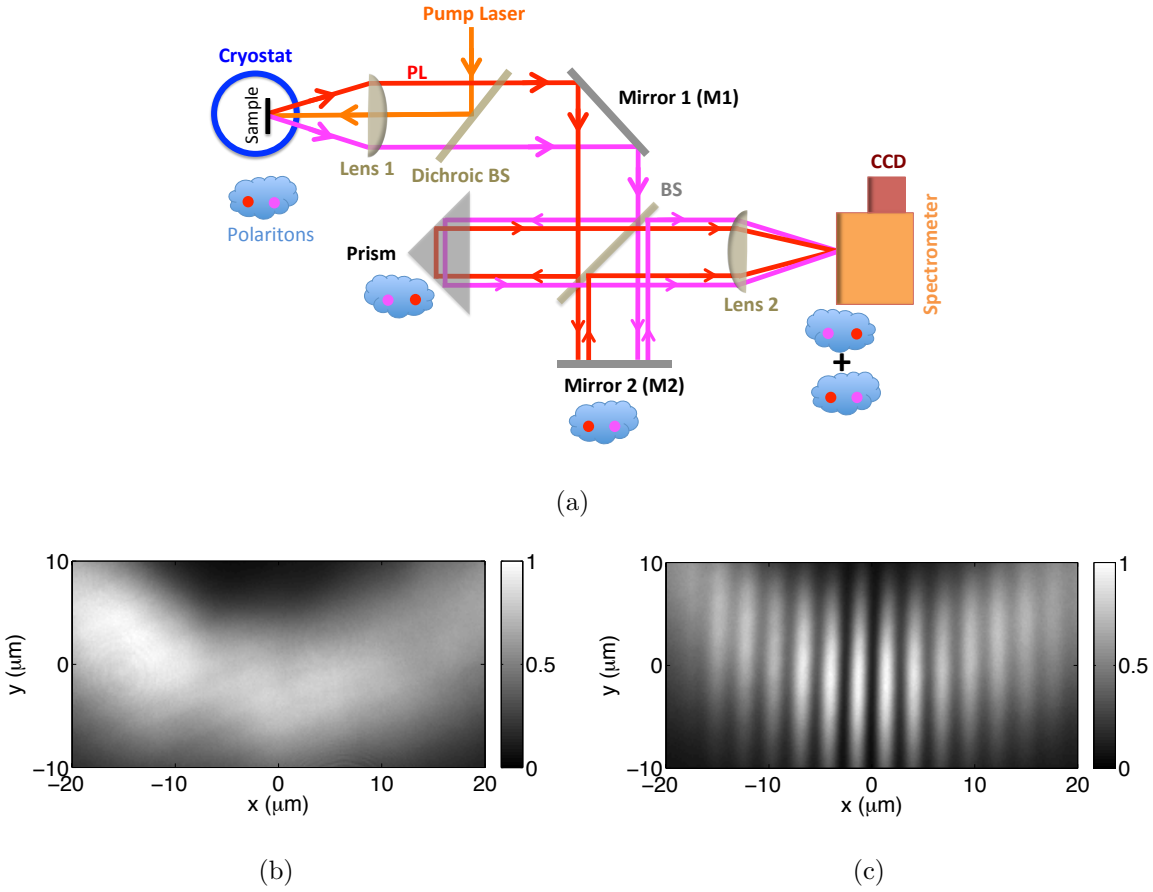

Figure 17: (a) Schematic of the setup for coherence time measurement. PL from the polaritons (red and purple dots) are collimated and then sent into the modified Michelson interferometer. One plane mirror (M3) is replaced by a right-angle prism. The prism flips the image of the polaritons by 180° with respect the axis perpendicular to the plane of incidence. When the images are overlapped at the entrance slit of the imaging spectrometer, polaritons from different positions interfere with each other. In the drawing, the reflected beams are intensionally shifted from the beam path of the incident beam to make them visible to the eyes. In practice, the beam going through the beam splitter (BS) gets shifted due to the non-zero thickness of the BS. (b) Real-space of a part of polariton condensate. (c) The interference pattern recorded by the CCD camera. It is created by interfere the polaritons in (b) with its image that flipped along the y axis.

paths is determined by sending a beam from a picosecond pulsed laser into the interferometer and overlapping them at the exit port of the interferometer. When taking measurements, the collimated beam of polariton PL is sent into the interferometer. After coming out of the interferometer, these two beams go through a focusing lens overlapping each other and generate a interference pattern at the focal plane of the lens. Fig. 16(b) shows the real-space image of a part of a polariton condensate. Fig. 16(c) is the interference pattern of these polaritons when the time delay between the two arms of the interferometer is zero. As one can see, there are bright and dark fringes across the whole image. The coherence time of the polaritons is determined by measuring the visibility of these interference fringes as a function of the time delay between these two beams. For a given time delay, Δt, between the two arms of the interferometer, the visibility of the interference fringes is defined as

$$v(\Delta t) = \frac{I_b(\Delta t) - I_d(\Delta t)}{I_b(\Delta t) + I_d(\Delta t)} \tag{3.1}$$

where I_b and I_d are the intensities of the bright and dark fringes, respectively.

In order to measure the spatial coherence, namely the coherence length (l_c), the time delay between the two arms of the interferometer is set to zero, and one plane mirror of the interferometer is replaced by a right angle prism (Fig. 17(a)). This prism gives a 180 degree reflection independent of the angle of incidence. In addition, it flips the incident beam along the axis that is perpendicular to the plane of incidence. When this beam is overlapped with the beam from the other arm of the interferometer, the spatially separated polaritons interfere with each other, gives us the spatial coherence information. Fig. 17(b) shows the real-space image of a part of a polariton condensate, and Fig. 17(c) is the interference pattern recored by the CCD camera. From Fig. 17(c), one can see that as the distance between the polaritons ($2|x|$) increases, the contrast between the bright and dark fringes decreases which implies that the polaritons becomes less coherent. By calculating visibility at different postions (x) in this Fig. 17(c), the coherence length l_c can be determined.

3.4 STRESS TRAP FOR POLARITONS

As discussed in Chapter 2, a uniform 2D system of bosons cannot undergo Bose-Einstein condensation at finite temperatures [58], because of long-range thermal fluctuations inherent to low-dimensional systems [53]. However, by applying a trapping potential to the system, one can introduce a lower bound for the momentum of such long-range thermal fluctuations and thus suppress their existence. Therefore, a true BEC can exist in a trapped 2D system of bosons [55, 56].

For microcavity polaritons, natural defects in the crystal might provide adequate trapping potential for the BEC to happen [15, 72]. But there are unavoidable drawbacks for this trapping method: the defects appear randomly in the sample, and they have random energy and spatial profiles. As a consequence, BECs are formed in discrete regions within the polariton cloud, and particle density and phase of the condensate are highly inhomogenous. In order to create a highly controllable trap for polaritons, several different methods that involve nano fabrication of the sample have been developed [59, 60]. In our experiments, we follow a different approach: creating harmonic traps for polaritons by applying stress on the microcavity sample. In this harmonic trap the first clear evidence of polariton BEC was established in 2007 [17].

3.4.1 Background Physics of Stress Trapping

Using stress to control the motion of excitons and free carriers was first demonstrated in bulk semiconductors [73, 74, 75]. The method of trapping excitons with stress in GaAs quantum well structures was first developed in our lab [76], and then adapted to microcavity structures [17]. When stress is applied on the microcavity, the energy of the excitons in the quantum well gets shifted. Meanwhile, the stress has negligible effect on the dielectric constants of the materials, so the cavity photon energy does not change. The polariton energy shifts as a result of the shifted exciton energy. The energy shift of the exciton as a function of stress is given by the Pikus-Bir deformation Hamiltonian [77]:

$$H_{PB} = a(\epsilon_{xx} + \epsilon_{yy} + \epsilon_{zz}) + b\left[(J_x^2 - J^2/3)\epsilon_{xx} + c.p.\right] + \frac{2d}{\sqrt{3}}\left[\frac{1}{2}(J_xJ_y + J_yJ_x)\epsilon_{xy} + c.p.\right] \quad (3.2)$$

where a, b, and d are deformation potentials, ϵ_{ij}'s are the components of stress-tensor, J's correspond to the spin states of the valence band ($m = \pm 3/2, \pm 1/2$), and $c.p.$'s are the cyclic permutations with respect to x, y and z. In our experiment, the stress is applied along the growth direction (z direction) of the sample, therefore

$$\begin{aligned} E_{PB} &= a(\epsilon_{xx} + \epsilon_{yy} + \epsilon_{zz}) - 3b(\epsilon_{zz} - \frac{1}{2}\epsilon_{xx} - \frac{1}{2}\epsilon_{yy}) \\ &= 3a\epsilon_{\text{hydro}} - 3b\epsilon_{\text{shear}} \end{aligned} \tag{3.3}$$

with ϵ_{hydro} the hydrostatic stress-tensor and ϵ_{shear} the shear stress-tensor. The shear stress will change the symmetry of the crystal lattice lifting the degeneracy of the bands. The band that is shifted to lower energy creates an energy minimum for excitons. The hydrostatic stress does not change the symmetry of the crystal but it can lower the energy of the band if it creates a hydrostatic expansion. On the other hand, if a hydrostatic compression is induced, the energy of the band will increase. In GaAs, the hydrostatic deformation potential is much larger than the shear deformation potential [78]. Therefore, in order to produce a trap for excitons in GaAs quantum wells, one needs to create a stress with no hydrostatic term, or to create a hydrostatic expansion. In our experiment, we take the second approach.

A schematic of the stress trap setup in our experiment is shown in Fig. 18. The stress is applied on the back side of the microcavity sample through a round tip stainless steel pin. In this geometry, the microcavity gets stretched as the sample bends under stress leading to a hydrostatic expansion of QWs. Fig. 19 shows the calculated exciton energy and the lower polariton energy for a 100 μm thick sample. A force of 0.8 N is applied on the sample by a pin with a 50 μm diameter tip. Material parameters such as deformation potentials used in the calculation are from Refs. [40, 79, 80]. As seen in Fig. 19(a), an exciton energy minimum is created by the stress while the cavity photon energy stays the same. In this particular case, the exciton energy at the center of the trap reduces by 9 meV changing the detuning from -6.8 meV to 2.2 meV. Fig. 19(b) compares LP energies with and without stress. Because of the cavity photon energy gradient, the trap for LP is shallower than that for excitons. On the lower energy side, the trap depth is 1 meV. PL of polaritons in this stress trap is shown in Fig. 20, which is in good agreement with the calculation. The bottom part of the stress trap can be well fitted by a harmonic trap $U = 1/2Kr^2$, where r is the distance to the center

of the trap and $K = 48.3$ eV/cm^2 is the spring constant of the trap. The effective mass of LP in the trap is $9.55 \times 10^{-5} m_0$ where $m_0 = 9.1 \times 10^{-31}$kg is the free electron mass. Thus the trapping frequency is $\omega_0 = 2.98 \times 10^{10}$ Hz and the quantum level spacing of the trap is $\hbar\omega_0 = 0.020$ meV. The sample temperature is maintained at 10 K in the experiment, the corresponding thermal energy of polaritons is $k_B T = 0.86$ meV. Therefore, the energy levels in the trap can be approximated as a continuum.

3.4.2 Advantages of Stress Trapping

The method of stress trapping has several advantages over other trapping methods that rely on nanofabrication of the sample [59, 60]: the position and depth of the stress trap can be actively tuned, while when the trap is created by nano fabrication it can not be changed once the fabrication is done. The stress trap provides a way of actively adjusting the energy detuning between the photon and the exciton. As a result, the properties of polaritons such as interaction strength and lifetime can be changed by stress as they all depend on detuning. For example, as the detuning changes from negative to positive the exciton fraction of the LP increases, the interactions between LPs become stronger and stronger and the LP gas gets better thermalized. Fig. 21 shows this change through the spectrally resolved momentum space images of LP at $x = 0$ μm in Fig. 19(b) before and after the stress is applied. Without stress, the detuning is -6.8 meV at this position which gives an exciton fraction of 0.26. The interaction between polaritons is not strong enough to make them thermalized, therefore, they move ballistically in the sample occupying only a small section of the dispersion curve (see Fig. 21(a)). With the detuning changed to 1.9 meV by stress, the exciton fraction of the LP increases to 0.58. The interaction between polaritons now becomes strong enough for them to thermalize with each other. This is illustrated by the momentum distribution in Fig. 21(b), where polaritons occupy a wide range of the momentum states.

To demonstrate the thermalization of polaritons in the stress trap, we measured the temperature of polaritons in a stress trap similar to the one shown in Fig. 20. At the center of this stress trap, the detuning is 4 meV and the exciton fraction is 0.65. Fig. 22(a) shows the energy-resolved real-space image of polaritons in this trap. These polaritons are

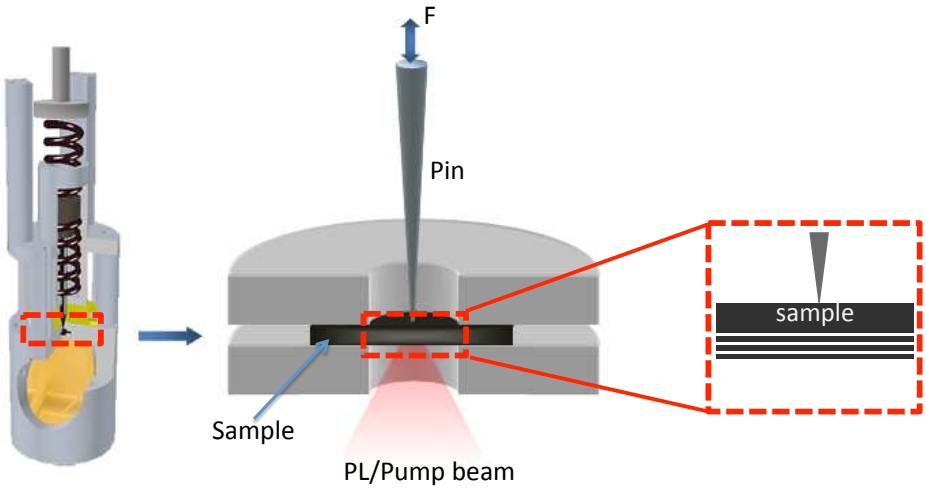

Figure 18: Schematic setup for the stress trap. The sample is clamped on the sample holder by a Telflon plate which has a hole at the center to allow the pin go through it. Stress is applied on the back surface of the sample through a spring-loaded pin. The sample will bent downward under the influence of the stress. While the region near the back surface of the sample gets compressed, the microcavity which is near the front surface of the sample gets stretched.

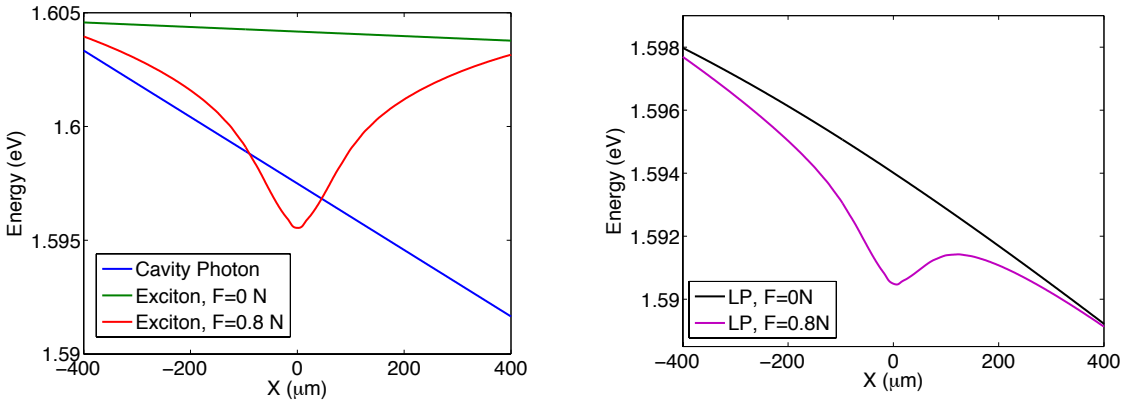

(a) (b)

Figure 19: Calculated energy of the excitons and polaritons without and with force applied on the back surface of the sample. (a) Energy of the excitons without (green) and with a stress of 0.8 N (red) applied at $x = 0$ μm. The photon energy does not change with stress (blue). (b) Energy of the polaritons with (purple) and without (black) stress. A trap in the vicinity of stress center is formed for the polaritons. Due to the cavity-width gradient, the right side of the trap is lower than the left side. The effective depth of the trap is 1 meV.

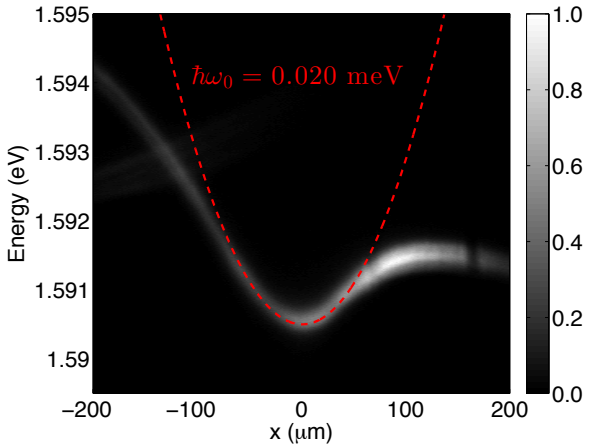

Figure 20: PL of lower polaritons when a stress of 0.8 N is applied on the sample. The pin touches sample at $x = 0$.The red dashed line is a harmonic trap fit to the bottom region of the stress trap. It gives a quantum level spacing of $\hbar\omega_0 = 0.020$ meV.

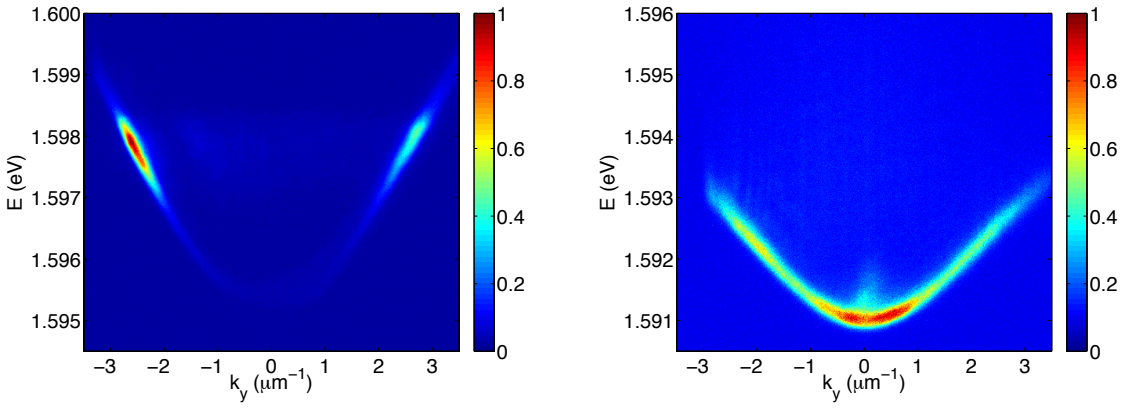

(a) (b)

Figure 21: Spectrally resolved momentum space PL of LPs at $x = 0$ in Fig. 19(b) without and with stress applied on the sample. (a) PL of LPs without stress; the detuning is -6.8 meV. (b) PL of LPs with a force of 0.8 N applied on the sample; the detuning is 1.9 meV.

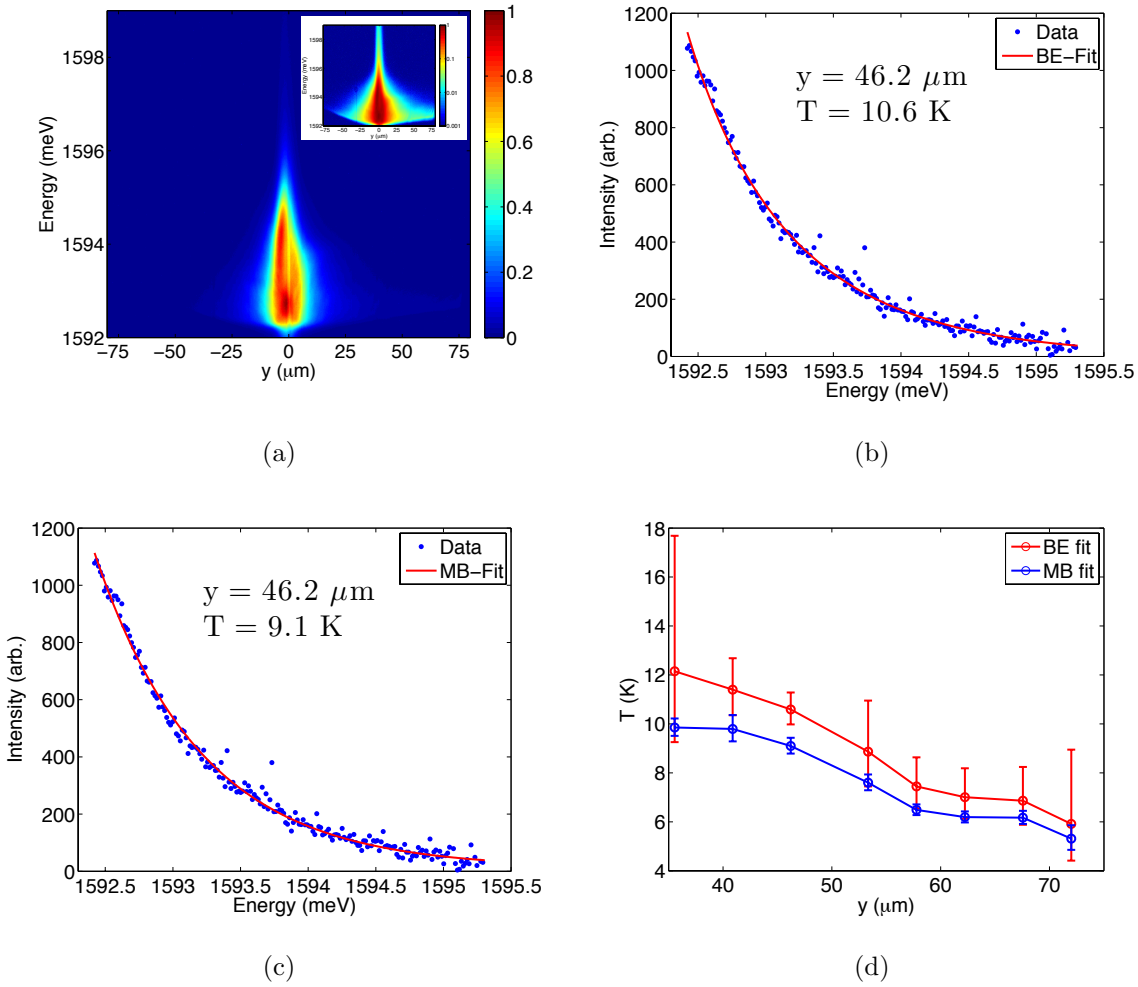

Figure 22: Temperature of polaritons in the stress trap. (a) The energy-resolved PL of polaritons in the stress trap with the pump laser focused to $y = 0$. The inset shows the same image but in a log-scale. (b) The fitting (red line) of the polariton intensity (blue dots) as a function of energy with the Bose-Einstein distribution. The data come from polaritons at $y = 46.2$ μm in (a). (c) The fitting of the same data in (b), but with the Maxwell-Boltzmann distribution. (d) The temperature of polaritons at different locations in the sample obtained by fitting the data with Bose-Einstein distribution (red) and Maxwell-Boltzmann distribution (blue), respectively.

created non-resonantly by a laser focuscing to a spot of 8 μm diameter at the center of trap ($y = 0$ μm). Due to the repulsion from excitons, polaritons move away from the excitation spot and fill in the trap. The polariton population outside the excitation spot is more visible in the inset of Fig. 22(a), which uses a log scale for the PL intensity.

In order to determine the temperature of polaritons in the trap, we took slices of Fig. 22(a) along the energy axis at different locations in the trap. Then for each slice, we fitted the intensity of the PL as a function of energy with Bose-Einstein (BE) distribution and Maxwell-Boltzmann (MB) distribution, respectively. The temperature is used as one of the fitting parameters in the data fitting. Fig. 22(b) and Fig. 22(c) show the type results of the data fitting. In these two figures, the data from the slice at $y = 46.2$ μm of Fig. 22(a) is fitted the Bose-Einstein distribution with a temperature of 10.6 K, and to the Maxwell-Boltzmann distribution with a temperature of 9.1 K. Good agreement between the data and the thermal distribution functions are obtained in both case. This implies that the polaritons are in thermal equilibrium with each other. The fact that the data fits well with both the Bose-Einstein distribution and the Maxwell-Boltzmann distribution is because the density of polaritons are well below the quantum degenerate density, and these two distributions are nearly the same at such low density. Fig. 22(d) shows the temperature of polaritons at different locations in the trap. It is interesting to notice that as polaritons move away from the excitation spot, they become colder. This is analogous to the free expansion of a gas; the gas becomes colder as it expands.

An important feature of this result is that the temperature of the polaritons is nearly the same as the temperature of the crystal lattice, which is ~ 9.5 K in this experiment. This indicates that polaritons are in thermal equilibrium with the crystal lattice, which has not been observed before except when the polaritons are extremely positively detuned (exciton fraction ~ 0.90) and are near the quantum degeneracy density [25]. The fact that our polaritons are only slightly positive-detuned and are at a density far below the degeneracy density makes this observation even more surprising. We ascribe thermalization between the polaritons and the lattice observed here to the extraordinarily long lifetime of polariton in our sample. In previous experiments, the polariton lifetime is in the range from 4 ps to 10 ps [15, 17]. While, the typical polariton-phonon scattering time in microcavity is 50 ps

[45]. Therefore, these short lifetime polaritons can not reach thermal equilibrium with the lattice via scattering with phonons, even when their density is high enough to form a BEC. For example, in Ref. [15] and [17] polaritons were found to reach thermal equilibrium with each other at effective temperatures of 19 K and 97 K respectively, while the samples were maintained at 4 K. Being able to thermalize with the lattice allows the possibility for tuning the temperature of the polariton system by changing the lattice temperature. This opens the door to study temperature dependent physics of polaritons, such as determining the phase diagram of polaritons [46].

Another important effect of the stress is that it can lift the degeneracy of the polariton state: the stress splits it into two linearly polarized states with different energies [81, 82]. This effect has been thoroughly studied in Ref. [81]. It was found that the splitting of the polariton states is primarily due to the splitting of exciton states, which comes from the electron-hole exchange interaction and the mixing of the light- and heavy-hole excitons induced by stress. Fig. 23 shows the polarization-resolved image of polaritons in the stress trap. A splitting of the polariton can be clearly seen when the polarizer allows both linear polarizations to pass through. Such a splitting of the polariton states plays an important role in our experiment, as we will discuss in Chapter 7.

3.5 EXCITON BARRIER FOR POLARITONS

In a non-resonant pumping experiment, an exciton cloud is created at the the pump spot. The excitons, with mass 10^4 times higher than the polaritons, are essentially static as seen by the polaritons. The repulsive interaction between the excitons and polaritons makes the exciton cloud a potential barrier for polaritons. The properties of this potential can be well modeled as a mean-field shift proportional to the local density of the excitons $\Delta U \sim g_{\mathrm{ex}} n_{\mathrm{ex}}(r)$, with g_{ex} and n_{ex} are the polariton-exciton interaction strength and exciton density. Fig. 24(a) shows the energy spectrum of polaritons created with a defocused non-resonant pumping laser. In this case the density of excitons is low in the pump region; therefore the blue shift is negligible and the polariton energy varies across the sample due to the cavity photon

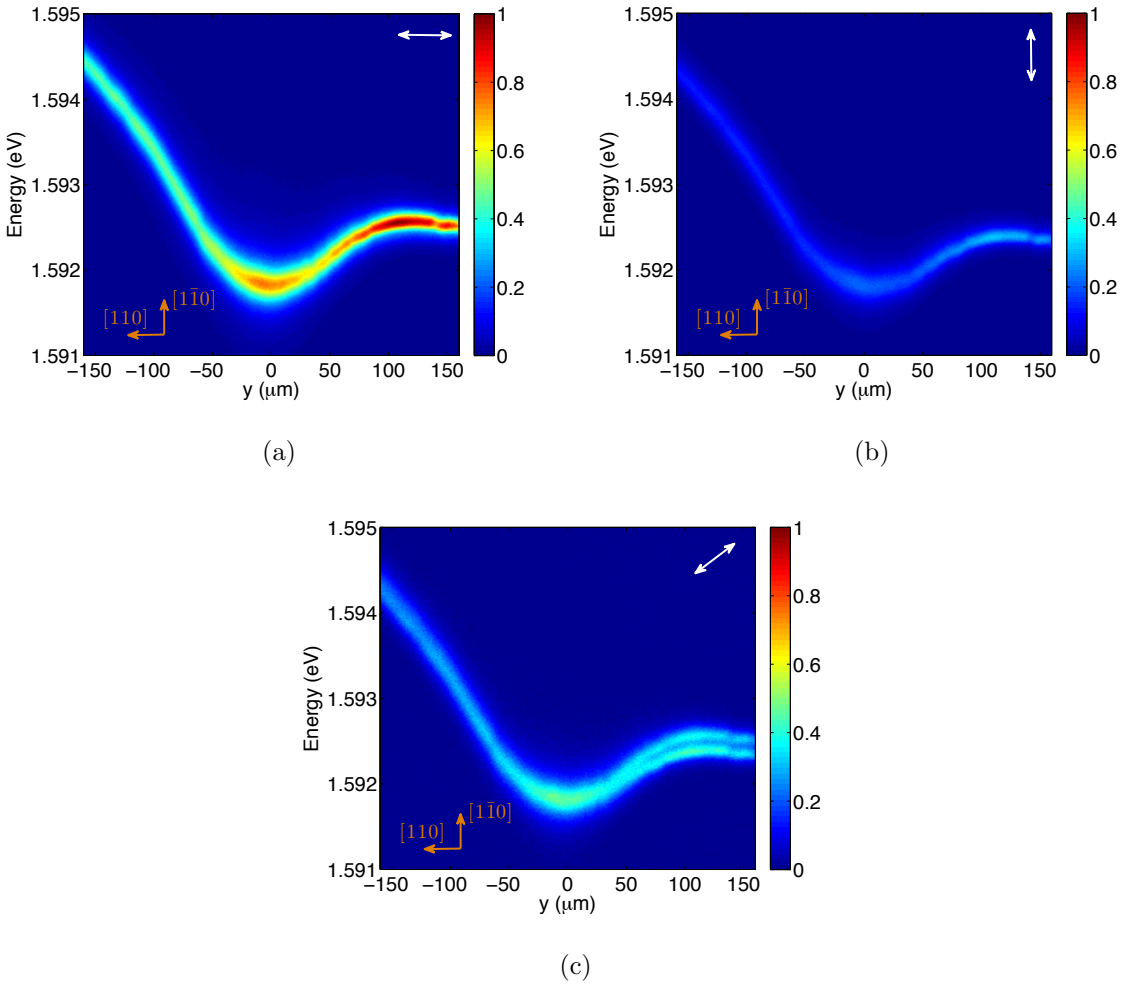

(a)

(b)

(c)

Figure 23: Polarization resolved PL of polaritons in the stress trap. The white double arrow represents the direction of linear polarization of the PL in (a) the horizontal direction, (b) the vertical direction and (c) the 45° direction. The brown arrows in the figures represent the directions of the crystal axis of the sample.

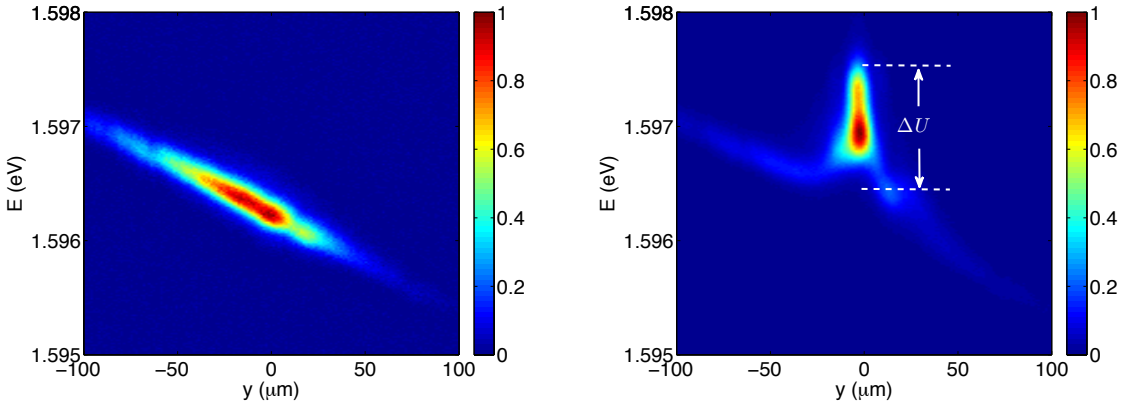

(a) (b)

Figure 24: Exciton barrier for polaritons. (a) When the pump laser beam is defocused, low density polaritons are created in a region of about 100 μm in diameter. The energy of polaritons changes due to the cavity-width gradient. (b) The laser beam is focused down to a spot of 15 μm in diameter at y=0 μm. The density of excitons is high at the pump spot, and the polaritons are shifted to higher energies.

energy gradient. Fig. 24(b) shows the polariton energy spectrum when the laser spot is focused down to a spot of 15 μm in diameter. Here the density of excitons at the pump spot is high and it shifts up the polariton energy significantly, therefore a potential barrier is obtained.

This method allows the possibility of creating an arbitrary potential landscape for polaritons, because both the height and shape of the barrier can be precisely controlled by the pump laser. For example, a 1D harmonic trap can be created by bringing two exciton clouds close together [20]. Using a ring-shaped pump beam, a 2D harmonic trap can be created [21]. In Chapter 5, I will discuss our experiment with an exciton barrier on top of the potential due to cavity-width gradient [22]. In Chapter 6, I will show that by combining the exciton barrier with the stress trap, we can create a ring-shaped trap in which a new type of half-quantized circulation of polaritons is observed [23].

4.0 COHERENT FLOW AND BEC OF POLARITONS WITH LONG LIFETIME

In this chapter, I will present our experiments on the long-lifetime polaritons created by the nonresonant pumping method. The extraordinarily long lifetime, 270 ps at resonance, enables the polaritons to move over hundreds of microns away from the point of creation. The polaritons exhibit very rich dynamics under the influence of the exciton barrier created by the pumping laser and the potential due to the cavity-width gradient. In the low-density regime, polaritons behave like classical particles propagating ballistically over hundreds of microns in the microcavity. The ballistic motion of polaritons provides a new way of measuring the polariton lifetime. In the moderate density regime, a large fraction of the polariton population enters into a dissipationless flow over hundreds of microns. Polaritons in this flow are coherent, and the coherence is maintained as they propagate in the sample. This allows the possibility of studying quantum coherence on macroscopic scales. When the polariton density is above a critical threshold, they make a sudden transition from the flow state to a trapped state in the quasi-1D trap formed by the exciton barrier and the cavity gradient. This transition is accompanied by a very sharp decrease of the polariton line width, and Bose-Einstein condensation to the zero in-plane momentum state. This transition is much sharper than transitions observed before with short-lifetime polaritons. The trapping effect observed here provides a new way of engineering potentials for polaritons.

The results presented in this chapter have been published in the paper "Dissipationless flow and sharp threshold of a polariton condensate with long lifetime," Physical Review X **3**, 041015 (2013) [22] I measured the real-space and momentum-space images of the polaritons at different pump powers, which were shown in Fig. 1 and Fig. 2 in the paper. I also contributed to the analysis of the data and the writing of the paper. The coherence time measurement of

the polaritons shown in Fig. 28 is published in the paper "Long-range ballistic motion and coherent flow of long-lifetime polaritons," Physical Review B **88**, 235314 (2013) [48]. Besides the coherence time measurement, I also contributed to the simulation of the evolution the polariton state which was shown in Fig. 9 of this paper.

4.1 EXPERIMENTAL METHOD

In the experiments, we chose a region with negative detuning on the sample. In this region, polaritons have relatively weak but nonzero interactions with each other and with the lattice. This allows the polaritons to move over large distances with very few scatterings. On the other hand, when the particle density is high, the polaritons still have enough interaction between themselves to exhibit many-body effects.

The sample was mounted in a cryostat with the temperature maintained at 10 K by a continuous flow of helium vapor. It was pumped by a single-mode continuous wave diode laser working at 707 nm, at the third minimum of the reflectivity above the microcavity stop band. The laser beam was focused down to a spot of 12 μm in radius. At the pumping position, the detuning was $\Delta = -3.2$ meV. The PL from the polaritons is detected and analyzed by the real space and momentum imaging setups discussed in Chapter 2.

4.2 BALLISTIC MOTION OF POLARITONS OVER MACROSCOPIC DISTANCE

Fig. 25 shows the energy-resolved real-space and momentum-space images of polaritons at a pumping power of 1 mW. The top picture of Fig. 25(a) is the PL from hot carriers created by the pumping laser. Its profile shows the spatial extent of the excitation region where the polaritons are generated. It also shows that the excitons remain where they are created. The bottom picture is the PL from polaritons with $k_{||} \sim 0$ ($\pm 2^\circ$ angle of acceptance). It shows that polaritons created at the pumping spot ($y = 0$ μm) move uphill against the

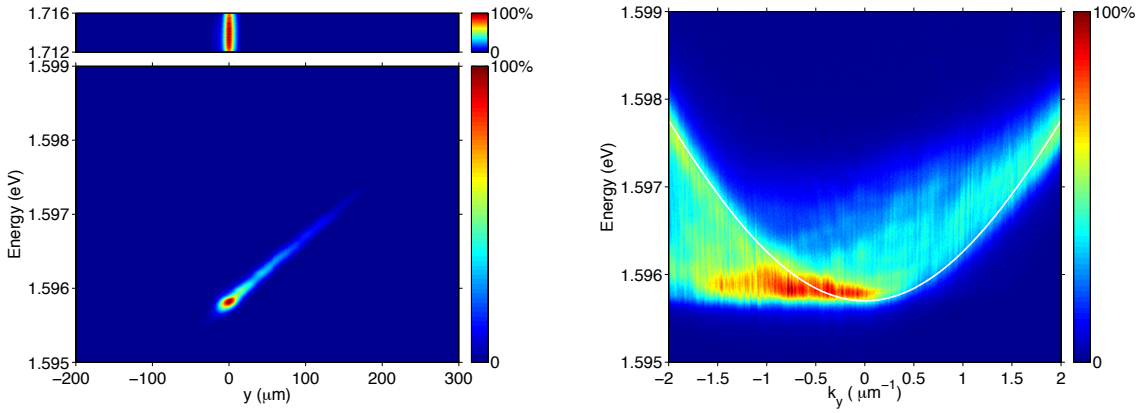

(a) (b)

Figure 25: Energy-resolved real-space and momentum-space images of polaritons when the pump power is 1 mW. (a) The image on the top is the PL from the hot carriers created by the non-resonant pumping laser. The bottom picture is the energy-resolved real-space of polaritons with $k_{||} \sim 0$ ($\pm 2^\circ$ angle of acceptance). The polaritons are created at y = 0 μm by the excitation laser. (b) The momentum-space image of the polaritons in the field of view of the imaging system. The white curve is the single-particle energy dispersion of polariton at the pump spot (y = 0 μm) at low density. From Ref. [22].

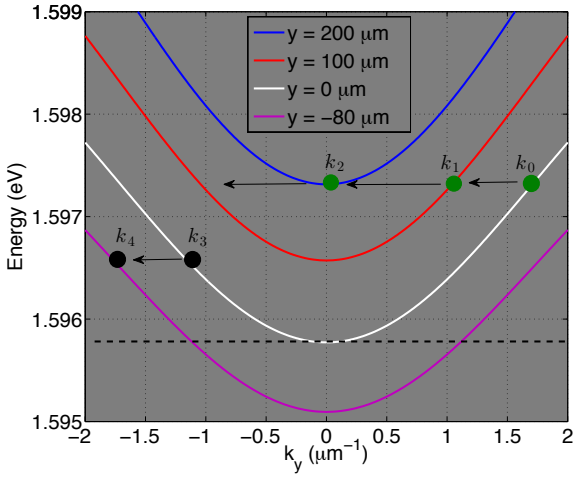

Figure 26: Illustration of the mechanism for the smearing of the polariton dispersion in Fig. 25(b). Curves with different colors are the single-particle dispersions of polariton at different positions in Fig. 25(a). The blue circle on the white curve represents the a polariton leaving the pump region with an initial momentum of k_0 in the up-hill direction. As it moves further away, it decelerates to lower momentum states (k_1, k_2). When its momentum reduces to 0 (k_2), it enters the aperture of the real-space imaging setup. The dark circle on the white curve represents a polariton moving in the down-hill direction with an initial momentum k_3. As it moves away, its gets accelerated to higher momentum state (k_4). The dashed line corresponds to the lowest energy of polaritons created at the pump spot. It determines the cutoff of the polaritons energy as seen in Fig. 25(b).

cavity gradient to places as far as 200 μm away. In fact, propagation of polaritons over 1 mm is observed when the pumping spot is moved further into the photonic side of the sample [48, 49]. At such low pumping power, the density of excitons in the pumping region is low; it does not lead to a noticeable blue shift of the polariton energy. It is interesting to notice that the polaritons seem to gain energy while moving uphill, which is counterintuitive. In order to understand this phenomena, we need to analyze the momentum-space distribution of the polaritons.

Fig. 25(b) shows the energy-resolved momentum-space image of the polaritons. The white curve represents the single-particle energy dispersion of polaritons at the pump spot at low density. This spectrum "smears" out from the single-particle dispersion curve for two reasons. First, it spatially integrates the emission from the polaritons as they move in the cavity plane; this spectrum is a sum of dispersion curves of polaritons at all different positions on the sample. The spatial gradient of the cavity width leads to a gradient of detuning which shifts these dispersion curves relative to each other, resulting in broadening of the width of the spectrum. The second reason for the spectrum to smear out is that polaritons experience a force, $F = -\nabla U(x)$, due to the spatial gradient of the cavity width. Under the influence of this force, polaritons accelerate in the downhill direction, i.e. gain momentum in the $-y$ direction, which smears the spectrum leftward.

These two effects are illustrated in Fig. 26. Here I plot the dispersion curves at different locations on the path of the polaritons in Fig. 25(a). The nonresonant excitation laser generates polaritons in a wide range of in-plane momentum states in the pumping region. These polaritons then move away from the pumping spot and populate dispersion curves at different locations on their path. Polaritons with initial momentum in the uphill direction (the right half of the white curve) will be decelerated by the cavity gradient. As they move uphill, their kinetic energy converts into potential energy. This process is illustrated by the trajectory of the green dot in Fig. 26. These polaritons keep moving uphill until they reach positions where all their kinetic energy has converted into potential energy. We call these positions where polaritons lose all their kinetic energy the "turnaround points". After reaching turnaroud points, they start to move in the opposite direction, namely the downhill direction, under the influence of the cavity gradient. Emission from these polaritons

appears in the region above the dispersion curve in Fig. 25(b). In particular, emission from polaritons at turnaround points has zero in-plane momentum which gives the PL observed in Fig. 25(a). Polaritons with initial momentum in the downhill direction (the left half of the white curve) will be accelerated by the cavity gradient. Their potential energy converts into the kinetic energy as they move away from the pumping spot. This process is illustrated by the trajectory of the black dot in Fig. 26. As a result, they emit photons with larger in-plane momentum which appears in the region below the dispersion curve in Fig. 25(b).

In this low-density regime, the polaritons are essentially moving ballistically, with little scattering with each other. Scattering with the lattice phonons is also suppressed by their very light mass [45]. The ballistic motion of polaritons observed here provides a new method for measuring polariton lifetime. Ideally, the polariton lifetime can be directly determined by measuring the decay of polariton population over time. But there are various reasons making it difficult to do so [48]. If the polaritons are created nonresonantly, there will be a reservoir of excitons in the pumping region which constantly replenishes the polariton population. As the excitons live much longer than polaritons, the decay of polaritons will be mostly determine by the time for excitons to cool down and form polaritons. Therefore, the measured lifetime will be longer than the lifetime of a single polariton. On the other hand, if the polaritons are created resonantly, there will be a large amount of reflected laser light which can not be completely eliminated. In addition, the decay of polaritons at the particular state will be affected by the scattering of polaritons into other states. Furthermore, a coherent polariton state produced by a resonant excitation can have superradiant emission which enhances the decay of polaritons. These two mechanisms make the measured lifetime shorter than the lifetime of a single polariton.

All these difficulties, however, can be circumvented by the ballistic motion of polaritons in our sample. The exciton reservoir does not affect the polariton population after polaritons move away from the pumping region. Scattering processes that take polaritons out of the interested state are also suppressed. The decay of polariton can be determined by comparing the PL intensity at different locations on its trajectory. Based on this idea, the lifetime of polaritons at resonance was measured to be 270 ps. Detailed description of the measurement and data analysis is presented in Ref. [48, 49].

4.3 TRANSITION TO COHERENT FLOW

As the pumping power increases, the energy distribution of the polaritons becomes more and more peaked, until a large fraction is all at a single energy. Fig. 27 shows the real-space and momentum-space images of polaritons under the same condition as that in Fig. 25, but the pumping power is 34 mW. In Fig. 27(a), the $k_y = 0$ polaritons only appear at the pumping spot and at $y = 210$ μm in the uphill direction. Polaritons at these two locations are at the same energy. At the pumping spot, the polariton energy is 2 meV higher than that in the low-density case (Fig. 25(a)). This energy blue shift is caused by the repulsive interaction between polaritons and excitons in the pumping region. At such high pump power, the density of excitons is very high leading to a significant blue shift of the polariton energy. The excitons, with a mass of 10^4 times larger than the polaritons, are static as seen by the polaritons. They can be treated as a static barrier for polaritons. The properties of this potential barrier can be modeled as a mean-field shift proportional to the local density of polaritons. This effect has been seen before, for example in Refs. [24, 20]. The dashed white line in Fig. 27(a) shows the height and spatial extend of the exciton barrier, on top of the potential due to the cavity-width gradient.

After being created on top of the exciton barrier, polaritons move away from the pump region due to the repulsion from excitons. They gain momentum as they rolling down from the exciton barrier. Those accelerating uphill appear as a bright spot at $k_y = 1.75$ μm^{-1} in Fig. 27(b), while the ones accelerated downhill appear at $k_y = -1.75$ μm^{-1} in the same figure. But they are not visible in the real-space image as the aperture of the imaging system is restricted to $k_y \simeq 0$. As they continue moving in the cavity plane, those moving downhill will keep accelerating staying outside of the field of view of the imaging system all the time. Others that are moving uphill will slow down to $k_y = 0$ when they reach the turnaround point at $y = 210$ μm, becoming visible again in our real-space imaging system. When the light emitted from the creation point and from the turnaround point are overlapped, we see interference fringes when there is a time delay of 140 ps (Fig. 28(a)), indicating that the propagation is coherent. The time delay corresponds to the the time for the polaritons to travel from the creation point to the turnaround point. The measured coherence time of the

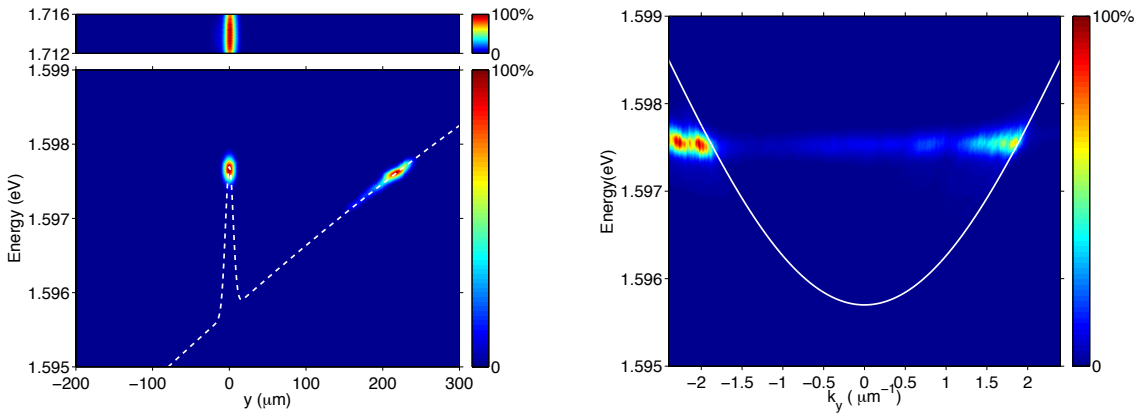

(a) (b)

Figure 27: Energy-resolved real- and momentum-space images of polaritons when the pumping power is 34 mW. (a) The white dashed line represents the exciton barrier on top of the potential due to cavity-width gradient. (b) The momentum-space image of polaritons under the same condition as that in Fig. 25(b), except the pump power is 34 mW. From Ref. [22].

polariton beam is approximately 40 ps; the coherence is preserved over a travel distance of 200 μm.

Fig. 27(b) shows that the polaritons remain monoenergetic as they propagate in the sample. This indicates that there has been no significant loss of energy of the particles over macroscopic distances. The single-mode behavior observed here occurs when one state is selected out of the continuum of 2D k state, as opposed to discrete trapped states as in Refs. [24, 20].

As discussed above, the monoenergetic, coherently flowing fraction of the polaritons increases as the density increases, until almost the entire polariton population goes into this flow. We interpret this redistribution as coming about because of the Bose-Einstein statistics of the polaritons, which causes the polaritons to increasingly accumulate in their ground state at their point of creation as the density is raised, due to the stimulated scattering final-state factor $(1 + N_f)$ [45]. There is no other mechanism that can cause this kind of nonlinear change in the polariton-energy distribution. Once the polaritons are in their ground state at the point of creation, they stream away from the creation spot, since there are no confining boundaries to their flow. The polaritons far from the creation spot have much lower density as they stream away. In this regime, their interactions are too weak to redistribute their energies; they simply flow ballistically with nearly no scattering for hundreds of microns. Thus, while they may start out as a quasicondensate at the creation spot, once they are in the ground state, they can simply flow coherently without scattering.

A streaming coherent flow of polaritons has also been reported before under nonresonant excitation [14, 24, 130, 84, 86], but with short-lifetime polaritons. In that case, there was also an acceleration of a coherent propagating state away from the potential-energy peak created by the exciton cloud, but only over a very short distance near the laser-excitation spot; there was also some degree of multimode behavior. In the present experiments, the long lifetime of the polaritons allows them to propagate completely away from the laser-generation spot, all the way to the point at which they turn around and come back in the potential gradient created by the cavity.

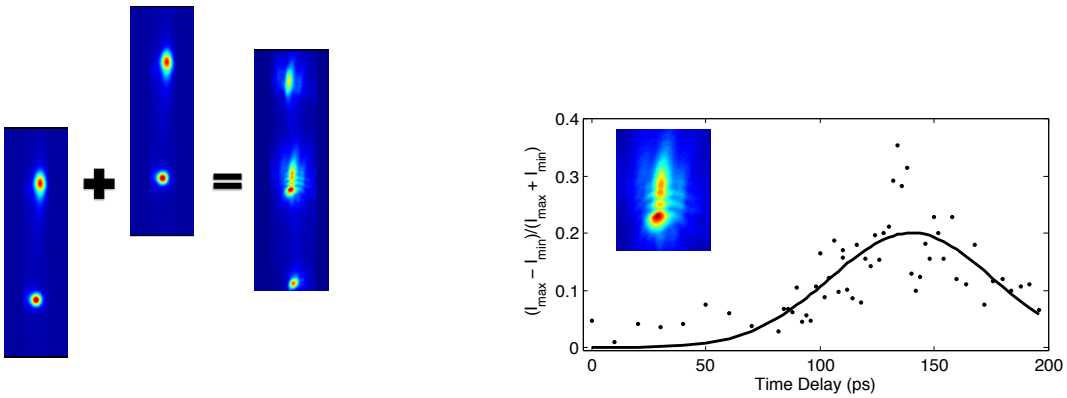

(a) (b)

Figure 28: Measurement of the coherence between the polaritons at the pump spot and the turn around point. (a) The images of the polaritons at the pump spot (lower circular spot) and the polaritons at the turn around point are overlapped by using the coherence time measurement setup in Fig. 16(a). (b) The visibility (dots) of the interference pattern as a function of the time delay between the two arms of the interferometer in Fig. 16(a). The black curve is a Gaussian fit to the data, which gives a coherence time of 37.5 ± 3.3 ps. The visibility is maximized at a time delay of 140.2 ± 2.8 ps. From Ref. [48].

4.4 SHARP TRANSITION TO TRAPPED STATE

The energy of the coherently propagating polaritons increases as the pump power increases. But when the pump power exceeds a critical threshold, the energy of the polaritons suddenly drops as shown in Fig. 29(a). The polaritons drop to the ground state of the quasi-1D trap created in the nook between the exciton cloud and the potential of the cavity gradient. The polariton cloud now has a very compact spatial profile with a radius of approximately 5.5μm. The momentum-space image (Fig. 29(b)) shows that the polaritons all go into the state with $k_y \simeq 0$. Therefore, a polariton condensate is formed in this quasi-1D trap. By measuring the intensity of emission from polaritons with $k_y = 0$ [22], we notice that this transition from the coherent propagating state to the condensate is very sharp. In fact, no equivalently sharp transition has been observed before in experiments with short-lifetime polariton systems [15, 17, 85]. We also measured the coherence time of this condensate, the result shows that it is greater than 280 ps which is the limit measurable by our Michelson interferometer.

The mechanism responsible for this sudden drop of polariton energy and the transition from flow to a trapped state is still not fully understood. We can make several observations, however. First, as mentioned earlier, the polaritons have nearly no interaction with the lattice phonons [45], and scattering with impurities are elastic which does not change their energy. Since the excitons at the pumping spot are 10^4 times heavier than polaritons, scattering with excitons will also be effectively elastic and will not change the polariton energy. On the other hand, the polariton-polariton scattering is not negligible, even away from the high-density pumping spot. We can see that the energy of the trapped state in Fig. 29(a) is 0.16 meV above the bottom of the trap. This energy shift comes from pure polariton-polariton interaction, since the polaritons have moved away from the exciton cloud sitting at the pumping spot. It may be that at high density, the polaritons returning from the turnaround point [seen in Fig. 27(a)] collide with the polaritons streaming outward from the creation spot, giving them a new channel for energy redistribution.

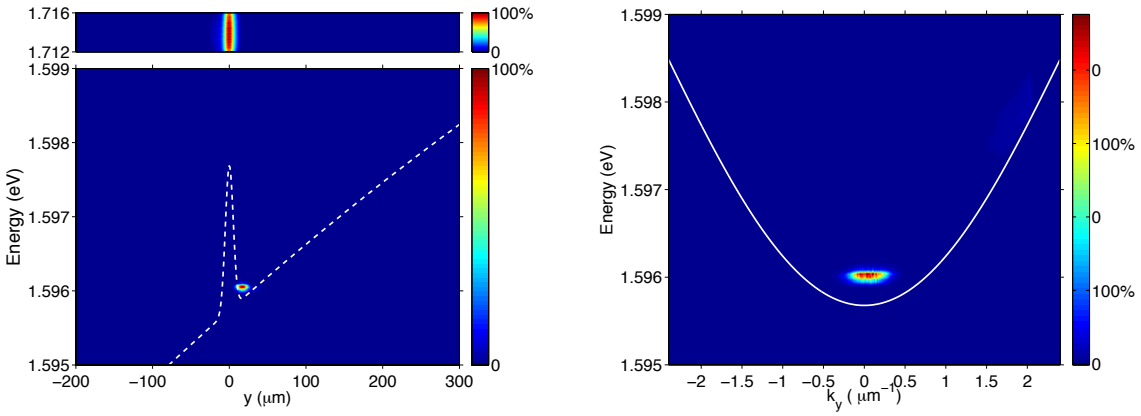

(a) (b)

Figure 29: Energy-resolved momentum-space and real-space images of polaritons when the pumping power is 44 mW. (a) The image on the top is the PL from the hot carriers created by the non-resonant pumping laser. The image on the bottom is the energy-resolved real-space image of polaritons with $k_{||} \sim 0$ ($\pm 2^\circ$ angle of acceptance). (b) The energy-resolved momentum space of polaritons. From Ref. [22].

5.0 CONDENSATION OF POLARITONS IN A RING TRAP

In this chapter and the next chapter, I will present my experiments on long-lifetime polaritons in a more complicated trap geometry — a ring-shaped trap. I will discuss our efforts in creating a polariton ring condensate in this current chapter. The next chapter will focus on the interesting properties of the ring condensate.

Condensates in a ring-shaped trap, analogous to superconducting rings, have received much attention recently [87, 88, 89, 90, 91, 92, 93, 94]. In ultra-cold atoms, ring condensates have been used to study various aspects of superfluid physics, such as persistent current, superfluid phase slips and hysteresis loop of superfluid [88, 91, 95]. These works not only have improved our understanding of superfluids, but also have provided important insights into the design and operation of future devices based on superfluid. As its counterpart in a solid state system, polaritons hold great promise for the study of fundamental superfluid physics as well as application devices. The fact that polaritons become superfluid at normal cryogenic temperatures, and possibly at room temperature, makes the polariton system even more suitable for application purposes. The superfluid physics of polaritons has been extensively studied in a simply-connected geometry [26, 27, 28, 29, 31, 32, 33, 34]. However, there are quite few works on polariton superfluid in a multiply-connected geometry, such as a ring geometry [96, 97, 98]. The ring geometry is of particular interest to us, because it is one of the simplest multiply-connected geometries. In addition, a ring of polaritons is also an important element for polariton circuits which have various possible applications [99, 100, 101, 102].

To create a polariton ring condensate, however, is not a trivial task. One needs to first create a ring trap for the polaritons and then make them relax to the ground state of the trap to form a condensate. In an early effort with short-lifetime polaritons, a non-resonant

excitation laser with ring geometry was used to create the ring condensate [96]. Due to the short lifetime and a gain-loss mechanism, the polaritons were localized to the ring-like pump region. A condensate of ring geometry with multi-lobe density structure was formed when the pump power was increased above a threshold. This patterned condensate was interpreted as a standing-wave state induced by the pump laser. Recently, a similar multi-lobe density patterns was observed in a laser-generated annular potential of a diameter of 40 μm [97]. This pattern is formed by the superposition of two counterrotating polariton waves in high-momentum states, which is similar to a standing wave in a wave guide. These fast moving polaritons interact very weakly with each other due to their large photon fraction. The lifetime of these polaritons is relatively short, about 10 ps. Therefore, the polaritons are unable to thermalize with each other and to relax down to the ground state of the trap to form a condensate.

Our long-lifetime polaritons and the stress trapping method provide unique opportunities for studying the polariton superfluidity in the ring geometry. As shown in Chapter 4, with such a long lifetime, these polaritons are able relax their energy even when they are negatively detuned. In addition, the strength of the interaction between polaritons can be fine tuned by applying stress on the sample. In this chapter, I will show that a highly controllable ring trap for polaritons can be created by placing a laser-generated exciton barrier at the center of a stress-induced harmonic trap. By carefully tuning the photon-exciton detuning in this ring trap, and therefore the polariton-polariton interaction strength, a polariton ring condensate with a coherence length comparable to the condensate size can be created.

The results presented in Section 5.1 and Section 5.3 have been published in "A new type of half-quantum flow in a macroscopic polariton spinor ring condensate," Proceedings of the National Academy of Science of the United States of American, **112**, 2676 (2015) [23].

5.1 CREATING RING TRAP FOR POLARITONS

In our experiments, we created a ring trap in a way similar to that in the cold atom experiments [87, 88], namely, by adding a repulsive barrier at the center of a harmonic trap

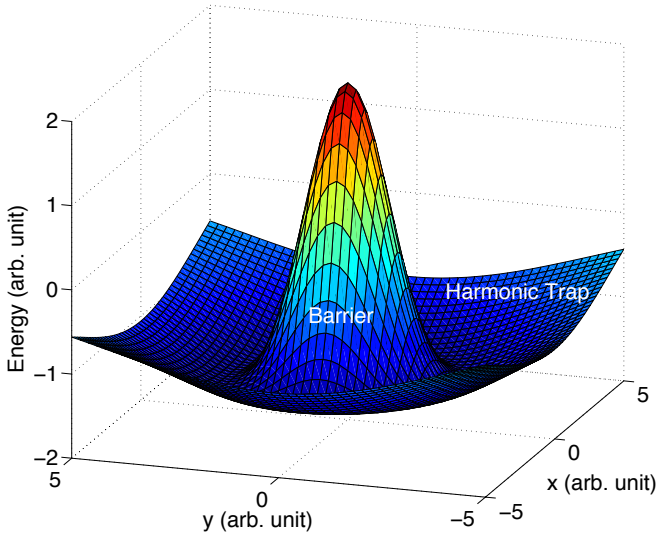

Figure 30: Illustration of a ring trap which is made of a harmonic trap and a barrier at the center.

(see Fig. 30). The harmonic trap is created by the inhomogeneous stress method discussed in Section 3.4, and the repulsive barrier is made of excitons generated by a non-resonant excitation laser discussed in Section 3.5. Because a shift of the exciton energy also affects the photon-exciton detuning and therefore, the strength of the interaction between the polaritons, we must compensate for the effect of the stress on the detuning by our initial choice of the detuning at the location in the cavity. Typically, we choose a region of the sample in which the polaritons are negatively detuned in the absence of stress. Then, by applying stress to the sample, we can bring the excitons into resonance with the photons at this position, or even positively detuned from the photon energy. Thus, the detuning as well as the interaction strength can be fine tuned by controlling the magnitude of the stress. The tuning range of the detuning is only limited by the maximum stress that can be applied on the sample before breaking it. For the 100 μm -thick sample used in our experiments, we limit the stress to be no more than 0.8 N, which shifts the exciton energy by about 9 meV.

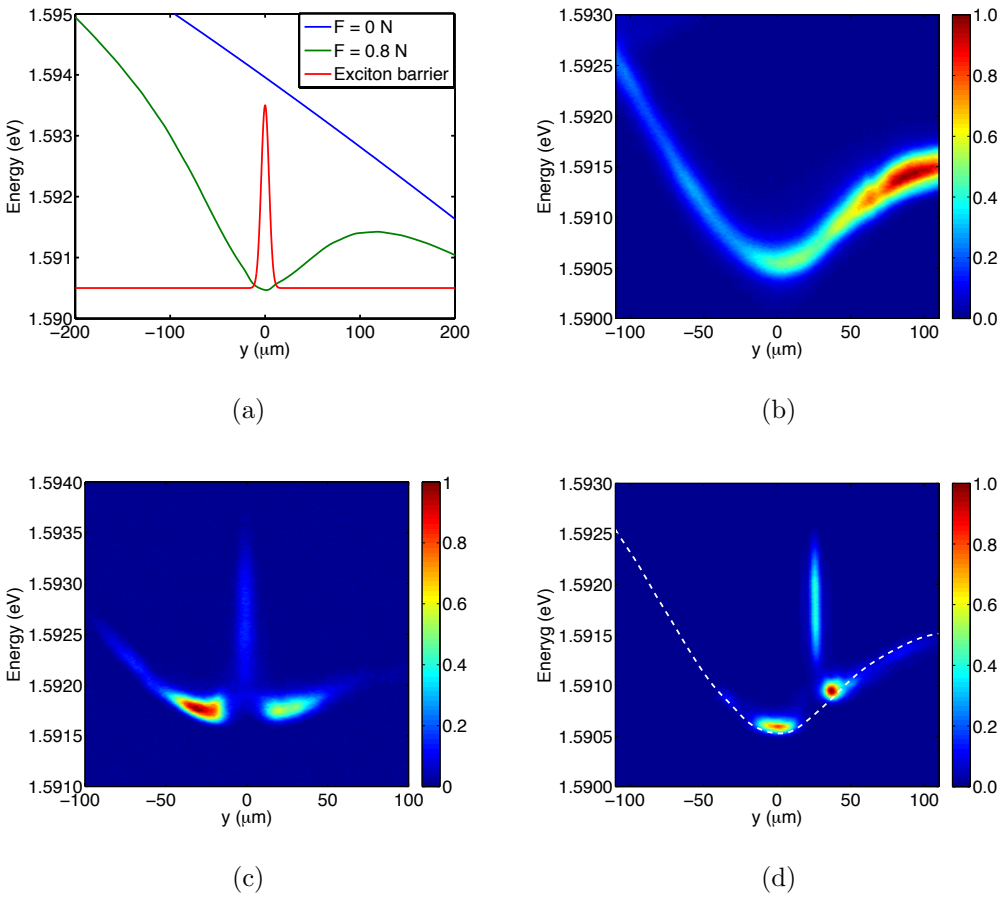

Figure 31: Stress trap and the ring trap (Ref. [23]). (a) The calculated polariton energy without (blue) and with stress applied (green) across the center of the stress trap. The red curve represents the Gaussian barrier created by the non-resonant laser with a FWHM of 10 μm. (b) Energy-resolved PL of the polartions in the vicinity of the stress trap recorded with a defocused laser. The effective trap depth is 1 meV, the quantum level spacing of the trap is $\hbar\omega_0 = 0.02$ meV. (c) A shallower trap with a the laser tightly focused at the center of the stress trap. (d) The same condition with (b) except the laser spot is focused moved to one side of the stress trap. Polaritons flow to both side of the pump spot, including the global minimum.

In the experiments where a coherent polariton ring condensate is obtained (Section 5.3), we chose a region on the sample where the detuning was -6.7 meV without stress and +2.2 meV with a 0.8 N stress applied. Accordingly, the photon fraction of the polariton changes from 0.76 to 0.40. Fig. 31(a) shows the calculated polariton energy in the area of interest without (blue line) and with stress (green line). Fig. 31(b) shows the PL of polaritons in the vicinity of the center of stress trap recorded using a defocused laser. A harmonic trap with a depth of 1 meV and quantum level spacing of $\hbar\omega_0 = 0.02$ meV is created.

We then created a Gaussian barrier inside this harmonic potential using a laser focused to a spot, which generates an exciton cloud. The laser was non-resonant, working at 733 nm corresponding to the second minima above the reflectivity stop band of the DBRs. The laser photon energy 105 meV higher than the polariton energy. This optical pumping produced both excitons and polaritons at the laser focus spot. As mentioned in Section 3.5, the excitons have a mass that is 3-4 orders of magnitude larger than that of the polaritons, and therefore, they diffuse at most about 10 μm from their point of creation; they therefore act as a quasistatic barrier for the polaritons [22, 24, 85]. The sum of the harmonic potential and the Gaussian peak caused by the exciton cloud makes a Mexican hat potential (Fig. 31(a)). Fig. 31(c) shows the intensity of PL of polaritons when the laser spot is focused at the center of the stress trap. The vertical line at the excitation spot is the emission of polaritons shifted to higher energy by the repulsion of excitons. Polaritons that move away from the creation spot are trapped in the region between the central barrier and the stress trap. Fig. 31(d) shows flow of the polaritons in the trap when the laser spot is focused not at the center of the trap but instead, on the right side. The polaritons clearly flow away from the laser spot, about 35 μm, to the minimum of the harmonic potential. The ability of moving large distances while being exciton-like is crucial for the polaritons to establish both spatial and energy equilibrium. As mentioned earlier, in previous works with short-lifetime polaritons [96, 97], spatial and energy equilibrium were not achieved simultaneously because the polaritons were either localized or interacting too weakly with each other.

5.2 EARLY ATTEMPTS TO CREATE POLARITON RING CONDENSATE

Before moving on to talk about the ring condensate created under the conditions described above, I first discuss some of my early attempts to create the ring condensate. It is through these experiments, that I learned how to optimize all the experimental parameters mentioned in the previous section and eventually succeeded in creating a fully coherent ring condensate.

5.2.1 Polaritons in a Deep Ring Trap

My first set of experiments was done at a location where the detuning was -2.5 meV and the exciton fraction of the polariton was 0.41 without stress. I chose this location of the sample because the depth of the trap of a given stress increases as the exciton fraction of the polariton increases; the shift of the polariton energy comes from the shift of the exciton energy. A major advantage of a deep trap over a shallow trap is that it can trap more particles and thus reach a higher particle density in it. At higher density, polaritons will scatter more frequently with each other thus reach better thermalization. In addition, it is easier to reach the critical density for BEC phase transition in a deeper trap as more of the particles created by the excitation laser are collected by the trap.

In order to create the harmonic trap, an 0.8 N stress was applied on the sample. It shifts the detuning to 6.7 meV and the exciton fraction of polariton to 0.73. Fig. 32(a) shows the profile of the stress trap recored with a defocused laser. As seen in this image, the depth of the trap is 1.5 meV .

I then created a barrier in the trap by pumping with a focused laser at a spot (8 μm in diameter) at the center of the stress trap (see Fig. 31(c), for example). To create the ring condensate, the pump intensity was increased above a threshold. In order to reduce heating to the sample, the laser beam was modulated into a quasi-continuos wave with 1% duty cycle at 400 Hz by a mechanical chopper. The pump power mentioned hereafter is the average power.

Fig. 33 shows the 2D real-space images and the energy spectra of polaritons in the ring trap at different pump powers. Fig. 33(a) is the real-space image of polaritons when the

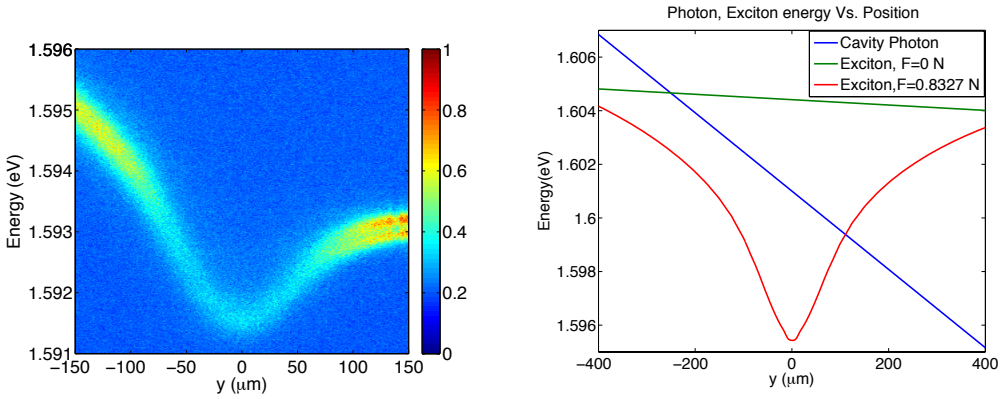

(a) (b)

Figure 32: PL of polaritons near the stress trap and calculated energy of photon and exciton. (a) The stress trap created at the location where the photon-exciton detuning was -2.5 meV without stress and 6.7 meV when a stress of 0.8 N was applied on it. (b) The calculated photon energy (blue), exciton energy without stress (green) and exciton energy after stress applied.

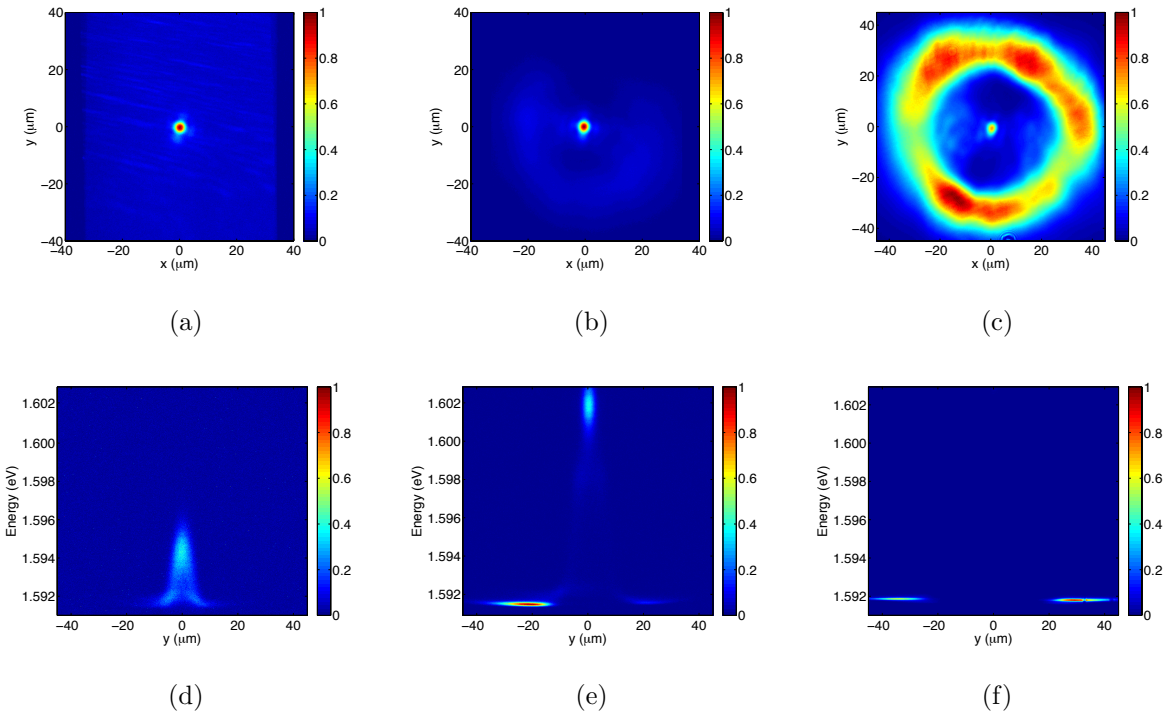

Figure 33: Real-space image and energy of polaritons at different pump powers in the ring trap made of the stress trap in Fig. 32(a) and an exciton barrier at its center. The pump powers are 70 μW for (a) and (d), 1100 μW for (b) and (e), 3000 μW for (c) and (f). (a) – (c) are the real-space images. (d)–(f) are the corresponding energy spectra of the polaritons along $x = 0$. The intensity in each figure is normalized to a maximum intensity of 1.

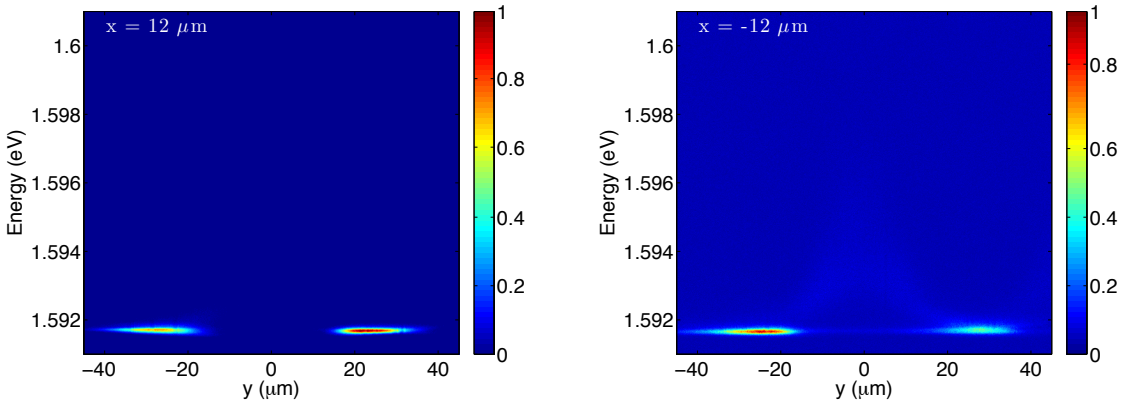

(a)

(b)

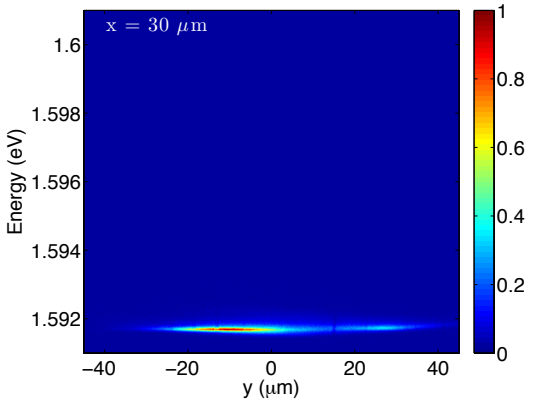

(c)

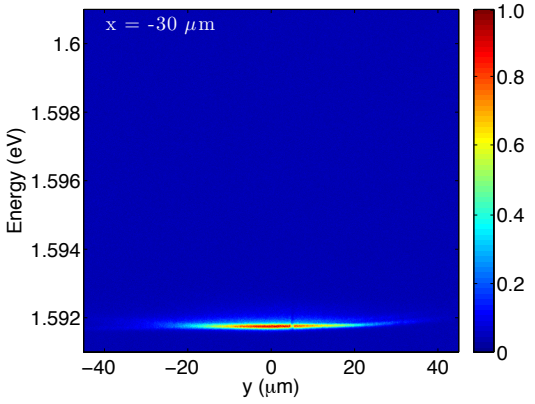

(d)

Figure 34: Energy spectrum of polaritons at different locations on the ring of Fig. 33(c). (a) $x = 12\mu$m, (b) $-x = 12\mu$m, (c) $x = 30\mu$m and (a) $d = -30\mu$m.

pump power is 70 μW. At such low pump power, the PL is dominated by emission from polaritons in the excitation spot. Fig. 33(d) is the energy spectrum of polaritons in the slice $x = 0$ of Fig. 33(a). Inside the excitation spot, polaritons are shifted to higher energies due to the repulsion from excitons. At the center of the excitation spot, where the density of the exciton is highest, polaritons are shifted up by about 3 meV. Outside the excitation region, the exciton population is negligible, thus the energy of polariton is determined by its kinetic energy and the trapping potential.

As the pump power increases, the density of excitons inside the excitation spot also increases, which results in stronger repulsion felt by the polaritons. Under this increasingly strong repulsion, more and more polaritons move away from the exciton spot and accumulate in the ring trap. Fig. 33(b) shows the real-space image of the polaritons when the pump power was 1 mW. In addition to the excitation spot, polaritons also appeared in the ring trap. The polariton population in the ring trap is more visible in the energy-resolved image shown in Fig. 33(e), which was again taken along $x = 0$ μm of Fig. 33(b). The bright PL in the region between $y = -10$ μm and $y = -40$ μm is from polaritons in the ring trap. The spectral line width of the PL is 0.16 meV. At the excitation center, the polariton energy has been shifted up by as much as 10 meV, reaching the cavity photon energy at this position. In fact, at such high density, the system very likely entered into the weak coupling regime [103, 104]. In our case, this only happens near the center of the pump spot where the exciton density is high enough. Outside this region, the system is still in the strong coupling regime.

The density of polaritons in the ring trap keeps increasing as the pump power increases. When the pump power reached 3 mW, a ring-shaped cloud of polaritons was formed in the ring trap. Fig. 33(c) is the real-space image of this ring cloud. In this case, the emission from the ring cloud becomes stronger than the emission from the excitation spot. The energy-resolved image of the slice at $x = 0$ μm (Fig. 33(f)) shows that polaritons in top and bottom parts of the ring are at the same energy state. This state has a very narrow spectral line width which is limited by our spectral resolution of 0.08 meV. Fig. 34 shows the energy spectra of polaritons at several different locations on the ring, which show that they are all at the same energy as that of Fig. 33(f). Thus, the whole polariton ring cloud is in a single energy state.

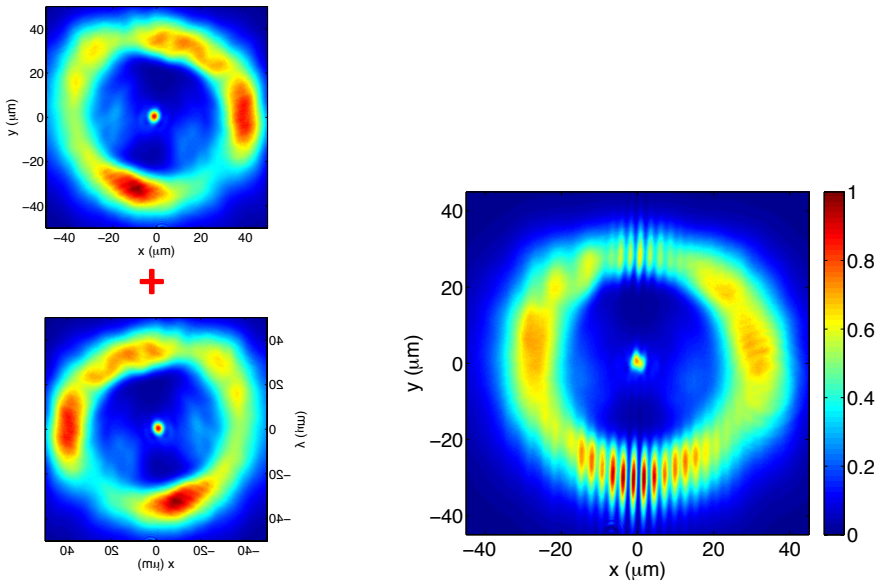

(a) (b)

Figure 35: Illustration of the spatial coherence measurement of the ring cloud and a typical interference pattern. (a) The real-space image of the ring cloud (top) and its flipped image (bottom, $(x, y) \to (-x, y)$) generated by the setup in Fig. 17(a). (b) The interference pattern obtained by overlapping the two images in (a).

The degree of spatial coherence of the ring cloud was measured with the setup discussed in Section 3.3.3.; as illustrated in Fig. 35(a), the ring cloud interferes with an image of itself which is flipped along the $y-$axis, therefore polaritons at position (x, y) will interfere with polaritons at position $(-x, y)$. A typical interference pattern is shown in Fig. 35(b), in which interference fringes parallel to the y axis are seen on the top and bottom parts of the ring. At the bottom part of the ring, interference fringes extend up to 20 μm away from the y axis, which indicates that the phase coherence of the polaritons is maintained up to 40 μm in this part of the ring, and the coherence length is about 20 μm. While on the top part of the ring, the fringes extend only about 5 μm away from the y axis, implying a cohernece length of 5 μm.

It was really surprising that the coherence length in this experiment was, 20 μm at most, only about 10% of the size of ring cloud. One would expect the coherence length to be comparable to the size of the ring, giving the fact that polaritons in the ring cloud are in a single energy state of very narrow spectral line width. However, the interference patterns indicate that the phase coherence of the polaritons could only be maintained over a small fraction of the size of the system. Due to this fact, we could not call this ring cloud a condensate.

In order to create a true condensate in this ring trap, we needed to understand why the coherence length of this polariton ring cloud was so short. Our first speculation was that this short coherence length is a consequence of the fluctuations in intensity of the pump laser we use. It is a well known effect that in non-resonant pumping experiments, the intensity fluctuations of the pump laser can induce phase fluctuations of the polariton condensate and therefore cause dephasing [105]. In this type of experiment, the fluctuations in the pump laser intensity first convert to the fluctuations in the exciton density in the system. Then, when the excitons become polaritons, the fluctuations from the pump laser are converted to fluctuations in the polariton density. Eventually, they lead to fluctuations in the condensate phase, because the condensate energy depends on the polariton density. The coherence time of the system will increase when the density fluctuation of the laser is eliminated. In Ref. [105], when an intensity-stablized single mode laser was used to pump the microcavity, the coherence time of the polariton condensate increased from 10 ps to about 150 ps.

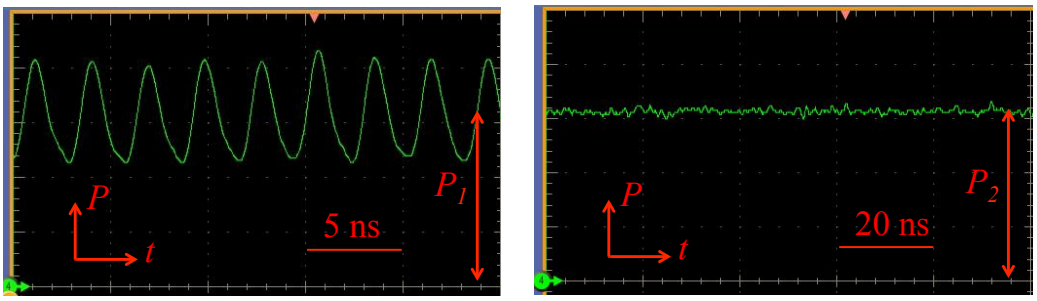

(a) (b)

Figure 36: Screenshots from the an oscilloscope that measures the output power (P) of the laser as a function of time (t). (a) Output power of the laser as a function of time when there is no grating feedback. The output power oscillates at a frequency of 330 MHz with an amplitude of 30% of the average power (P_1). (b) Output power of the laser when there is grating feedback. The power fluctuation is negligible.

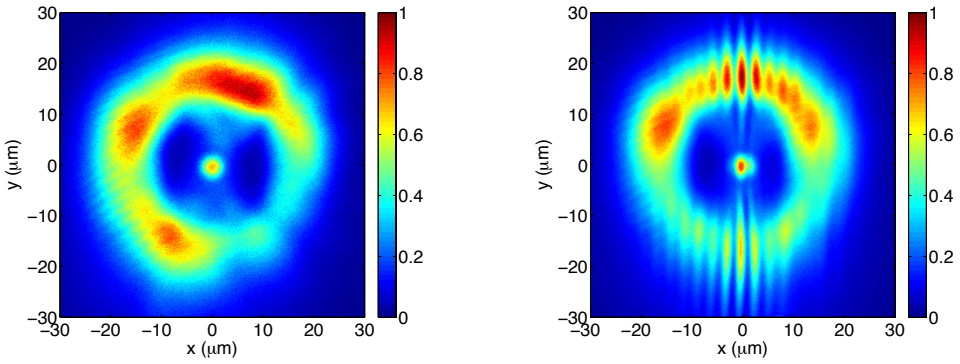

(a) (b)

Figure 37: Real-space images of the polariton ring cloud (a), and its interference pattern (b) created by the home-made Ti:Sapphire laser after grating feedback is installed.

In our experiment, I had taken this effect into consideration when I built our laser: a CW Ti:Sapphire laser. As the intensity fluctuation in this type of laser is typically caused by mode-hopping — hopping between multiple resonant modes of the laser cavity — I minimized the mode-hopping rate by making the cavity as short as possible, which maximized the free spectral range of the laser. The length of the laser cavity is 45 cm, limited by the size of the components inside the cavity, and the corresponding free spectral range is 330 MHz. Fig. 36(a) shows a screenshot of an oscilloscope screen which was measuring the output power of the laser as a function of time. One can see that the output power of the laser is oscillating at a frequency of 330 MHz with an amplitude of 30% of its average power. The oscillation frequency is the same as the free spectral range of the laser cavity, which indicates that this oscillation comes from the beating of the cavity modes. Such a fluctuation is already smaller than many commercialized laser system, but it is still a large fluctuation.

In order to further reduce the intensity fluctuations of this laser, I employed the grating feedback method which is widely used in diode lasers [106]. A 1200 grooves/mm ruled diffraction grating is used to send a fraction of the laser beam back into the cavity. This grating is set into the so-called Littrow configuration with respect to the beam coming from the laser. In this configuration, the incident beam comes in along the normal direction of the grating grooves, the 1st-order diffraction of the grating is collinear and antiparallel to the incident beam. The zero-order diffraction of the grating is the final output of the laser. The spectrally-narrow 1st-order beam will go back into the cavity, stimulate the cavity to lase at the its particular wavelength, and therefore eliminate other modes in the laser cavity. The time evolution of the output power of this laser with the feedback from the grating is shown in Fig. 36(b), from which we see that the laser power is stabilized. One drawback of doing grating feedback is that we lose a lot of output power. There are two reasons for this: One is that without the feedback from the grating, the laser was working at multiple modes which converts the pump power into the laser power more efficiently. After the grating feedback is added, the laser is working in a single mode; thus the total power drops. The other reason is that the grating has a certain efficiency (80% in this case) at its zero-order diffraction. The maximum output power of this laser at 730 nm was about 500 mW without grating feedback, and is 150 mW after adding the grating feedback. This power is just enough to

generate a single-energy polariton ring cloud.

With the laser intensity stabilized, I repeated the experiments. Fig. 37 shows the real-space image of the ring cloud generated with the intensity-stabilized laser, and its self-interference pattern from coherence length measurement. The density of polaritons in the ring is lower than that in Fig. 33(c) because the pump power is lower. But the polaritons are still in a single energy state as indicated by the energy-resolved measurement. It is obvious that the phase coherence still does not extend all the way around the ring. Therefore, we concluded that the fluctuation in the pump laser was not the major reason for the short coherence length.

In our system, the thermal de Broglie wavelength of the plaritons is of the order of 1 μm. Therefore, it is reasonable to expect that the phase coherence is maintained over distances on this order of magnitude. To establish phase coherence over larger distances, polaritons at distant locations needs to synchronize their phase. One way of doing so is to propagate over this distance and synchronize their phase through polariton-polariton scattering. As we will show in Appendix A, near the condensation threshold, such scatterings tend to favor the build-up of phase coherence in the system. But in the meantime, polaritons can also lose their phase coherence by scattering with uncondensed polaritons and phonons in the lattice. Also, when the scattering with other particles is strong, polaritons will not be able to propagate very far. Thus, polaritons from different parts of the system cannot "meet" each other and synchronize their phase. In the case discussed above, the polaritons had a relatively large exciton fraction of 73%, which means they scattered strongly with each other. We noticed that when polaritons are created on the side of the trap, they did not flow down to the center of the trap which indicates that the mobility of these polaritons is low. Therefore, we suspected that the coherence length is short because the exciton fraction of the polaritons was too high.

5.2.2 Polaritons in a Shallow Ring Trap

Based on the discussion above, we decided to create a ring trap in which the polaritons will have smaller exciton fraction and can flow better. We moved to a region of the sample where

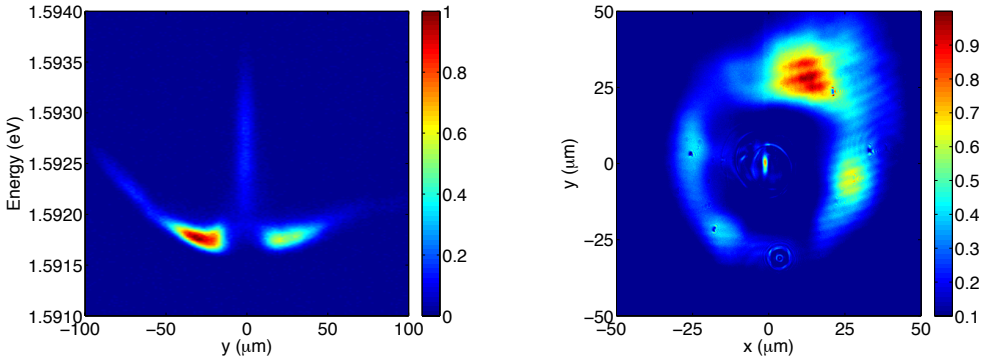

(a) (b)

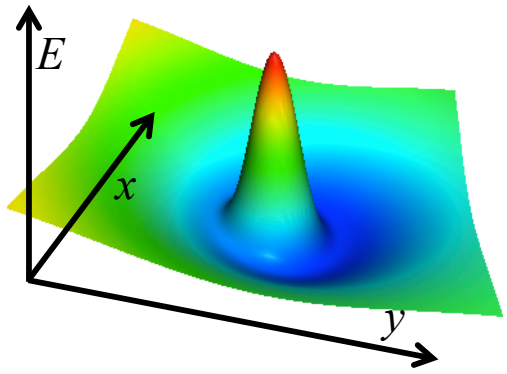

(c)

Figure 38: (a) Energy-resolved image of polaritons in the stress trap created at the new location on the sample, where the detuning is -6.6 meV without stress and -0.5 meV with a 0.6 N stress applied on it. (b) Real-space image of polariton cloud in the ring trap. (c) Schematic of the trap profile in which the multi-lobe density pattern is osberved. The cavity gradient is along the y direction.

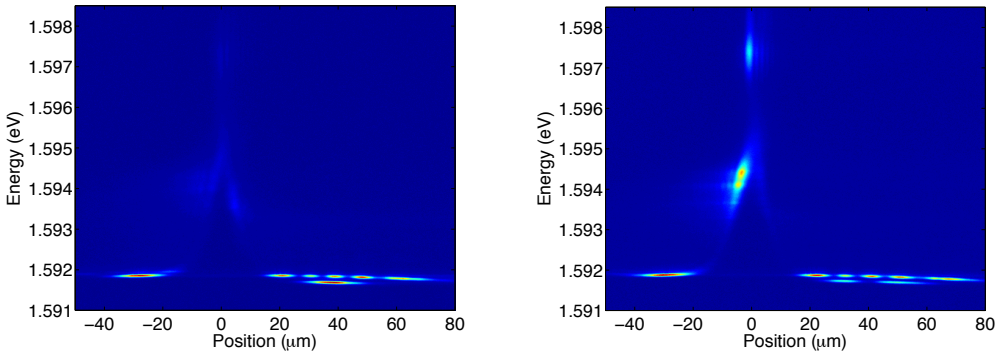

(a)

(b)

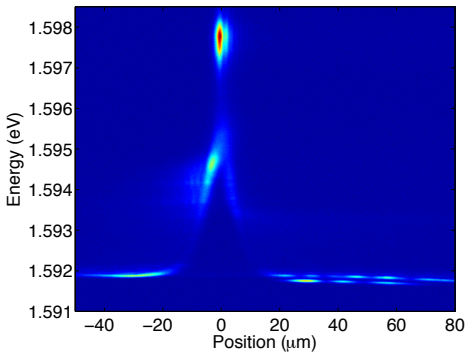

(c)

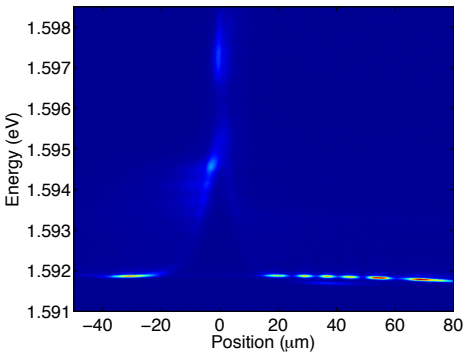

(d)

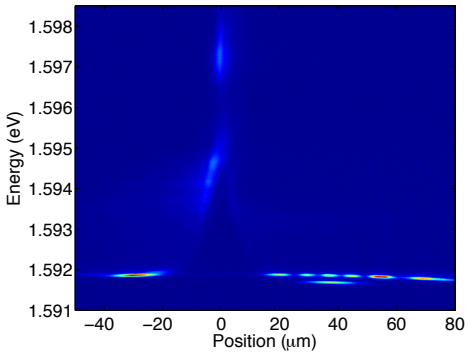

(e)

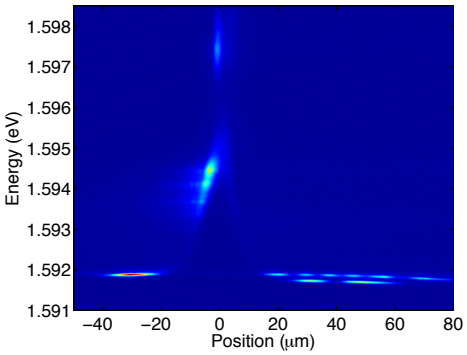

(f)

Figure 39: Energy-resolved images of the polaritons in the trap when the laser spot is about 20 μm away from the center of the stress trap.

the detuning was -6.6 meV without stress, and the exciton fraction of the polaritons was 0.28. We also decreased the magnitude of the stress to 0.6 N. When this stress was applied on the sample, the detuning changed to -0.5 meV and the exciton fraction increased to 0.48. We did not use smaller exciton fractions, because polaritons might not be able to thermalize with each other when the exciton fraction is too small.

Fig. 38(a) shows the profile of the stress trap created at this new location, which has a depth of 0.45 meV. Fig. 38(b) shows the real-space image of polaritons in the ring trap when the pump power is 3 mW. This ring-shaped polariton cloud does not have a uniform density profile as that in Fig. 33(c). It is interesting to notice that there are fringes in the top and right side of the cloud. As this is not a interference image, these fringes correspond to modulations in the density of polaritons in this region. In order to get a more uniform density profile, we moved the laser spot around near the center of the stress trap. However, we did not get any better ring-shaped cloud.

While moving the laser spot around, we noticed that when the laser spot was moved downward, more polaritons accumulated into the top and right parts of ring, and the fringes became more visible. We spectrally resolved this polariton cloud along $y = 0$ μm when the laser spot is about 20 μm below the center of the trap. Fig. 39 shows the typical results of this measurement. As the polariton distribution was fluctuating, we took many images in a row and analyzed them afterwards. Images shown here are taken with a time separation less than 1 second between each other. These images have two striking features: polaritons in the region of $y > 0$ (top part of ring) have a multi-lobe density profile, and they occupy multiple discrete energy levels. These two features can be understood simultaneously by interpreting these energy states as the eigenstates of the harmonic trap formed by the exciton barrier and the stress trap in the radial direction. For example, in Fig. 39(a) the polaritons are occupying the ground state (one lobe in density) and the 4th excited state (5 lobes in density) of the harmonic trap. In Fig. 39(b) they are occupying the 1st excited state and the 5th excited states of the harmonic trap. From the energy spacing between the ground state and the excited states, one can determine the quantum level spacing of this harmonic trap, which turns out to be 0.03 meV. On the other hand, the quantum level spacing of the trap formed by the exciton barrier and the lower side of the stress trap is about 0.028 meV, which is

estimated from the fact that the energy of polaritons changed from 1.5919 eV to 1.5917 eV when going from $x = 20$ μm to $x = 38$ μm in Fig. 39(a).

Similar behaviors of polaritons have been observed in other experiments, for example, in Ref. [20] it was observed that polaritons occupy the first few excited states of 1D harmonic trap formed in between two exciton barriers. The fact that polaritons remain in the excited states of the harmonic trap is an indication of the lack of interaction between them, which is due to the small exciton fraction they have. Therefore, a larger exciton fraction is needed for them to relax to the ground state.

Polaritons on the other side of the exciton barrier ($y > 0$) exhibit different behavior: they are all condensed into the ground state of the ring trap in this region. This behavior can be understood as a consequence of better confinement in this region, which can be seen from Fig. 38(a): the stress trap on this side is deeper than on the other side. Therefore, more polaritons can be trapped in this region which led to higher density and better thermalization of polaritons. In contrast, the boundary of the stress trap on the other side is low, most polaritons escape the trap from this side. Therefore, the density of polaritons is low on this side, and they can not efficiently thermalize with each other. It is worthwhile to point out that we only observed this multi-lobe density profile in the radial direction of the stress trap. This is because the confinement in the radial direction is much stronger than the tangential direction.

5.3 OBSERVATION OF A POLARITON RING CONDENSATE

The experiments discussed in the last section showed us that a balance between the mobility and the interaction strength of polaritons is required for creating a fully coherent ring condensate. Following this principle, we eventually succeeded in creating a polariton ring condensate by using the combination of parameters mentioned in Section 5.1. In this section, I will discuss the successful experiments.

In these experiments, the stress trap was created at the same location as that of Section 5.2.2. In order to increase the strength of interaction between polaritons, the stress was

increased to 0.8 N. This changed the detuning from -6.7 meV without stress to +2.2 meV with the stress applied. The exciton fraction of the polariton also changed, from 0.34 to 0.60. A trap with a depth of 1 meV was created, and its profile is shown in Fig. 31(b). Polaritons in this trap had a much better mobility than the polaritons in the trap of Fig. 32(a). This is proved by Fig. 31(d), in which polaritons, created on the side of the trap, flow over 35 μm to the bottom of the trap. The ring trap is created by pumping at the center of the stress trap with a non-resonant laser. More details about the trap can be found in Section 5.1.

To create a polariton condensate in this ring trap, we kept the focused laser spot at the center of the stress trap and increased the pump power to above a critical threshold. Fig. 40(a) shows the real-space image of polaritons when the pump power is 64 μW, far below the critical threshold value 1100 μW. At such low pump power, the PL is dominated by emission from polaritons in the excitation spot. Fig. 40(b) is the energy spectrum of the slice at $x = 0$ in Fig. 40(a). Inside the excitation spot, polaritons are shifted to higher energies due to the repulsion from excitons. At the center of the excitation spot, where the density of the exciton is highest, polaritons are shifted up by 4.5 meV. Outside the excitation region, the exciton population is negligible therefore polaritons are at the energy determined by their kinetic energy and the trapping potential.

As the pump power increases, the energy blue-shift of polaritons at the excitation spot increases. More and more polaritons move out of the pump region due to the increasingly stronger repulsion from excitons. As a result, the density of the trapped polaritons also increases. When the pump power is above a critical threshold, a ring shaped polariton cloud appears in the trap. Fig. 40(c) shows the PL of polaritons when the pump power is 3560 μW, well above the critical threshold. The PL is dominated by emission from polaritons on a ring of an average radius of 25 μm. Fig. 40(d) shows the energy spectrum of polaritons on the slice at $x = 0$ in Fig. 40(c). It shows that polaritons from the upper and lower part of the ring are in the same single energy state. The spectral line width of this state is 0.1 meV, limited by the resolution of our spectrometer which is 0.08 meV. Energy spectra of the polaritons at several different locations on the ring are shown in Fig. 41. They show that the polaritons in the ring cloud are all in the same single energy state.

The degree of spatial coherence of this ring cloud is measured by interfering it with a

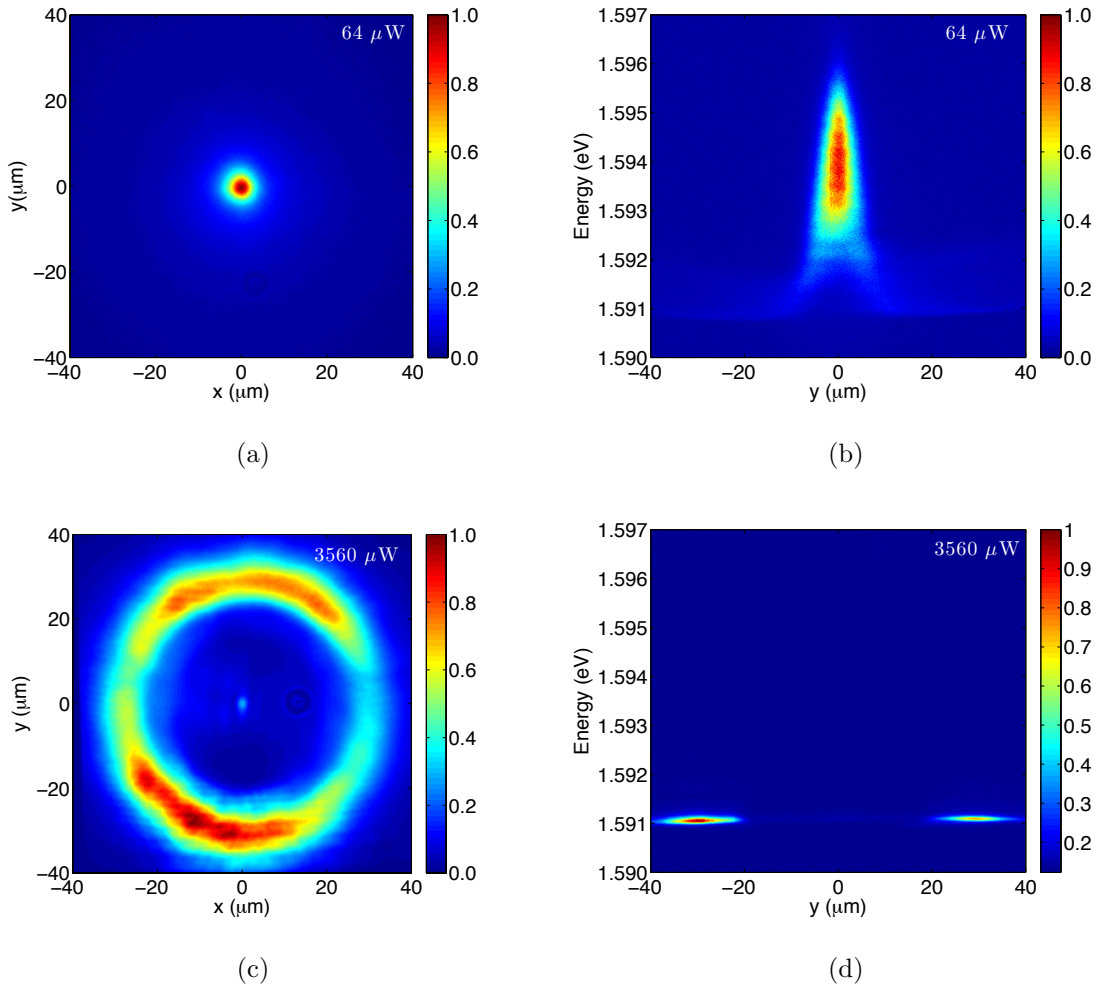

Figure 40: Real-space images and spectra of polaritons in the ring trap below and above the condensation threshold. (a) Real-space image of the polaritons when the pump power (64 μW) is below the condensation threshold (1000 μW). (b) Spectra of the poloaritons at $x = 0$ of (a). (c) Real-space image of the polaritons when the pump power (3560 μW) is above the condensation threshold. (d) Spectra of the poloaritons at $x = 0$ of (b). From Ref. [23]

.

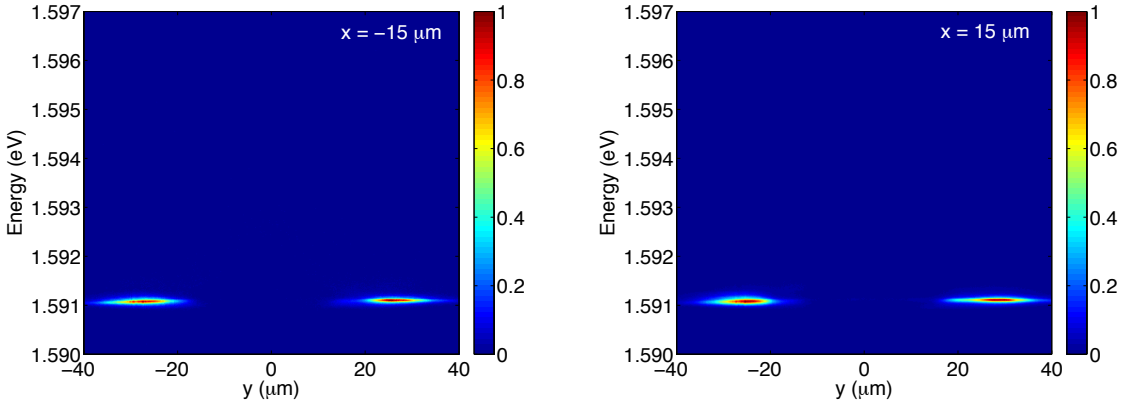

(a) (b)

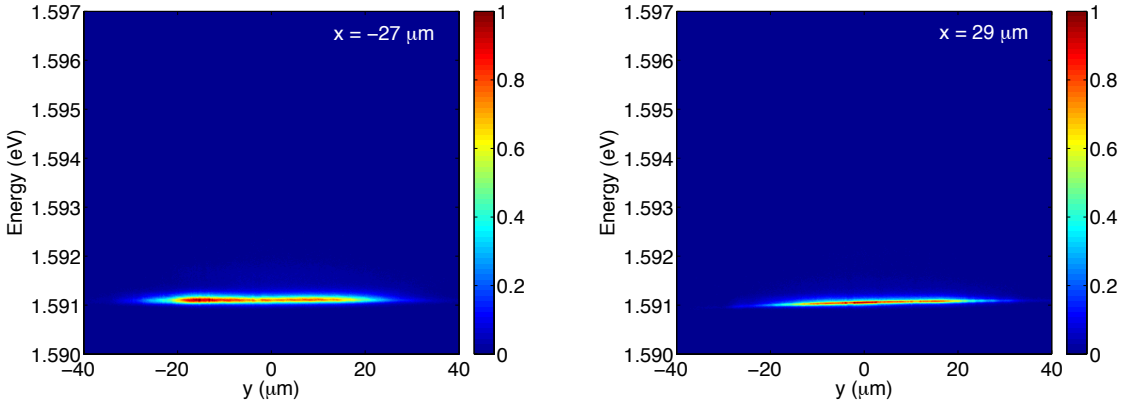

(c) (d)

Figure 41: Spectra of polaritons at different parts of the ring condensate. (a) $x = -15$ μm, (b) $x = 15$ μm, (c) $x = -27$ μm, (a) $x = 29$ μm

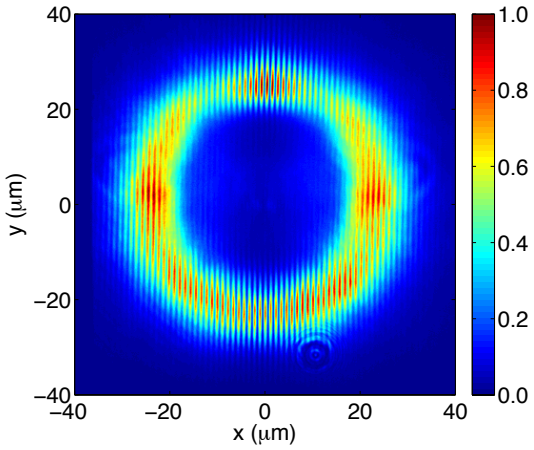

Figure 42: Interference pattern of the ring condensate with its flipped image ($x \to -x$). From Ref. [23].

image of itself which is flipped $x \to -x$ as discussed in Section 3.3.3 (An illustration of this method is shown in Fig. 35(a)). Fig. 42 shows a typical interference pattern of the ring cloud, in which fringes are seen all over the ring, implying that the coherence extends across the whole ring. This is in sharp contrast to the interference pattern of the polariton ring cloud in a deeper trap discussed in the Section 5.2.1. It is clear that in the current case the coherence length is at least the same as the system size. Based on this, we can conclude that the ring-shaped polariton cloud is indeed a condensate.

6.0 HALF-QUANTUM CIRCULATION OF POLARITON RING CONDENSATE

In the last chapter, I discussed the experiment in which a fully coherent polariton ring condensate was created. In this chapter, I will focus on the study of the properties of this polariton ring condensate. Through phase and polarization-resolved measurements, I found that this ring condensate was in a new type of half-quantized circulation state. The existence of this state is related to the spinor nature of polaritons as well as the ring geometry of our system. Because it is a spinor condensate, half-quanta are allowed in which there is a phase rotation of π together with a polarization vector rotation of π around a closed path in the condensate. In our ring geometry, the half-quantum state that we see is one in which the handedness of the spin flips from one side of the ring to the other side in addition to the rotation of the linear polarization component; such a state is allowed in a ring geometry but will not occur in a simply connected geometry. This state is lower in energy than a half-quantum state with no change of the spin direction and corresponds to a superposition of two different elementary half-quantum states. The fact that the observed state is not the energy ground state of the system is very likely related to the dynamics of the quasi-steady state condition of generating the ring. This type of macroscopic polariton ring condensate allows for the possibility of direct control of the circulation to excite higher quantized states and the creation of Josephson junction tunneling barriers.

The results presented in this chapter have been published in "A new type of half-quantum flow in a macroscopic polariton spinor ring condensate," Proceedings of the National Academy of Science of the United States of American, **112**, 2676 (2015) [23].

6.1 CIRCULATION IN THE RING CONDENSATE

By analyzing the interference pattern, we find that the number of fringes on the top of the interference patterns in Fig. 42 are not always equal to the number of fringes on the bottom. In fact, about 90% of the time there is one more fringe either in the top or in the bottom part of the interference pattern. And for the rest 10% time, there are equal number of fringes in the top and the bottom parts of the interference pattern. Fig. 43 show typical interference patterns for these situations. As discussed in Section 2.5, the difference in the number of fringes corresponds to a net phase shift around the ring. This implies that the phase of the condensate cannot be continuous – in the ring geometry, the potential barrier at the center of the ring makes the density of the condensate zero where the discontinuity occurs.

To see this phase shift more clearly, we retrieved the phase of the interference pattern with the numerical method known as digital off-axis holography [107]. A pedagogic introduction to this method can be found in Ref. [108]. The procedure of processing the interference pattern to get the phase map can be found in Appendix C. Fig. 43(d) – (e) shows the phase maps corresponding to the interference patterns. In the phase maps, the phase of the condensate changes 2π when going around the ring. Because the interference pattern measures the phase shift of the ring condensate relative to itself in the opposite direction, the net phase shift around the ring is one-half of that shown in the phase map. Therefore, there is a $\pm\pi$ phase shift around the ring condensate, which corresponds to a net circulation of polaritons with angular momentum of $\pm\hbar/2$. This half-quantum circulation indicates that the spinor nature of the polaritons is important, because a scalar condensate must have a phase change of $2n\pi$ (n is an integer) around a closed path.

6.2 POLARIZATION ROTATION OF THE RING CONDENSATE

To ensure that the wave function is single-valued, there must be another π rotation of the linear polarization of the polariton in connection with the π phase shift around the same path. Polaritons possess a spin with two possible projections in the growth direction

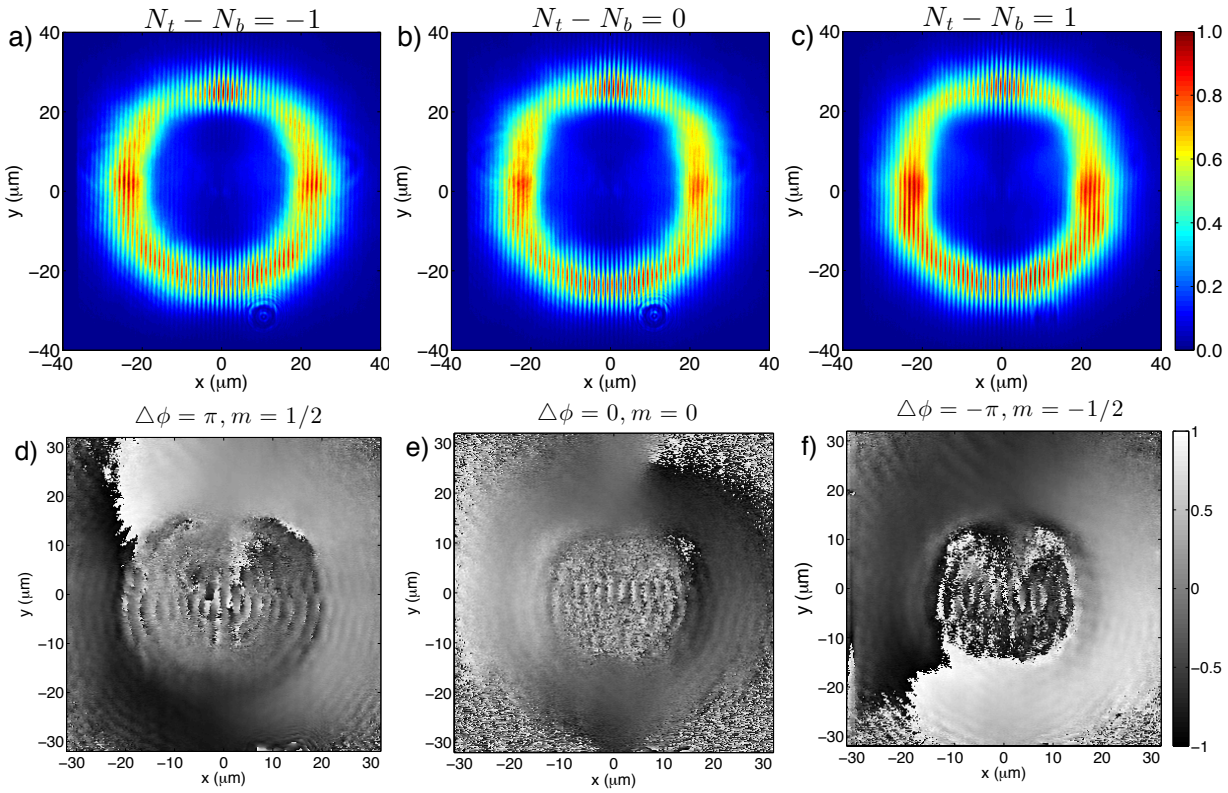

Figure 43: Interference patterns of the ring condensate. (a) There is one more fringe in the bottom half of the ring ($N_t - N_b = -1$). (b) They are equal amount of fringes in the top and bottom half of the ring ($N_t - N_b = 0$). (c) There is one less fringe in the bottom half of the ring ($N_t - N_b = 1$). (d), (e) and (f) are the phase maps obtained by processing the interference patterns in (a), (b), and (c) respectively. From Ref. [23].

of the microcavity structure. They directly map to the two possible circular polarization states of the emitted photon. When the spin of the polariton has a component in the cavity plane, the emitted photon becomes elliptically polarized; the in-plane spin component gives a nonzero linear polarization, and the spin component on the growth axis gives nonzero circular polarization. Thus, the spin state of the polariton can be deduced from the polarization of the emitted photons. We determined the polarization of the emitted photons by measuring its Stokes vector. The Stokes vector $\vec{S} = (S_0, S_1, S_2, S_3)$ is related to polarization of a photon by,

$$
\begin{aligned}
S_0 &= I, && (6.1)\\
S_1 &= \frac{I_{0^\circ} - I_{90^\circ}}{I_{0^\circ} + I_{90^\circ}}, && (6.2)\\
S_2 &= \frac{I_{45^\circ} - I_{-45^\circ}}{I_{45^\circ} + I_{-45^\circ}}, && (6.3)\\
S_3 &= \frac{I_{\sigma^+} - I_{\sigma^-}}{I_{\sigma^+} + I_{\sigma^-}} && (6.4)
\end{aligned}
$$

where I is the intensity of light, I_{0° and I_{90°, I_{45° and I_{-45° are the intensities of the linear polarization components of the light along the vertical (0°) and horizontal (90°), diagonal (45°) and antidiagonal (-45°) directions, respectively. I_{σ^+} and I_{σ^-} are the intensity of the right-handed and left-handed circular polarization components of the photon. With the Stokes vector, the polarization of the photon can be fully determined as

$$
\begin{aligned}
DOP &= \sqrt{S_1^2 + S_2^2 + S_3^2} && (6.5)\\
DOLP &= \sqrt{S_1^2 + S_2^2}\ , && (6.6)\\
\theta &= \frac{1}{2}\arctan(\frac{S_2}{S_1})\ , && (6.7)\\
DOCP &= S_3\ , && (6.8)
\end{aligned}
$$

where DOP is the total degree of polarization of the photon, DOLP is the degree of linear polarization, θ is the polarization angle with respect to the vertical direction (0°), and DOCP is the degree of circular polarization.

The intensities of the linear polarization components are measured by passing the photoluminescence of polaritons through a linear polarizer. To measure the intensity of the

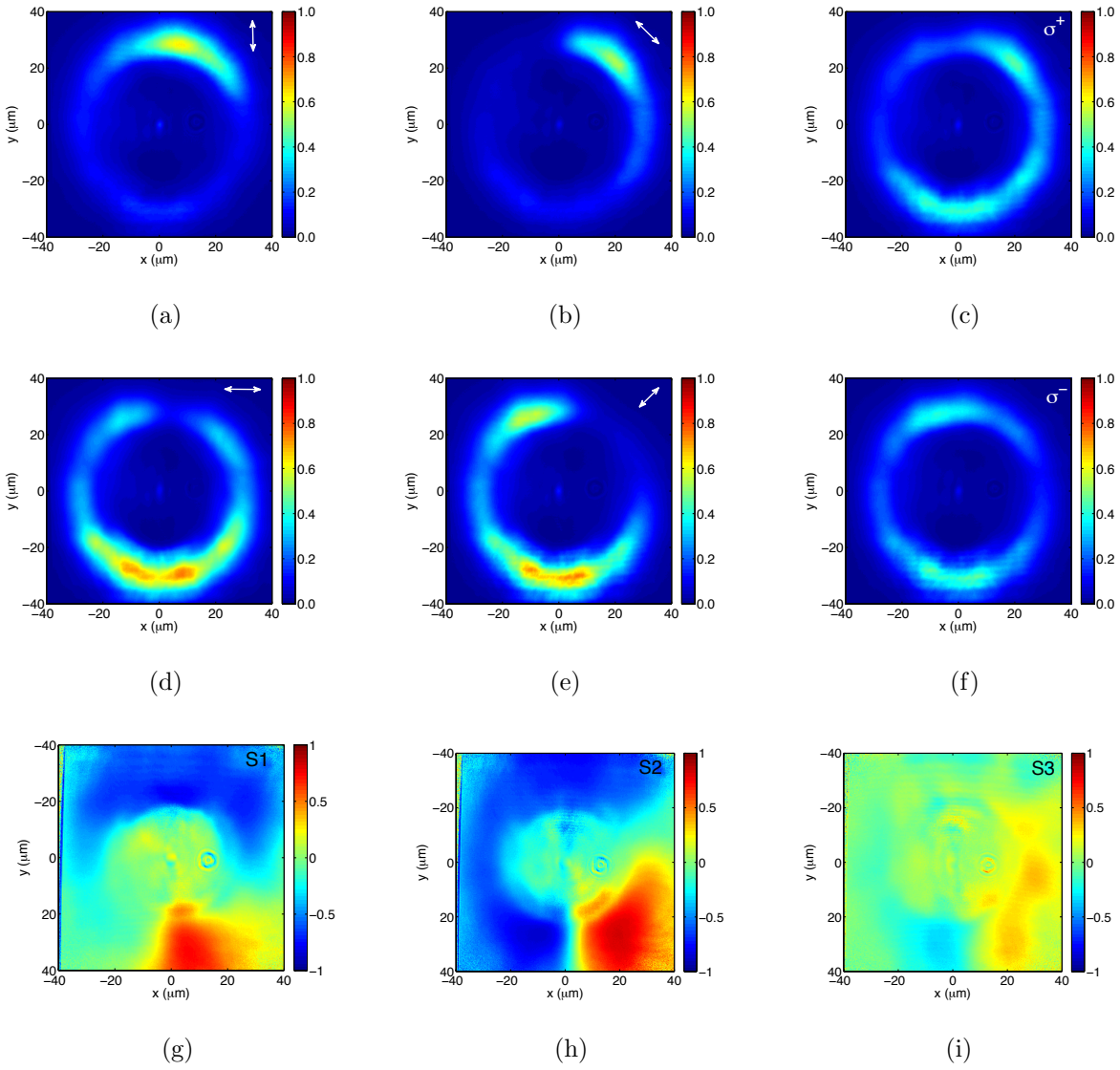

Figure 44: Polarization resolved real-space image of the ring condensate and the measured Stokes parameters. (a)–(d) The linear polarization component of the ring condensate. The white double arrows represent the direction of the linear polarization. (e)–(f) The circular polarization component of the ring condensate. (g)–(i) The Stokes parameters $S1$, $S2$ and $S3$ calculated from (a) and (d), (b) and (e), and (c) and (f) by using Eq. (6.1) – (6.4). (a)–(f) are from Ref. [23].

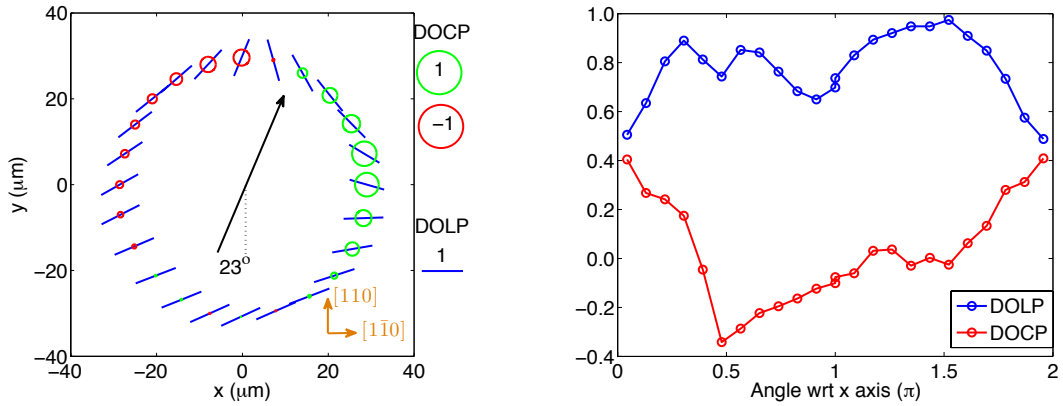

(a) (b)

Figure 45: Polarization of the ring condensate obtained from the Stokes vector measurement. (a) The polarization of polaritons in the ring condensate. The blue lines represent the degree of linear polarization (DOLP) with its length being proportional to the magnitude of the linear polarization and its oriental being the direction of the linear polarization. The circles represent the degree of circular polarization (DOCP). The red circles correspond to left-handed circular polarization, and the green circles correspond to right-hand circular polarization. The diameter of the circle is proportional to the degree of circular polarization. (b) The degree of linear polarization (DOLP, blue dotted line) and the degree of circular polarization (DOCP, red dotted line) of the polaritons as a function of the polar angle (angle with respect to the positive x direction). From Ref. [23].

circular polarization component, the PL is first sent through a $\lambda/4$ wave plate, which converts the circularly polarized light into linearly polarized light. Depending on the handedness of the circular polarization, the emergent linear polarization is either along the 45° direction or $-45°$ with respect to the fast axis of the wave plate. The PL is then passed through a linear polarizer of which the transmission axis is at 45° with respect to the fast axis of the wave plate. Fig. 44 shows the real-space image of the ring condensate with the polarization resolved. It can be seen from these images that different parts of the ring condensate have different polarizations.

Using these images as input for Eq. (6.1) and Eq. (6.5), we obtain the polarization map of the ring condensate. Fig. 45(a) shows the polarization at different spots on the ring. The blue line represents the linear polarization: its length is proportional to the DOLP, and its orientation is the direction of the polarization. The Circle represents the circular polarization, its diameter is proportional to the DOCP and its color represents the handedness of the circular polarization: red for σ^- and green for σ^+. It can be seen from Fig. 45(a) that the linear polarization vector rotates by 180 degrees when going around the ring. This allows the boundary condition of the ring condensate, discussed above, to be satisfied. More interestingly, the circular polarization component flips handedness on opposite side of the ring. The boundary between the opposite circular polarization components is lined up with the cavity gradient direction (black arrow). This polarization pattern is striking given that the underlying exciton states in GaAs-based structures have a fourfold symmetry, which is seen in a fourfold rotational symmetry of the polarization pattern under incoherent conditions [81, 82], and the eigenstates of the polariton states are linearly polarized [81]. The orientation of the pattern is not connected to the underlying crystal symmetry; instead, it is fixed relative to the gradient of potential that exists in the system, which comes from the wedge in the cavity width. As we will discuss in Chapter 7, the polarization pattern of the condensate also does not depend on the polarization of the laser that generates the polaritons at the central spot.

6.3 HALF-QUANTIZED CIRCULATION STATE OF THE RING CONDENSATE

The interference pattern and the polarization measurements can both be understood as the effects of quantized angular momentum in a spinor condensate. The generic effect of half-quantization has been worked out for spinor atom condensates [109], d-wave superconductors [110] and in particular, by Rubo [111], the case of polaritons in a simply connected geometry; half-quantized vortices were reported experimentally for a polariton condensate localized in a submicrometer disorder minimum [29, 35]. However, the state that we see here is distinct from the half-vortex state by Rubo [111] and is allowed only in a ring geometry.

The Rubo state, when generalized to a ring geometry, consists of a π-rotation in phase around a closed path accompanied by a π-rotation of the polarization angle around the same path. In terms of the linear polarization components in the plane of the sample, the azimuthal angle dependence of the Rubo state around a circle of constant radius can be written as [111]

$$\vec{\varphi}_{k,m}(\theta) = \sqrt{n(\theta)}e^{im\theta}\left[f\begin{pmatrix}\cos(k\theta)\\ \sin(k\theta)\end{pmatrix} -i\,\mathrm{sgn}(km)\sqrt{1-f^2}\begin{pmatrix}\sin(k\theta)\\ -\cos(k\theta)\end{pmatrix}\right]. \tag{6.9}$$

Here, $m, k \in \{-1/2, +1/2\}$ select the rotation directions for the phase and polarization, respectively; $n(\theta)$ is the effective one-dimensional density of the condensate, and f is a real constant which gives the degree of circular polarization, and $|f|$ must be less than 1. In the Rubo vortex state, f can depend on the radius r, while in a ring, we can approximate that f is nearly constant. For each combination of k and m, this ansatz gives a degree of circular polarization $c = \mathrm{sgn}(km)2f\sqrt{1-f^2}$ which does not depend on θ, and a linear polarization angle that rotates as $k\theta$. In the absence of interactions, and in a homogeneous ring $n(\theta) = n$, these states with $|f| = 1/\sqrt{2}$ are eigenstates of the Hamiltonian that consists of the kinetic energy,

$$H_{\mathrm{kin}} = -\frac{\hbar^2}{2m}\nabla^2 \equiv -\frac{\hbar^2}{2mR^2}\frac{d^2}{d\theta^2}, \tag{6.10}$$

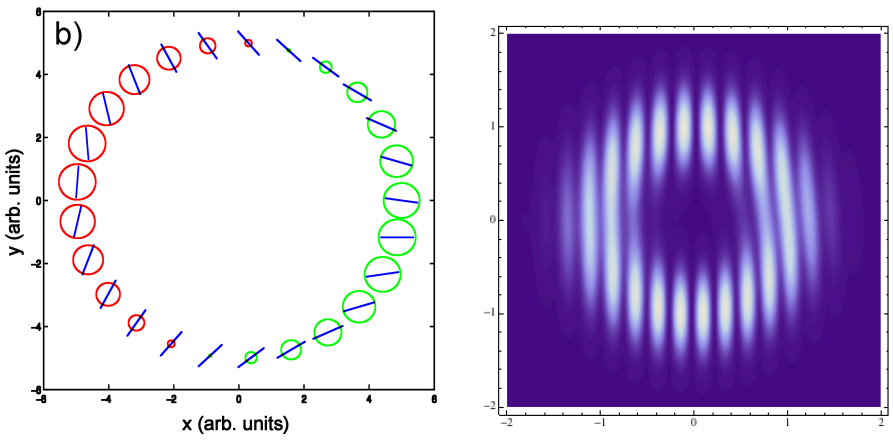

(a) (b)

Figure 46: (a) Polarization map, and (b) interference pattern of the ring condensate given by Eq. (6.13).From Ref. [23].

where m is the effective mass of the polaritons.

In a simply connected geometry, only half quanta of the type Eq. (6.9) are allowed, because there is an implicit boundary condition that the polarization must be continuous at $r = 0$. However, in a ring geometry, this condition is relaxed, and other wave functions with half-quanta of circulation also satisfy the boundary condition that the wave function be single-valued. The polarization pattern we observe was reproduced by A. Daley using the following form for the wave function, which is the same except for a single sign change:

$$\vec{\psi}_{k,m}(\theta) = \sqrt{n(\theta)}e^{im\theta}\left[f\begin{pmatrix}\cos(k\theta)\\ \sin(k\theta)\end{pmatrix} + i\,\mathrm{sgn}(km)\sqrt{1-f^2}\begin{pmatrix}\sin(k\theta)\\ \cos(k\theta)\end{pmatrix}\right]. \tag{6.11}$$

This equation gives the polarization map shown in Fig. 46(a) for the choice of $f = -0.3$. Like the Rubo state, it provides a half-quantum of circulation with a phase rotation direction chosen by the sign of m, but it involves a flip of the circular polarization around the ring. For these states, the degree of circular polarization is given by $c = -\,\mathrm{sgn}(km)2f\sqrt{1-f^2}\cos(2k\theta)$,

so that the circular polarization direction, i.e., the z-component of the spin-1 particles, flips from one side of the ring to the other, as seen in the experimental data of Fig. 45(a). The linear polarization angle is given by

$$\frac{1}{2}\arg\left(\frac{f+\mathrm{sgn}(km)\sqrt{1-f^2}\,e^{2ik\theta}}{f\,e^{2ik\theta}-\mathrm{sgn}(km)\sqrt{1-f^2}}\right), \tag{6.12}$$

which can rotate in either direction, and this direction is determined by the sign of k in the ansatz. Note that any sign of k and m can be paired here. As shown in Fig. 46(b), this ansatz also reproduces the interference patterns which we observe. It reproduces the observation of a difference of one between the top and bottom of the pattern; a full quantum of vorticity would give a difference of two fringes between the top or the bottom. There are fewer fringes across the ring because a smaller angle between the two interfering beams is chosen in the simulation.

The state seen here is not an eigenstate of kinetic energy. The ansatz (Eq. (6.11)) that fits our experimental data corresponds to the superposition

$$\vec{\varphi}_{k,m} = -\sqrt{2}(0.95\vec{\psi}_{\frac{1}{2},\frac{1}{2}} + 0.3\vec{\psi}_{\frac{1}{2},-\frac{1}{2}}), \tag{6.13}$$

where $\vec{\psi}_{k,m}$ indicates the Rubo states (Eq. (6.9)) with $f = 0$, which are chosen because they give us an orthogonal basis of states with well- defined physical properties. In other words, the observed state is a superposition of different half-quantized circulating states. Although a superposition of different angular-momentum states may seem odd, there is no in-principle reason for the system to favor a pure angular momentum state over the observed spin-flipping circulating state. Both states satisfy the boundary conditions. The state given by Eq. 3 is not allowed in a simply connected geometry, however, because the kinetic energy would diverge at r = 0. The fact that the observed state is not an energy eigenstate is likely related the dynamic quasisteady-state conditions of generating the ring. I will discuss this in more detail in Chapter 7.

6.4 MOMENTUM-SPACE IMAGES OF THE RING CONDENSATE

So far, I have discussed the interesting properties of the ring condensate discovered by analyzing its real-space images. The momentum-space image of the polaritons, on the other hand, also carries abundant information about the system. In this section, I will present the momentum-space measurements of the ring condensate at different pump intensity, and discuss the implications of their results.

The momentum-space images are taken with the setup shown in Fig. 14(b). Fig. 47 shows the momentum-space images of polaritons in the ring trap at different pump powers. Fig. 47(a) shows the momentum distribution of the polaritons when the pump power is 10 μW. The momentum distribution seen in this image is highly anisotropic: a large fraction of the polaritons are moving in the direction opposite to the cavity gradient direction (white arrow). This is in sharp contrast to Fig. 15(a) which is the typical momentum-space distribution of polaritons at low density without trapping. Here, I propose an interpretation which takes into account the effects of cavity gradient and time-averaging in the data collecting process. Further experiments and numerical modeling are needed to fully understand the features of these momentum-space images.

Due to the cavity gradient, the stress trap is in fact tilted (see Fig. 48(a)) with the uphill side being at higher energy than the downhill side. After being created at the center of the stress trap, polaritons rapidly move out of the excitation region due to the strong repulsion from excitons in this region. As they move out of the excitation region, their potential energy converts to kinetic energy in the cavity plane. The initial momentum distribution of polaritons when they leave the excitation region is isotropic as shown in Fig. 48(b), where only the PL from the excitation region is collected. After leaving the excitation region, polaritons will propagate in the cavity plane under the influence of the stress trap and the cavity gradient. Polaritons moving toward the uphill side will always feel a force which is the sum of the restoring force from the stress trap and the constant force from the cavity gradient. Polaritons keep moving away from the center of the trap until all their kinetic energy is converted to potential energy. Then they will start moving in the opposite direction—toward the center of the trap. In this process they are accelerating until

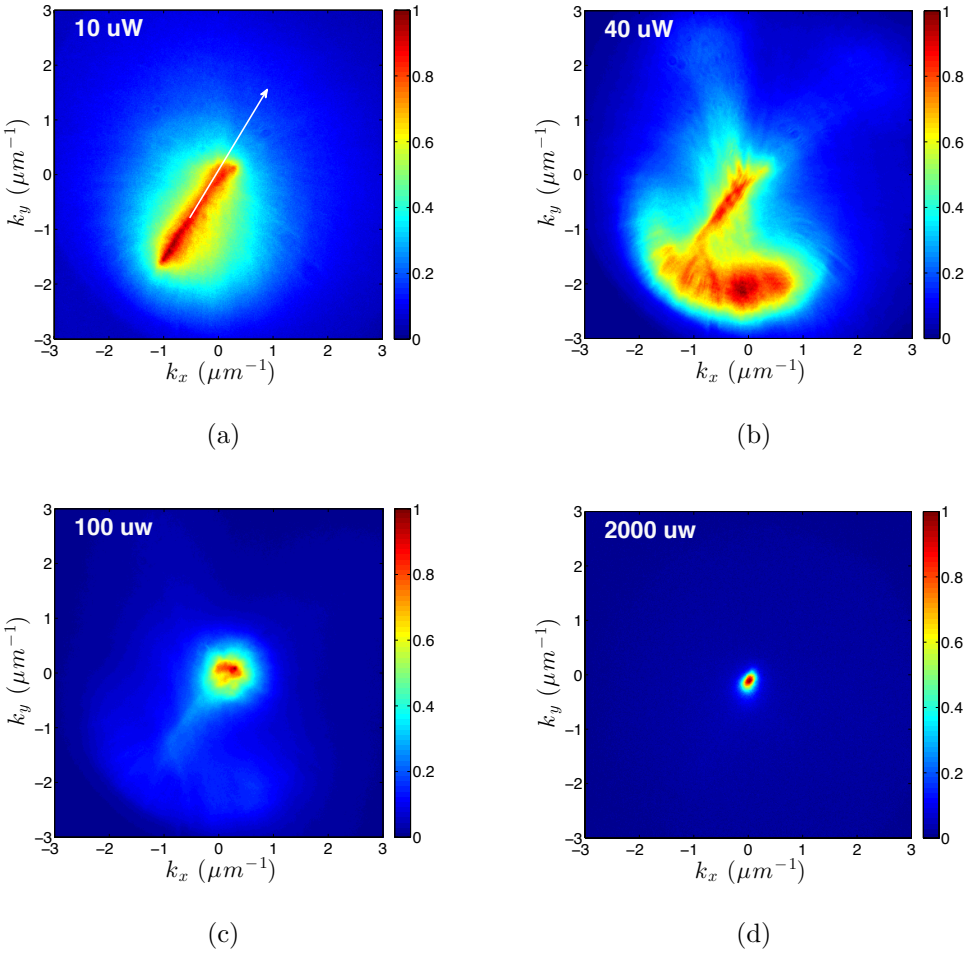

Figure 47: Momentum-space images of polaritons in the ring trap at different pump powers. (a) The pump power is 10 μW. The white arrow points to the direction of the cavity gradient. (b) The pump power is 40 μW. (c) The pump power is 100 μW. (c) The pump power is 2000 μW

.

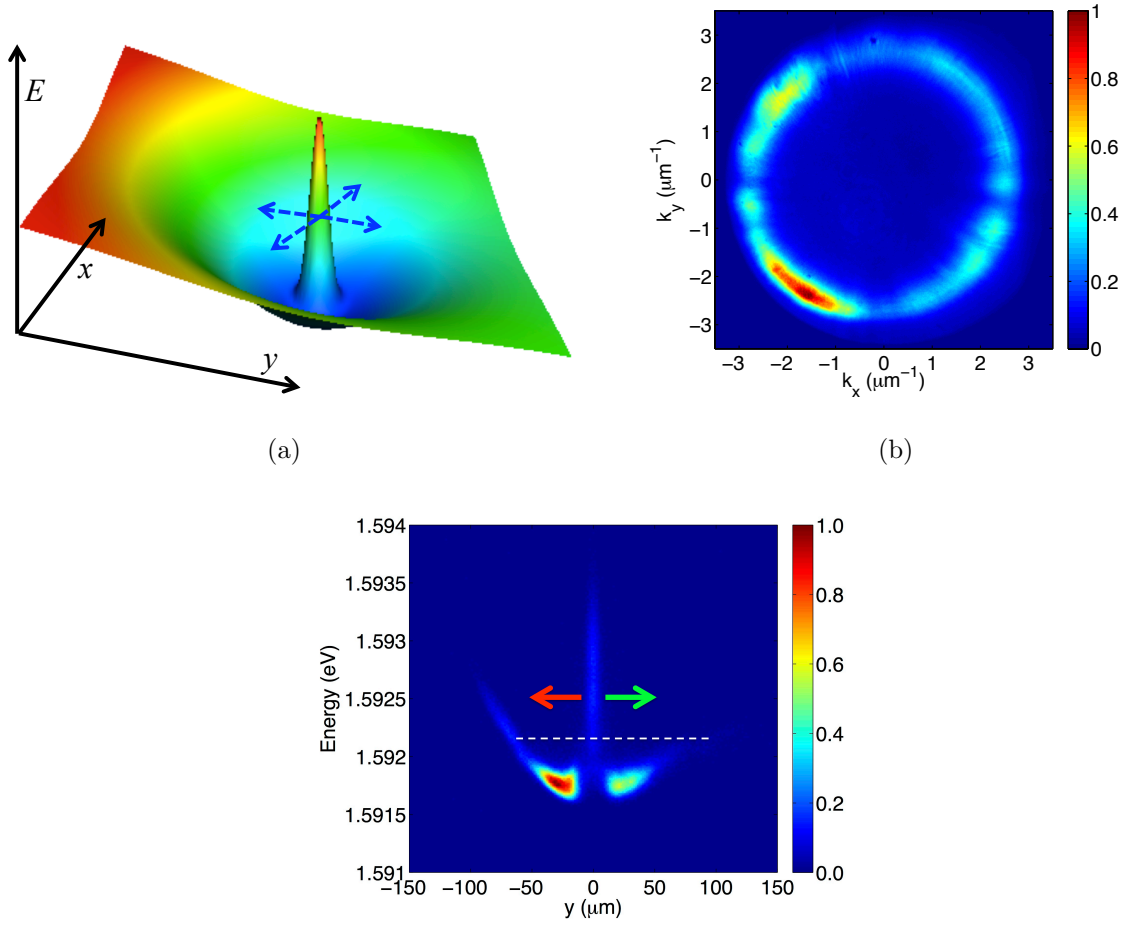

Figure 48: Schematic of the 2D profile of the ring trap and the trapping of polaritons.(a) Illustration of the titled stress trap and the exciton barrier at its center. (b) The momentum distribution of polaritons in the excitation region at the center of the stress trap. (c) Trapping of the polaritons in an 0.4 meV deep stress trap. The white dashed line shows the energy of the low side of the stress trap. Polaritons moving in the uphill direction (red arrow) are trapped by the high side of the stress trap and the exciton barrier. Polaritons moving in the downhill direction (green arrow) and with initial potential energy larger than the trap depth will escape from the trap.

they reach the excitation region at the center of the trap. Once they reach the excitation region, their momentum will rapidly reduce to zero due to the steep potential gradient of the exciton barrier. Then, they will start moving out of the excitation region again, and repeat the process described above until they decay out of the cavity. However, not all the polaritons moving towards the uphill side of the trap will oscillate in the region between the uphill side of the trap and the exciton barrier. When their initial momentum is not perfectly aligned with the cavity gradient, they will drift away from the cavity gradient direction and miss the exciton barrier when they coming back down from the uphill side of the trap. They will continue to moving away from the center of the trap and eventually escape from the trap from the downhill side of the trap. Therefore, only the polaritons with initial momentum within a certain angle to the cavity gradient direction will oscillate in the trap.

Polaritons with initial momentum in the downhill direction and kinetic energy larger than the trapping energy (1 meV in this case) will move directly out of the trap, and will gain momentum as they are moving outside the trap. The larger initial momentum they have, the shorter time they stay in the field of view of our imaging system. The time that a polariton remains in the field of view of our imaging system increases as the angle between its initial momentum and the cavity gradient increases. Therefore, the plaritons with initial momentum in the opposite direction of the cavity gradient will have the most intense signal.

The above discussion, of course, is very simplified as it does not take into account the polariton-polariton scatterings, which will change the momentum of the polaritons. But at this low pump power, the density of polaritons is low, and the scattering does not play any important role. This is proved by the fact that in Fig. 47(a) polaritons with momentum opposite to the cavity gradient has the highest intensity.

The situation changes as the pump power increases. Fig. 47(b) shows the momentum-space image of the polaritons when the pump power is 40 μW. In this case, the polaritons are distributed in a more broad range of momentum states. This is an indication of the increasing scattering between the particles. As we keep increasing the pump power, more and more polaritons start to populate the region near $k = 0$. Fig. 47(c) is the momentum-space image of polaritons when the pump power is 100 μW. At this pump power, there are more polaritons in the states near $k = 0$ than in other high k states. At a pump power

of 2000 μW, a bright spot is observed at $k = 0$ in Fig. 47(d), which corresponds to the polaritons in the ring condensate. From these momentum-space images at different pump power, we conclude that most of the polaritons in the ring condensate are the polaritons with initial momentum in the opposite direction of the cavity gradient. This feature turns out to be important to the polarization pattern of the ring condensate as we will discuss in Chapter 7.

7.0 EXPERIMENTAL STUDY ON THE ORIGIN OF THE STABLE POLARIZATION PATTERN

As discussed in Chapter 6, while analyzing the interference pattern we noticed that the difference of the fringe numbers between the top and bottom half of the ring changes randomly between ± 1 and 0; for about 90% of the time the difference is ± 1, for the remaining 10% of the time, there number of fringes is equal. This indicates that the polariton flow direction changes randomly from shot to shot. In the meantime, however, the polarization pattern of the ring condensate is very stable. The fluctuation in the flow direction of polaritons is very likely due to the fluctuations of the excitation laser: fluctuations in the laser induce fluctuations in the initial momentum distribution of polaritons which can lead to changes in the circulation state. The fact that the polarization is stable is surprising and the reason is not immediately clear. In this chapter, I will discuss my experimental investigation on the possible mechanisms responsible for the stable polarization pattern. This study indicates that the polarization pattern is very likely related to the way the ring condensate is created – polaritons are created at the center of the trap and then propagate into the ring. We believe that the special geometry of our system and the optical spin Hall effect are responsible for the stable polarization pattern.

7.1 STABLE POLARIZATION PATTERN IN THE RING TRAP

By analyzing the interference pattern in Fig. 43, we find that there is an approximately equal chance to have one more fringe in the top half of the ring or the bottom half of the ring. This implies that the direction of the circulation is changing randomly. On the other hand,

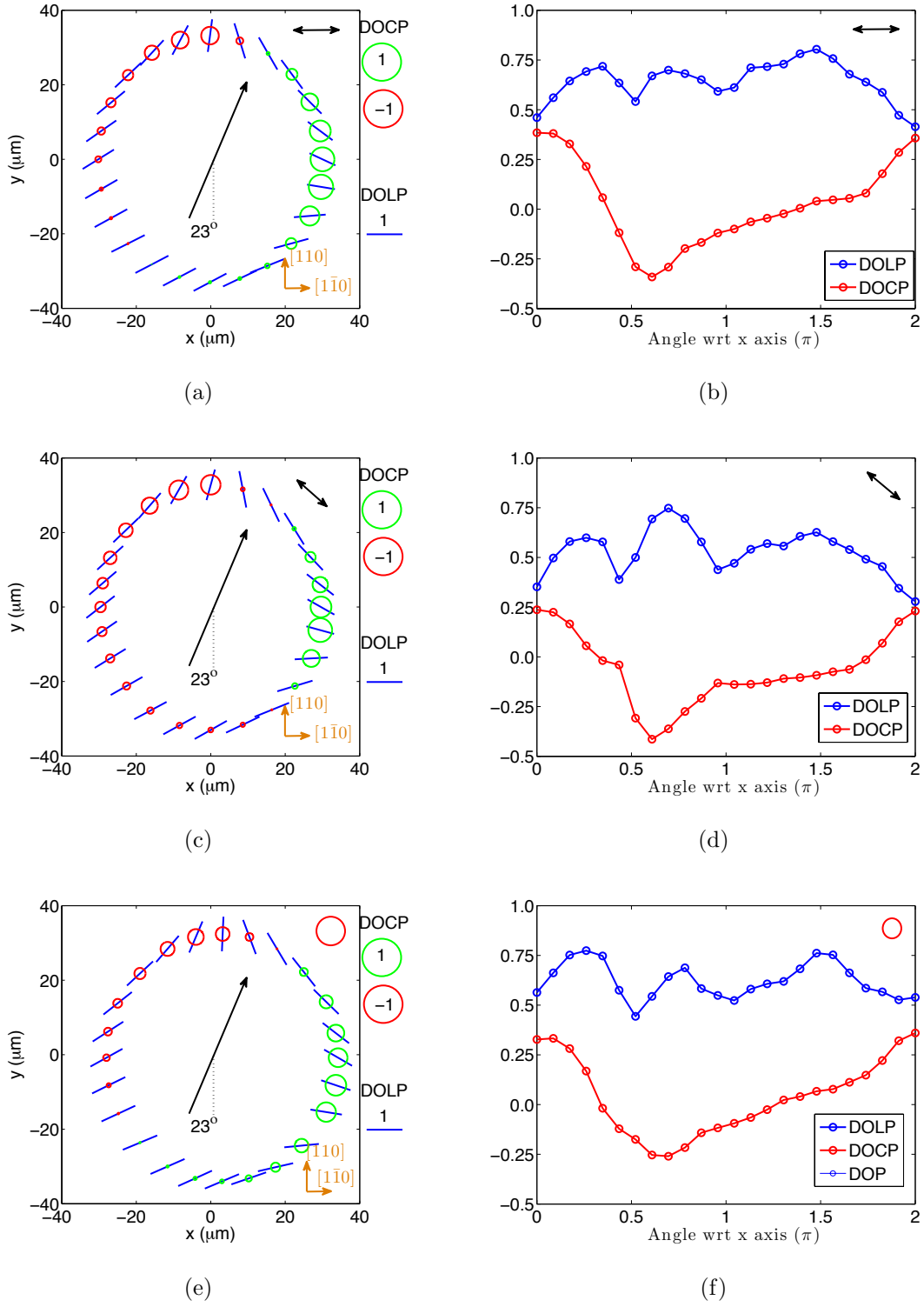

Figure 49: Polarization map of the ring condensates created with lasers of different polarizations. (a) and (b), the laser is linearly polarized in the horizontal direction. (c) and (d), the laser is linearly polarized in the direction 30° below the horizontal direction. (e) and (f), the laser is left circular polarized.

however, the polarization pattern always stays the same. This raises an interesting question: why is the polarization pattern stable? In this section, I will discuss our experimental study of several possible mechanisms that are known to induce polarization patterns in polariton condensates.

7.1.1 Effect of the Lattice Pinning

It has been shown theoretically that linear polarization in the emission spectra of polaritons will spontaneously build up when they undergo the Bose-Einstein condensation under non-resonant pumping [112, 113]. The linear polarization comes from the stable relative phase between the two degenerate spin states of polaritons in the condensate phase. On the other hand, in GaAs-based microcavity the ground state of polariton always splits into two orthogonal linear polarizations due to the crystal asymmetry and residual strain from sample growing process. As a consequence, the polarization of the condensate is always pinned to a crystal axis [15, 16, 17]. For the ring condensate, which was created in a stress trap, it therefore seems possible that the stable polarization pattern is due to the pinning to the underlying crystal lattice. However, this is not the case. Because the GaAs-based structures have a fourfold symmetry, this would lead to a fourfold rotational symmetry of the polarization of the polaritons [81, 82]. In the current case, both the linear polarization and circular polarization of the ring condensate only rotate by 180°.

7.1.2 Effect of the Pump Laser Polarization

The polarization of the pump laser can also affect the polarization of the condensate even in a non-resonant pumping method. Using a non-resonant pumping method different from ours, Roumpos *et al.* [114] showed that when the pump laser is linearly polarized, the emission of the condensate develops both nonzero linear and circular polarization. They observed rotation of the linear polarization axis by $\sim 90°$ between the pump laser and the condensate. This rotation is due to the spin anisotropy of the polariton-polariton interactions. The circular polarization comes from the rotation of the Stokes vector induced by the energy splitting between the two linearly polarized eigenstates.

The correlation between the pump laser and the polaritons observed by Roumpos and colleagues can be understood as a result of insufficient spin relaxation in their system. Their experiments were done with polaritons of lifetimes about 10 ps, which is shorter than typical spin-relaxation time of 100 ps [116]. The pump laser in their experiments was at the exciton resonance wavelength, just a few meV above the polaritons energy, which directly injects excitons with the same polarization as the pump laser into the cavity. Due to the lack of spin relaxation, polarization of the laser is preserved in polaritons. In fact, the 90° rotation of the linear polarization axis between condensate and pump observed in their experiments implies that there was only one polariton-polariton scattering event before a polariton reaches the ground state.

In contrast, polaritons in our microcavity have lifetimes about 270 ps, which is much longer than polariton scattering time and spin relaxation time. In addition, the photon energy of the pump laser in our experiment is $\sim$ 100 meV above the exciton resonance. The pump laser creates hot carriers in the cavity, which then cool down to form excitons. During this process, information of pump laser, such as phase and polarization, is believed to be completely lost. Therefore there should be no correlation between the pump laser polarization and the polariton polarization.

In order to verify our argument, we created ring condensates using pump lasers with different polarizations and then measured their polarizations. Fig. 49 shows the polarization maps of ring condensates created with three different pump laser polarizations: (a) linear polarization along the horizontal direction, (b) linear polarization along 30° above the horizontal direction, and (c) left circular polarization. It can be seen that the polarizations are nearly the same for different laser polarizations. Therefore, we conclude that the polarization of the ring condensate is independent of the laser polarization.

It is worth to note that in a work done by Kammann *et al.* [131], in which the microcavity was excited with a circularly polarized laser with photon energy more than 100 meV higher than the polariton energy, a polariton condensate with the same circular polarization as the pump laser was observed. Again, in this work the polariton lifetime was only a few picoseconds, and the correlation between the condensate polarization and the pump laser polarization was due to the insufficient spin relaxation of the polaritons.

7.1.3 Effect of the Polariton Density Variation

In addition to the mechanisms discussed above, we studied the possible connection between the polarization and the density profile of the condensate. Comparing Fig. 40(c) and Fig. 45(a), one notices that in the upper-right and lower-left parts of the ring where the polariton density is high, the degree of the circular polarization is nearly zero. Whereas in the middle-right section where the polariton density is low, the condensate has a large circular polarization component. These features suggest that there might be a connection between the density profile and the polarization profile.

In order to determine the possible connection, we created ring condensates with different density profiles and measured the polarizations in each case. Fig. 50(a) shows a ring condensate with a density profile nearly opposite to that of the ring condensate shown in Fig. 40(c); the polariton density is high in the right side and upper-left side of the ring. Presumably, polaritons in these regions should be less circularly polarized than in other regions where the density is low. However, as shown in Fig. 50(b) and Fig. 50(c), the degree of circular polarization in these high density regions are much larger than that in low density regions. In fact, this polarization profile is nearly the same as that of the ring condensate shown in Fig. 40(c). The current ring condensate has larger overall degree of polarization, because it has higher average density of polaritons in the condensate. The similarity between the polarization patterns of these two ring condensates implies that the particle density has no significant effect on the polarization of the ring condensate.

An even stronger evidence showing the polarization pattern is not correlated with the density distribution is given by the polariton cloud shown in Fig. 50(d), which is obtained by moving the pump spot (white cross) 14.3μm away from the trap center (red cross) along the direction perpendicular to the cavity gradient. In this case, polaritons condensed into the region on the right side of the pump spot, with is the global minimum of trap potential. On the left side of the pump spot, the trap energy is 0.4 meV higher than that on the right side, thus density of polaritons is low and they remain in a thermal state. It is very surprising to see, from Fig. 50(e) and Fig. 50(f), that the polarization map of this polariton cloud is again very similar to that of the ring condensate shown in Fig. 50(a) and Fig. 40(c): the

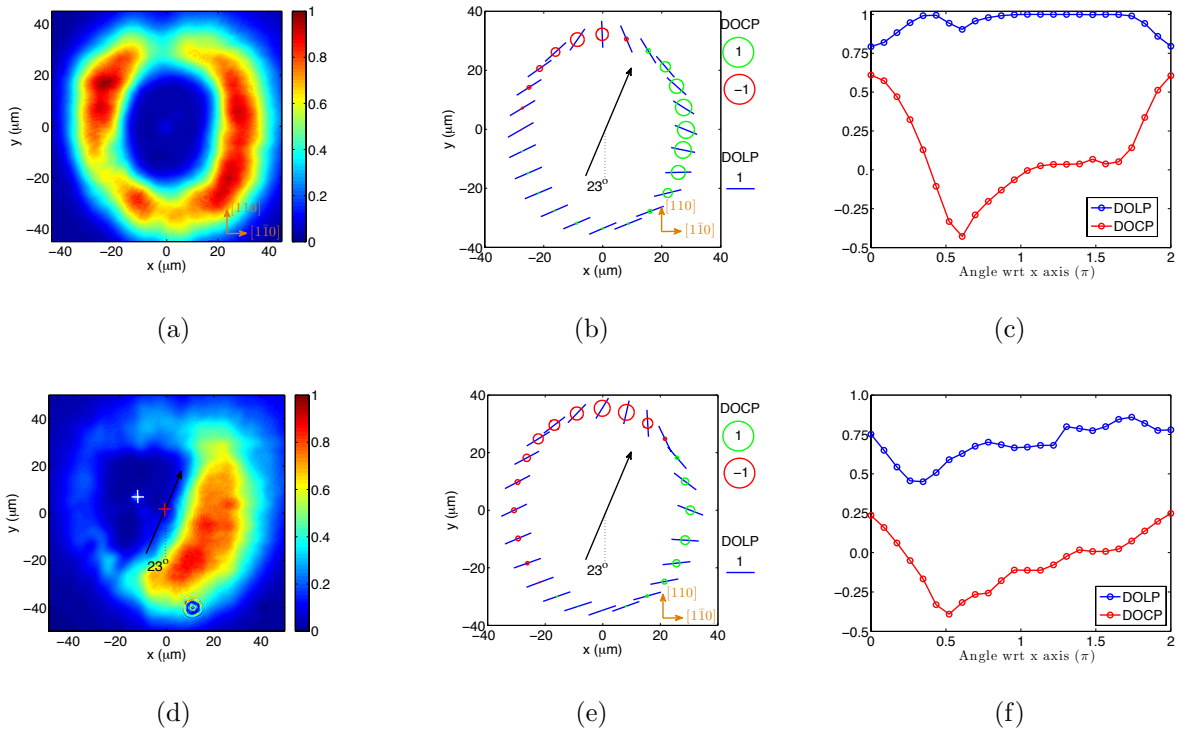

Figure 50: Polarization map of a ring condensate and a condensate that fills part of the ring trap. (a) The real-space image of a ring condensate obtained under the same conditions as that of Fig. 40(c). (b)–(c) The degree of linear polarizatioin (DOLP) and circular polarization (DOCP) of the ring condensate in (a). (d) Real-space image of polariton condensate in a tilted ring trap. The pump spot (white cross) is shifted by 14.3 μm away from the center of the stress trap (red cross) along the direction perpendicular to the cavity gradient (dark arrow). (e)-(f) The degree of linear polarization (DOLP) and circular polarization (DOCP) of the condensate shown in (d).

linear polarization rotates around the ring, and the handedness of the circular polarization are opposite on each side of the ring. This provides a very strong proof that the polarization pattern is independent of the density distribution of polaritons.

7.2 A POSSIBLE MECHANISM FOR THE POLARIZATION PATTERN

In Section 7.1, I experimentally investigated several possible mechanisms for the stable polarization pattern of the ring condensate, and found none of them had significant effect on the polarization of the condensate. In this section, I will first introduce the concept optical spin Hall effect [122] and discuss why I think it is a possible mechanism for generating the polarization pattern observed in the ring condensate.

7.2.1 Optical Spin Hall Effect

The optical spin Hall effect is the analogy of the spin Hall effect (SHE) [118, 119, 120, 121] in semiconductor optics. It was first predicted by Kavokin and coworkers in their study of the Rayleigh scattering of light [122]. Later on, this effect was observed in a microcavity polariton system [123] and a photonic cavity [124] under the resonant pumping scheme. These experiments rely on the Rayleigh scattering with defects in the sample, therefore, they are analogous to the extrinsic SHE [118]. Recently, the OSHE analogous to the intrinsic SHE [120, 121] is observed in a radially expanding polariton condensate [131].

The OSHE of polaritons originates from the precession of the polariton pseudospin induced by the longitudinal-transverse splitting (Δ_{LT}, LT splitting) of polaritons [122, 126, 127, 128]. This splitting comes from the transverse electric and magnetic mode splitting (TE-TM splitting) of the cavity photon. The LT splitting depends on the in-plane wave vector of the polaritons, and plays the role as a directional dependent effective magnetic field in the cavity plane.

When this effective magnetic field is considered, the propagation of the polaritons in the

cavity plane can be described by the the following effective Hamiltonian [122]:

$$\hat{H} = \frac{\hbar^2 k^2}{2m} + \mu_B g(\vec{\sigma} \cdot \vec{H}_{\text{eff}}) \tag{7.1}$$

where $\vec{k} = (k_x, k_y)$ is the in-plane wave vector of the polariton, m is the mass of the polariton, μ_B is the Bohr magneton, g is g-factor, $\vec{\sigma}$ is the Pauli matrix vector, $\vec{H}_{\text{eff}} = \hbar\vec{\Omega}(\vec{k})/(\mu_B g)$ is the effective magnetic field with $\vec{\Omega}_{\vec{k}}$ having the following components:

$$\Omega_x = \frac{\Delta_{\text{LT}}}{\hbar k^2}(k_x^2 - k_y^2), \quad \Omega_y = 2\frac{\Delta_{\text{LT}}}{\hbar k^2} k_x k_y. \tag{7.2}$$

Fig. 51(a) shows the orientation of the effective magnetic field (blue arrow) for in-plane wave vectors of the same magnitude but with different directions (circle). For a polariton with initial pesudospin $\vec{s}$, the time evolution of the pesudospin is described by [122]

$$\frac{\partial \vec{s}}{\partial t} = \vec{s} \times \vec{\Omega}_{\vec{k}} + \vec{f}(t) - \frac{\vec{s}}{\tau}, \tag{7.3}$$

where $\vec{s}$ is the pseduospin, $\vec{f}(t)$ is the flux of polaritons coming into this state, τ is the lifetime of the polariton. This equation ((7.3)) successfully reproduced the polarization pattern of polaritons observed in various experiments [123, 131].

7.2.2 Optical Spin Hall Effect In the Ring Trap

In order to see how the OSHE relates to the polarization pattern of our ring condensate (Fig. 45(a)), let us first apply the Eq. (7.3) to a radially expanding polariton condensate which is linearly polarized along the x direction. Such a condensate has been created and studied by several groups [130, 131], and it closely relates to our experiments in the ring trap, as I will discuss later in this section. The radially expanding condensate is typically created by nonresonantly pumping the microcavity with a tightly focused laser spot [130, 131]. The tightly focused laser creates a steep exciton potential barrier and polaritons in the excitation spot. When the polariton density is high enough, a condensate is formed on top of the exciton barrier. Due to the strong repulsion from excitons, polaritons move away from the excitation spot resulting in the expansion of the condensate. As it expands, its potential energy converts to the kinetic energy in the radial direction. When the scattering with defects

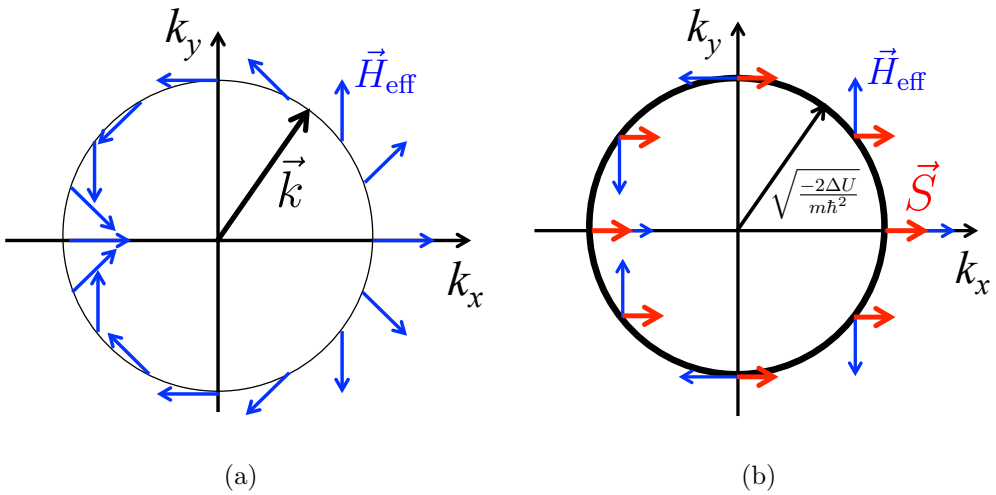

Figure 51: (a) The direction of the effective magnetic field (blue arrow) induced by the longitudinal-transverse splitting of the polaritons with an isotropic momentum distribution (black ring). (b) The initial momentum (black ring) distribution and polarization (red arrow) of a radially expanding polariton condensate.

and other polaritons is negligible and the cavity is isotropic, the momentum distribution of the expanding condensate will be a ring with a radius of $k = \sqrt{-2\Delta U/m\hbar^2}$ (see Fig. 51(b), where ΔU is the blueshift of the potential energy barrier from which they are launched.

Fig. 51(b) shows the initial momentum distribution (dark thick circle) and polarization of the polaritons (red arrow) of the radially expanding condensate. It also shows the direction of the effective magnetic field (blue arrow) they experience. In fact, the situation shown in Fig. 51(b) is the same as that of the Rayleigh scattering of a polariton cloud, which is linearly polarization in the x direction, with defects in the sample. The later case was studied numerically and experimentally in Ref. [122] and [123], respectively. As the time evolution of the pesudospins in these two cases are both governed by Eq. (7.3), and the initial conditions are the same, the pesudospin patterns should be the same. Thus, I will use the results from Ref. [123] for the discussion hereafter.

Fig. 52 shows the circular polarization degree of polaritons obtained by simulating the

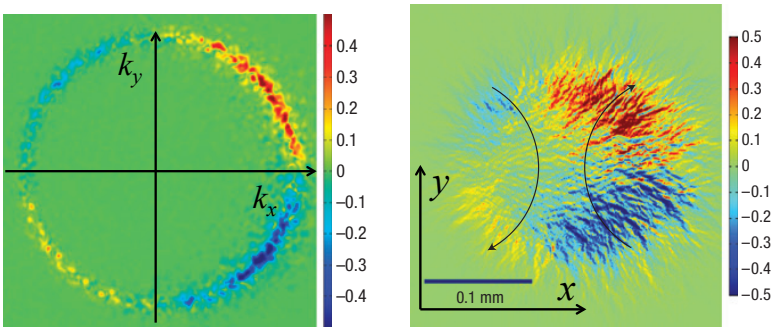

(a) (b)

Figure 52: Simulation of the momentum-space and real-space circular polarization degree of a polariton cloud with initial momentum and polarization given in Fig. 51(b). (a) The circular polarization degree in momentum space. (b) The circular polarization degree in real space. These figures are taken from Ref. [123].

time evolution of the polariton pesudospin with Eq. (7.3) and with the initial condition given in Fig. 51(b). One can see that opposite circular polarization components are separated both in momentum space and real space. This should also be the polarization pattern of a radially expanding condensate which has initial momentum and polarization given by Fig. 51(b).

One might already notice the similarity between Fig. 52(b) and the circular polarization degree of our ring condensate shown in Fig. 45(a). In fact polaritons in our ring trap share some common features with the radially expanding condensate discussed here: a polariton cloud is created on top of a exciton barrier at the center of stress trap and then expands in the radial direction due to the repulsion from the excitons. The momentum distribution, shown in Fig. 48(b), of the polaritons moving out of the pump region is similar to that of the radially expanding condensate shown in Fig. 51(b).

The major difference between the polarization profiles in Fig. 45(a) and Fig. 52(b) is that in Fig. 45(a) the circular polarization flips its sign twice along a closed loop around the ring condensate, while in Fig. 52(b) it flips the sign four times along a closed loop around the radially expanding condensate. Such a difference is caused by the asymmetry of the ring

trap. As discussed in Section 6.4, this ring trap collects polaritons with initial momentum in the uphill direction much more efficiently than polaritons with initial momenta in other directions. This effect leads to the highly anisotropic momentum distribution of polaritons in the ring trap, as shown in Fig. 47. Another important consequence of this effect is that the ring condensate is mostly generated from the polaritons with initial momentum in the uphill direction. Let us assume that the uphill direction of the ring trap is parallel to the x direction in Fig. 52(a). Then the ring condensate would be formed mostly by the polaritons with $k_x \geq 0$. Therefore, the circular polarization of the ring condensate will be the same as that of the right half of Rayleigh ring in Fig. 52(a); the circular polarization has opposite signs on the two sides of the cavity gradient direction.

There is still one thing that needs to be discussed: to get a polarization pattern like the one shown in Fig. 52(b), the initial state of polaritons needs to be polarized, so, are the polaritons created at the center of the stress trap polarized before they moving into the ring trap to form the ring condensate? My recent experiments showed that these polaritons indeed were polarized when the pump power was above the condensation threshold. Fig. 53(a) shows the real-space image of a polariton ring condensate. Fig. 53(b) and 53(c) show the degrees of linear polarization and of circular polarization of the polaritons in the region enclosed by the ring condensate (inside the black dashed circle in Fig. 53). A linear polarization degree of 0.76 and a circular polarization degree of 0.27 were observed in the pump spot (red dashed circle). The linear polarization of the polaritons was along the $[1\bar{1}0]$ direction. As I discussed in Section 3.4, the state with linear polarization along this direction has lower energy than the state with linear polarization along the [110] direction. Thus, these polaritons were in the lowest energy state in the pump spot. When the pump power was below the condensation threshold, the polartions in this region were unpolarized; the polarization degree of these polaritons did not exceed 0.2, which was the noise polarization in the background. This nonzero background polarization noise level was the maximum polarization of the PL from a single pixel (0.2 μm by 0.2 μm) of the image. When averaged over many pixels, the noise polarization approached to zero. The nonlinear increase of the polarization in the pump spot indicated that a condensate was formed in this region. This condensate expands due to the repulsion from the excitons, which makes it very similar to the expanding condensates

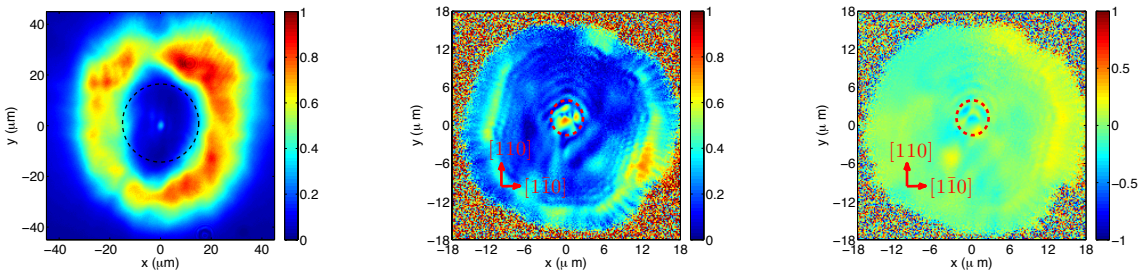

(a) (b) (c)

Figure 53: Polarization of polaritons in the pump region above condensation threshold. (a) Real-space image of the ring condensate when the pump power is above the condensation threshold. The black dashed circle encloses the region in which the polarization is measured in (b) and (c). (b) The degree of linear polarization of the region enclosed by the black dashed circle in (a). The red circle indicates the boundary of the pump region. The linear polarization in the pump region is mostly along the $[1\bar{1}0]$ direction. (c) The degree of circular polarization of the same region in (b).

studied in [130, 131]. The linearly polarized condensate in the pump spot provided the initial condition for the OSHE to generate the polarization pattern in the ring trap.

The polarization of polaritons in the ring trap exhibited a similar nonlinear increase as the pump power increases. Fig. 54 shows a typical set of data of the average polarization in the ring trap for different pump powers. A drastic increase of the polarization is observed when the pump power goes from below condensation threshold to above the condensation threshold. Below the threshold, the polaritons were unpolarized, as their degree of polarization (DOP) was the same as the background noise level. Above the threshold, the polaritons become polarized and the degree of polarization kept increaseing with the pump power. In this particular case, the degree of polarization reached 0.72 when the pump power was 2.4 mW. Fig. 55 shows the real-space images of the polaritons in the ring trap at several different pump powers. The corresponding degrees of linear polarization (DOLP) and of circular polarization (DOCP) are shown in second and third columns of Fig. 55. It is very clear that the polaritons become polarized when the pump power goes above the condensation threshold, and they become more and more polarized as the pump power increases.

It is worthwhile to point out that the optical spin Hall effect does not require the existence of a condensate. However, to generate a polarization pattern in a system with a large number of polaritons, the initial state of the system needs to have a non-zero polarization order. Otherwise, there would not be a polarization pattern since the randomness in the initial polarization of the polaritons would wash out any non-zero polarization degree. The condensate provides the necessary initial polarization state for the system to develop a polarization pattern under the optical spin Hall effect. Also, the condensate greatly enhances the stimulated scattering process between polaritons, which favors polaritons in the same state. This effectively amplifies the polarization degree of the system.

The above discussion and observations show that the optical spin Hall effect and the asymmetric trap profile can explain the polarization pattern of the ring condensate shown in Fig. 45(a). Furthermore, the stability of the polarization pattern of the ring condensate can also be understood as a consequence of the OSHE; the polarization pattern generated by the OSHE is determined by the momentum distribution and the polarization of the initial state of the polaritons, which were not changed when I altered the pump laser polarization and

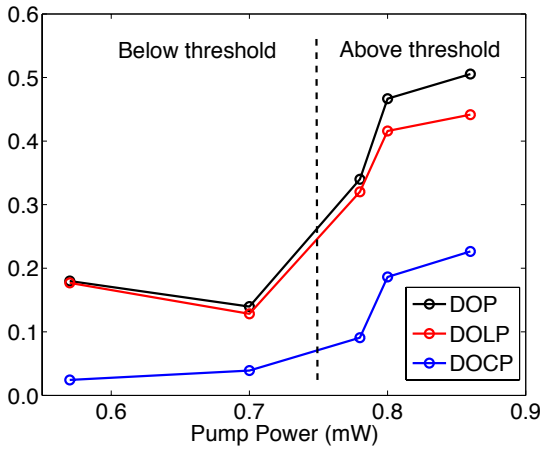

Figure 54: Average polarization of polaritons in the ring trap at different pump powers. Black circle: the degree of polarization (DOP). Red circle: the degree of linear polarization. Blue circle: the degree of circular polarization. The lines are guide to the eye. At each pump power, the average polarization is calculated by averaging over the polarizations at 24 equally spaced locations around ring trap (see Fig. 50(b) for example). The vertical dashed line represents the threshold pump power in this, which is 0.75 mW.

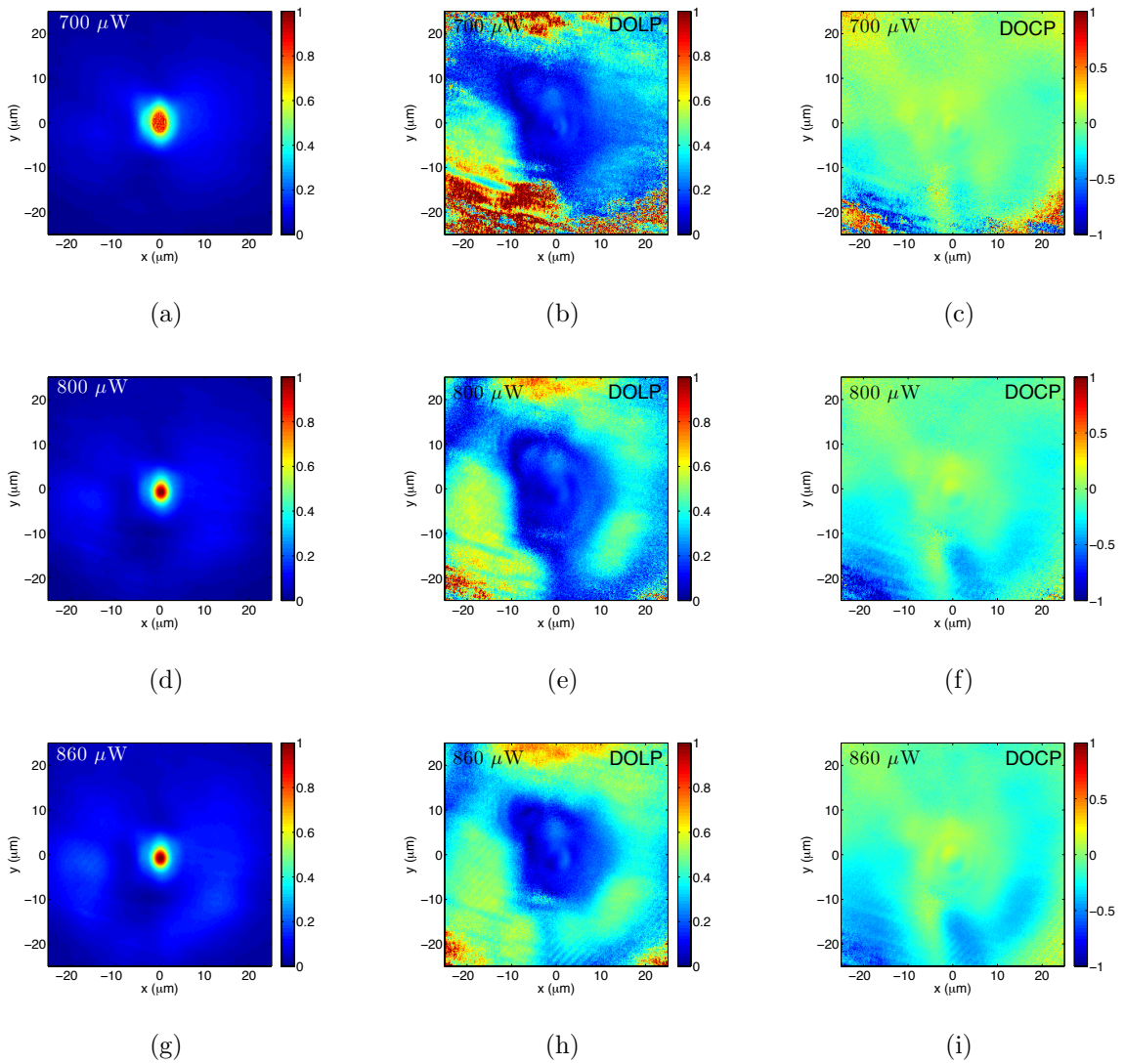

Figure 55: Polarization of polaritons in the ring trap for different pump powers. (a) – (c), the pump power is 700 μW. (a) is real-space image of the polaritons, (b) and (c) are the degree of linear polarization (DOLP) and degree of circular polarization (DOCP), respectively. (d) – (f), the pump power is 800 μW. (d) is the real-space image of the polaritons, (e) and (f) are the DOLP and DOCP of the polaritons, respectively. (g) – (f), the pump power is 860 μW. (g) is the real-space image of the polaritons, (h) and (i) are the DOLP and DOCP of the polaritons, respectively.

density profile of the polaritons in the way described in Section 7.1.

One thing that remains unclear is the energy relaxation mechanism of the polaritons in the ring trap. The polaritons have high in-plane momentum when they leave the pump region. But they eventually relax down to the ground state of the trap and forms the ring condensate. It is likely that the out-flowing polaritons collide with the polaritons coming back from the higher energy side of the stress trap, and one of them goes into ground state and the other goes to higher energy state. We have seen evidence for this in several experiments of our own [22] and others [20], in which a thermal condensate only formed in regions where there are polaritons flowing in opposite directions. When the polariton density is low, the polariton-polariton scattering is weak. But when the polariton density is high, stimulated scattering greatly enhances this process, therefore leading to the formation of a condensate. More experimental and theoretical work is need to understand the energy relaxation of the polaritons in the ring trap.

8.0 CONCLUSION AND FUTURE DIRECTIONS

8.1 CONCLUSION

The goal of this thesis was to investigate the Bose-Einstein condensation and superfluidity of polaritons with long lifetimes. In the first part of this thesis, this was done by nonresonantly exciting the sample with a laser, and studying the properties of the polaritons as a function of their density. It was observed that, at low density, the polaritons propagated ballistically over hundreds of microns in the microcavity. At moderate density, most of the polariton entered into a dissipationless flow state. These polaritons propagated over hundred microns while maintaining their phase coherence. When the polariton density was above a critical threshold, they made a sudden transition from the flow state to a trapped state in the quasi-1D trap formed by the exciton barrier and the cavity gradient. This transition was accompanied by a very sharp decrease in the polariton spectral line width, and a condensation to the in-plane momentum ground state. In addition, it was also observed that this transition was much sharper than transitions observed before with short-lifetime polaritons. This feature was attributed to the better thermalization achieved among these long lifetime polaritons. An interesting quesiton remains to be answered is how the polaritons relaxed their energy when they made the sharp transition from the coherent flow state to the trapped state.

In the second part of this thesis, the properties of the polaritons in a ring-shaped trap were studied. This ring trap was created by combining an optically generated potential barrier and a stress-induced harmonic trap. It was shown that when the trap was deep, polaritons could relax down to the ground state of the trap and form a ring-shaped cloud. However, the spatial coherence length of this ring cloud was only a small fraction of its

size. Thus, this single-energy polariton ring cloud could not be regarded as a condensate. Various experiments were done in order to improve our understanding of the origin of this short coherence length. In the end, it turned out that the large exciton fraction (0.73) of the polaritons was responsible for it; With such a large exciton fraction, polaritons interact strongly with each other and become less mobile, therefore, were unable to synchronize their phase with other polaritons far apart. Based on this understanding, another series of experiments were carried out in a shallower trap, in which the polaritons had a smaller exciton fraction (0.48). It was observed that in this shallow trap, the polaritons were unable to relax to the ground state of the trap. Instead, they stayed in states with multi-lobe density patterns along the radial direction of the trap. These states were interpreted as standing-waves formed by polaritons moving back and forth in the trap.

The experiments with different trap depths showed that the strength of the interaction between polaritons was crucial for polaritons to achieve both spatial and energy equilibration. It also showed that the stress trapping method allowed fine tuning of this critical property. By carefully adjusting the interaction strength of the polaritons, eventually a fully coherent polariton ring condensate was created. Phase-resolved and polarization-resolved measurements revealed that this the ring condensate was in a new type of half-quantum circulation state; a state featured a phase shift of π and a polarization vector rotation of π of the polaritons around a closed path in the ring. It was also found that the direction of circulation of the flow around the ring fluctuated randomly between clockwise and counter-clockwise from one shot to the next. In contrast, the rotation of the polarization of polaritons were very stable. This property was experimentally studied, and it was found that the stable spatial polarization pattern was very likely relate to the optical spin Hall effect. Further experiments and numerical simulations are needed to improve our understanding of the connection between the polarization pattern of the ring condensate and the OSHE.

8.2 FUTURE DIRECTIONS

8.2.1 Time Resolving the Jump of the Flow Direction of the Ring Condensate

An interesting property of the ring condensate discussed in Chapter 5 is that the direction of the polariton flow in the ring trap fluctuates between clockwise and counterclockwise from shot to shot. In these experiments, the pump beam is modulated by a mechanical chopper at 400 Hz with a duty cycle of 1% to reduce heating of the sample. The integration time of the CCD was set to 1 ms to ensure that each image corresponded to only one laser pulse (Fig. 8.2.1(a)). If a larger duty cycle was used, namely the pump beam was kept on for a longer time, the flip of the flow direction might be recored in a single shot. Fig. 8.2.1(b) illustrates the idea of this experiment.

8.2.2 Generating Quantized Circulation State on Demand

In our current experiments only the states of angular momentum $\pm\hbar/2$ have been generated. It is therefore interesting to develop methods to generate quantized circulation states with higher angular momenta. Here, we propose two different methods for generating higher angular momentum states in the ring trap. The first method is illustrated in Fig. 57(a), where a polariton droplet with initial in-plane momentum $\vec{p}_0$ is resonantly injected into a ring condensate of radius r. This droplet carries angular momentum $\vec{J}_i = N(\vec{r} \times \vec{p}_0)$ into the ring condensate, where N is total number of polaritons in this droplet. Suppose the ring condensate is circulating in clockwise direction with angular momentum $\hbar/2$ and there are N_0 polaritons in the condensate. After the injection of the polariton droplet, the magnitude of the total angular momentum of the system is

$$J = N(r \cdot p_0) + N_0\hbar/2. \tag{8.1}$$

By adjusting the number of injected polaritons (N) and their initial momentum ($\vec{p}_0$), the ring condensate can be driven to different angular momentum states. For example, to drive the ring condensate to the state with angular momentum $\hbar$, namely

$$(N + N_0)\hbar = N(r \cdot p_0) + N_0\hbar/2, \tag{8.2}$$

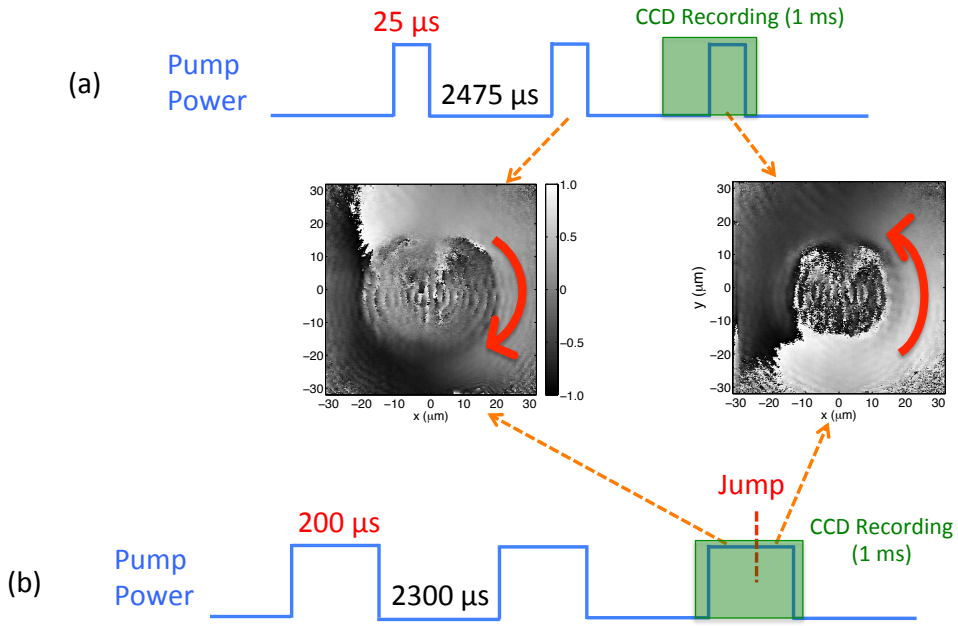

Figure 56: (a) Schematic of current pumping and data recording setting. The blue line is the modulated pump power. It is set to have its full power for 25 μs and zero power for 2475 μs. The CCD camera integrates the PL over a 1 ms time window (green rectangle). (b) Schematic of a different setting that will be used to record the jump of the polariton flow direction. The pump beam is kept on for 200 μs and all the other conditions are kept the same. The red arrows in the phase maps represent the flow direction of the polaritons.

one can inject $N_0/[2(rp_0/\hbar-1)]$ polaritons with initial momentum $\vec{p}_0$ into the ring condensate. The circulation direction of the ring condensate can also be reversed by injecting polaritons with initial angular momentum opposite to that of the ring condensate. Therefore, with this method we will have full control of both the magnitude and direction of the angular momentum of polaritons in the ring trap.

In the above discussion, one has assumed that the injected polaritons will be absorbed by the ring condensate. However, it is also possible that the injected polaritons will not be absorbed by the ring condensate. This can happen for example when the injected poalritons are polarized differently from the polaritons in the ring trap. In this case, the injected polaritons might travel as a soliton in the condensate which is also a very interesting phenomenon to study.

The second method of generating a well-controlled quantized flow in the ring trap is illustrated in Fig. 57(b). In this method, the pump beam (red) has an S-shaped profile centered at the stress trap. This S-shaped pump profile can be easily generated by a spatial light modulator (SLM). Due to the special geometry of this pump beam, net flows of polaritons (wide orange arrows) are generated as they move away from the excitation region due to the repulsion from the excitons. After reflecting off the boundary of the stress trap, some of these polaritons start circulating in the ring trap forming the quantized flow. The magnitude of the angular momentum of a polariton is determined by its initial momentum which comes from the potential energy in the excitation region. The potential energy is controlled by the intensity of the pump beam, therefore by changing the pump intensity the angular momentum of the polariton can be changed. As seen from Fig. 57(b), the direction of the circulating flow is determined by the orientation of the S-shaped pump profile. This provides the control of the flow direction; by inverting the orientation of the pump profile, the direction of the circulating flow can be inverted.

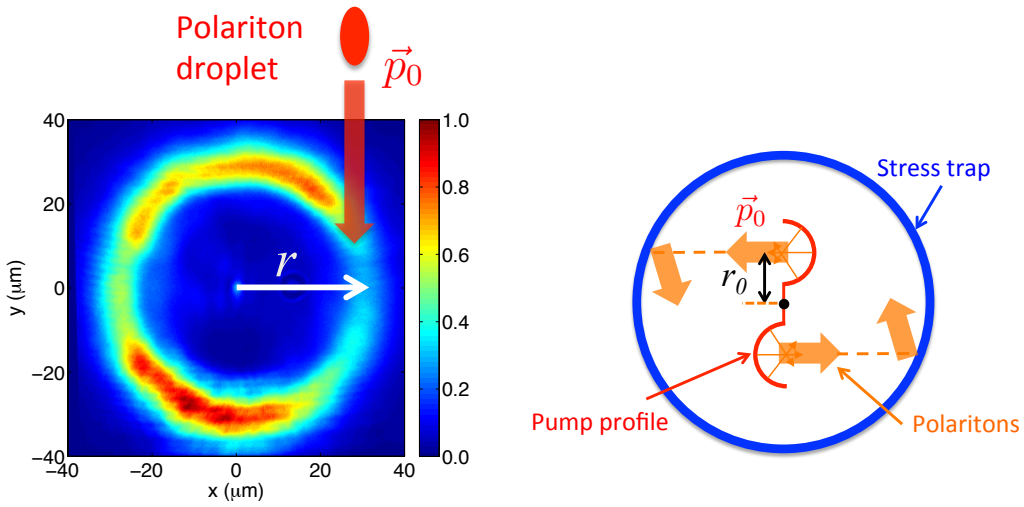

(a) (b)

Figure 57: (a) Illustration of generating quantized flow states in the ring trap by resonantly injecting polaritons into a ring condensate. (b) Illustration of the pumping the sample with an S-shaped laser beam to generate quantized flow in the ring trap.

APPENDIX A

DEPHASING OF A CLOSED INTERACTING MANY-BODY SYSTEM

In this chapter, I will present a theoretical study of the decoherence in a closed interacting many-body system. In this work, we show that by using modern quantum field theory it is possible to deduce irreversible behavior for a closed system entirely on the basis of wave mechanics without invoking any of the common extra-mathematical notions of particle trajectories, collapse of the wave function, measurement, or intrinsically stochastic processes. A novel result of our calculation is that interacting many-body systems in the infinite volume limit evolve toward diagonal states (states with loss of all phase information) on the the time scale of the interaction time. The connection with the onset of off-diagonal phase coherence in Bose condensates is also discussed. Here, I will first give a brief summary of the quantum Boltzmann equation. Then I will present the calculation of the decoherence of a closed interacting many-body system.

The results presented here have been published in "The basis of the Second Law of thermodynamics in quantum field theory," Annals of Physics **327(7)**, 1825 (2012) [132]. I contributed to this paper by verifying the derivation of the Boltzmann equation, and calculating the time evolution of the off-diagonal elements of the density matrix.

A.1 SUMMARY OF THE QUANTUM BOLTZMANN EQUATION

The equation which describes the evolution of a many-body system toward equilibrium is commonly known as the quantum Boltzmann equation. Let me first briefly summarize the derivation of the quantum Boltzmann equation (see Ref. [132] for more details). For the derivation, the model system is a many-body system that involves a number-conserving interaction between its particles. The interaction has the form,

$$\hat{V} = \frac{1}{2} \sum_{k_1,k_2,k_3} U_{k_1,k_2,k_3,k_4} a^\dagger_{k_4} a^\dagger_{k_3} a_{k_2} a_{k_1}. \tag{A.1}$$

where U_{k_1,k_2,k_3,k_4} is the interaction strength, $a^\dagger_k$'s and a_k's are the creation and destruction operator of the state with momentum k. The Hamiltonian of this system can be written as,

$$\begin{aligned} \hat{H} &= \hat{H}_0 + \hat{V} \\ &= E_0 + \sum \hat{N}_k \hbar\omega_k + \frac{1}{2} \sum_{k_1,k_2,k_3} U_{k_1,k_2,k_3,k_4} a^\dagger_{k_4} a^\dagger_{k_3} a_{k_2} a_{k_1}, \end{aligned} \tag{A.2}$$

where E_0 is the ground state energy, $\hat{N}_k = \hat{a}^\dagger_k \hat{a}_k$ is the number operator of the momentum state k. The evolution of the system can be found by using time-dependent perturbation theory (e.g., Ref. [134]). If the initial state of the system is $|\psi_i\rangle$, and the state of the system at some later time t is $|\psi_t\rangle$, the change in the average number of particles in state $\vec{k}$ is given by

$$\begin{aligned} d\langle\hat{N}_k\rangle &= \langle\psi_t|\hat{N}_k|\psi_t\rangle - \langle\psi_i|\hat{N}_k|\psi_i\rangle \\ &= \langle\psi(t)|e^{iH_0 t/\hbar}\hat{N}_k e^{-iH_0 t/\hbar}|\psi(t)\rangle - \langle\psi_i|\hat{N}_k|\psi_i\rangle \\ &= \langle\psi_i|e^{(i/\hbar)\int \hat{V}(t)dt}\hat{N}_k e^{-(i/\hbar)\int \hat{V}(t)dt}|\psi_i\rangle \\ &\quad -\langle\psi_i|\hat{N}_k|\psi_i\rangle \\ &= \langle\psi_i|e^{(i/\hbar)\int \hat{V}(t)dt}[\hat{N}_k, e^{-(i/\hbar)\int \hat{V}(t)dt}]|\psi_i\rangle, \end{aligned} \tag{A.3}$$

where $|\psi(t)\rangle = e^{iH_0 t/\hbar}|\psi_t\rangle$ and $\hat{V}(t) = e^{iH_0 t/\hbar}\hat{V}e^{-iH_0 t/\hbar}$ in the standard interaction notation. The operator $\hat{N}_k$ commutes with H_0, by definition. If it commutes with $\hat{V}$, there is no change in the occupation numbers over time.

The exponential of the interaction operator can be written out as the series expansion,

$$\begin{aligned} d\langle\hat{N}_k\rangle &= \langle\psi_i|\left(1-(1/i\hbar)\int_0^t \hat{V}(t')dt' + ...\right) \\ &\times\left((1/i\hbar)\int_0^t dt'[\hat{N}_k,\hat{V}(t')] + (1/i\hbar)^2\int_0^t dt'\int_0^{t'} dt''[\hat{N}_k,\hat{V}(t')\hat{V}(t'')] + ...\right)|\psi_i\rangle. \end{aligned} \tag{A.4}$$

By substituting $\hat{N}_k = a_k^\dagger a_k$ and Eq. (A.1) into this expansion, one get terms containing the matrix elements in the form of $\langle\psi_i|a_k^\dagger a_{k_3}^\dagger a_{k_2}a_{k_1}|\psi_i\rangle$, $\langle\psi_i|a_{k_1'}^\dagger a_{k_2'}^\dagger a_{k_3'}a_{k_4'}a_{k_1}^\dagger a_{k_2}^\dagger$ $a_{k_3}a_k|\psi_i\rangle$, $\cdots$, and so on. Among these matrix elements, the ones in which the creation operators fully undo the action of the destruction operators are called 'diangonal' elements, and the others are called 'off-diangonal' elements. For example, $\langle\psi_i|a_k^\dagger a_{k_3}^\dagger a_{k_2}a_{k_1}|\psi_i\rangle$ is a diagonal element when $k=k_2,\ k_3=k_1$ or $k=k_1,\ k_3=k_2$.

After carrying out the series expansion in Eq.(A.4) to the second order, the quantum Boltzmann equation can obtained by making the following approximations: (1) the off-diagonal elements in the expansion are negligible, (2) the time evolution is Markovian, and (3) there is no long-range correlation in the many-body wave function. The quantum Boltzmann equation is

$$\begin{aligned} \frac{d}{dt}\langle\hat{N}_k\rangle &= \frac{2\pi}{\hbar}\frac{1}{2}\sum_{k_1,k_2}(U_D \pm U_E)^2\delta(E_{k_1}+E_{k_2}-E_{k_3}-E_k) \\ &\times\Big(\langle\hat{N}_{k_1}\rangle\langle\hat{N}_{k_2}\rangle(1\pm\langle\hat{N}_{k_3}\rangle)(1\pm\langle\hat{N}_k\rangle) - \langle\hat{N}_k\rangle\langle\hat{N}_{k_3}\rangle(1\pm\langle\hat{N}_{k_2}\rangle)(1\pm\langle\hat{N}_{k_1}\rangle)\Big) \end{aligned} \tag{A.5}$$

where $\vec{k_3} = \vec{k_1} + \vec{k_2} - \vec{k}$.

The steady-state solution of this equation gives the particle number distribution at equilibrium. In equilibrium, we must have $dN(E_k)/dt = 0$ for all $\vec{k}$. This will occur if for all the different scattering processes, the forward and backward rates for any process are the same:

$$\begin{aligned} &N(E_{k_3})N(E_{k_2})(1\pm N(E_{k_1}))(1\pm N(E_k)) \\ &-N(E_k)N(E_{k_1})(1\pm N(E_{k_2})(1\pm N(E_{k_3}) = 0. \end{aligned} \tag{A.6}$$

This is the principle of detailed balance. It can easily be verified that a distribution of the form

$$N(E) = \frac{1}{e^{\alpha+\beta E} \mp 1} \tag{A.7}$$

satisfies this condition, where the $-$ sign is for bosons and the $+$ sign for fermions. The constants α and β are determined by the conditions

$$N = \sum_k N_k = \int N(E)\mathcal{D}(E)dE, \quad U = \sum_k E_k N_k = \int EN(E)\mathcal{D}(E)dE, \tag{A.8}$$

where $\mathcal{D}(E)$ is the density of k-states at energy E. These conditions follow from number and energy conservation, which follow from the fact that the total number operator N and the total energy operator U commute with the Hamiltonian. We can find α and β in terms of standard thermodynamic quantities by noting that if $\alpha \gg 1$, the equilibrium distribution is equal to $N(E) = e^{-\alpha}e^{-\beta E}$. Equating this to the standard equilibrium distribution $N(E) = e^{\mu/k_BT}e^{-E/k_BT}$, which is called the Maxwell-Boltzmann distribution, we then have $\beta = 1/k_BT$ and $\alpha = -\mu/k_BT$, or

$$N(E) = \frac{1}{e^{(E-\mu)/k_BT} \mp 1}, \tag{A.9}$$

which is the well-known equilibrium distribution for quantum particles; when the sign is negative it is called the Bose-Einstein distribution and when the sign is positive it is called the Fermi-Dirac distribution. The quantum Boltzmann equation is therefore another way of deducing the standard equilibrium distributions.

A.2 IRREVERSIBILITY IN QUANTUM BOLTZMANN EQUATION AND DEPHASING

A.2.1 Irreversibility in Quantum Boltzmann Equation

Starting from a non-equilibrium state, the quantum Boltzmann equation predicts that the system will evolve deterministically towards the equilibrium state and then maintain at that state. This prediction has been widely verified in experiments [135]. For example, *Snoke* et al. [136] showed that a population of excitons created by a ultrafast laser pulse in a

semiconductor rapidly evolved into a Maxwell-Boltzmann distribution. They found that the measured population dynamics fitted very well to the evolution given by the quantum Boltzmann equation.

But in a closed, energy-conserving system, we expect the dynamics will be time-reversible. In other words, if we start with state $|i\rangle$ and evolve to a state $|j\rangle$ at some later time, then we expect that if we started with the system in state $|j\rangle$, and reverse all the momenta, we should get back to state $|i\rangle$. So, why does the quantum Boltzmann equation tells us that the system will evolves deterministically to equilibrium? How have we gone from a time-reversible system to one with apparent irreversibility?

A close examination reveals that the irreversibility comes in when the off-diagonal terms are dropped off when we were deriving of the quantum Boltzmann equation [132]. In the derivation, we threw out terms of form

$$\rho^{(2)}_{k_1,k_2,k_3,k} \equiv \langle\psi_i|a^\dagger_{k_1}a^\dagger_{k_2}a_{k_3}a_k|\psi_i\rangle, \tag{A.10}$$

and

$$\rho^{(4)}_{k_1,k_2,k_3,k_4,k_5,k_6,k_7,k} \equiv \langle\psi_i|a^\dagger_{k_7}a^\dagger_{k_6}a_{k_5}a_{k_4}a^\dagger_{k_3}a^\dagger_{k_2}a_{k_1}a_k|\psi_i\rangle.$$

One way of speaking of this is to say that we keep only the "diagonal" information of the state of the system, and discard the "off-diagonal" information. This terminology is a generalization of the density matrix formalism, where the first-order density matrix of a quantum system is defined as (see Ref. [133], Section 9.2)

$$\rho = \begin{pmatrix} \langle a^\dagger_{k_1}a_{k_1}\rangle & \langle a^\dagger_{k_1}a_{k_2}\rangle & \langle a^\dagger_{k_1}a_{k_3}\rangle & \dots \\ \langle a^\dagger_{k_2}a_{k_1}\rangle & \langle a^\dagger_{k_2}a_{k_2}\rangle & \langle a^\dagger_{k_2}a_{k_3}\rangle & \dots \\ \langle a^\dagger_{k_3}a_{k_1}\rangle & \langle a^\dagger_{k_3}a_{k_2}\rangle & \langle a^\dagger_{k_3}a_{k_3}\rangle & \dots \\ . & & & \\ . & & & \\ . & & & \end{pmatrix} \tag{A.11}$$

The diagonal elements of this matrix are the average occupation numbers, while the off-diagonal terms account for phase correlations in the system. We can generalize to define as

"off-diagonal" any expectation values which do not involve only matched pairs of creation and destruction operators of the form $a_k^\dagger a_k$.

Suppose that the system starts in a purely diagonal state, with all off-diagonal terms of all orders strictly equal to zero. After a short time dt, while the quantum Boltzmann equation gives the correct value for the change of $\langle \hat{N}_k \rangle$, the state of the system will have evolved to a different superposition of Fock states, and therefore the off-diagonal terms may be nonzero. While in the derivation, we dropped all the off-diagonal terms. In this process, the information contained in the off-diagonal terms is lost. The loss of the off-diagonal information, known as "dephasing," ensures irreversibility.

On the other hand, if we did keep track of these terms, then we could write down the exact quantum mechanical state at time dt, and using this as an initial state, by reversing time we could recover the initial state at time $t = 0$.

A.3 CALCULATION OF THE OFF-DIAGONAL TIME EVOLUTION

As discussed above, the elimination of off-diagonal phase information leads to the irreversibility in the quantum calculation. Then, a natural question to ask is how valid an approximation it is to discard the phase information as we did in Section A.1. We can answer this question by computing the dephasing rate from the full quantum mechanical many-body wave function. In Section A.1, the evolution of $\langle \hat{N}_k \rangle$ depends, in principle, on the values of all of the different $\rho^{(2)}$ and $\rho^{(4)}$ terms. We note that the evolution of $\langle \hat{N}_k \rangle$ depends *only* on these terms, that is, on averages of the phase factors, and not on detailed knowledge of single values of the phase factors.

In the rest of this section, we show how to calculate the evolution of the off-diagonal phase terms. We will focus on the evolution of the $\rho^{(2)}$ terms, and return to discuss the $\rho^{(4)}$ and other terms at the end of this section. We define the operator $\hat{\rho}^{(2)}_{k,k',k'',k'''} = a_k^\dagger a_{k'}^\dagger a_{k''} a_{k'''}$, and assume that the four momenta are all different, because the case when two or more momenta are the same will be greatly suppressed due to the requirement of momentum conservation in the interaction Hamiltonian which gives rise to evolution of the $\rho^{(2)}$ terms.

Following a similar approach to that of Section A.1, we write for a given off-diagonal term,

$$\begin{aligned} d\langle\hat{\rho}^{(2)}_{k,k',k'',k'''}\rangle &= \langle\psi_t|\hat{\rho}^{(2)}_{k,k',k'',k'''}|\psi_t\rangle - \langle\psi_i|\hat{\rho}^{(2)}_{k,k',k'',k'''}|\psi_i\rangle \\ &= \langle\psi(t)|\hat{\rho}^{(2)}_{k,k',k'',k'''}(t)|\psi(t)\rangle - \langle\psi_i|\hat{\rho}^{(2)}_{k,k',k'',k'''}|\psi_i\rangle. \end{aligned} \tag{A.12}$$

As we did for (A.4), we expand the time-dependent exponential operators as

$$\begin{aligned} d\langle\hat{\rho}^{(2)}_{k,k',k'',k'''}\rangle &= \langle\psi_i|\left(1 - \frac{1}{i\hbar}\int_0^t \hat{V}(t')dt' + \frac{1}{(i\hbar)^2}\int_0^t dt'\int_0^{t'} dt''\hat{V}(t')\hat{V}(t'') + \dots\right)\hat{\rho}^{(2)}_{k,k',k'',k'''}(t) \\ &\times\left(1 + \frac{1}{i\hbar}\int_0^t \hat{V}(t')dt' + \frac{1}{(i\hbar)^2}\int_0^t dt'\int_0^{t'} dt''\hat{V}(t')\hat{V}(t'') + \dots\right)|\psi_i\rangle \\ &-\langle\psi_i|\hat{\rho}^{(2)}_{k,k',k'',k'''}|\psi_i\rangle. \end{aligned} \tag{A.13}$$

The lowest-order term is

$$\langle\psi_i|(\hat{\rho}^{(2)}_{k,k',k'',k'''}(t) - \hat{\rho}^{(2)}_{k,k',k'',k'''})|\psi_i\rangle; \tag{A.14}$$

the first-order terms are

$$\frac{1}{i\hbar}\int_0^t dt'\langle\psi_i|[\hat{\rho}^{(2)}_{k,k',k'',k'''}(t), \hat{V}(t')]|\psi_i\rangle; \tag{A.15}$$

while the second-order terms are

$$\begin{aligned} &\frac{1}{\hbar^2}\int_0^t dt'\int_0^t dt''\ \langle\psi_i|\hat{V}(t')\hat{\rho}^{(2)}_{k,k',k'',k'''}(t)\hat{V}(t'')|\psi_i\rangle \\ &-\frac{1}{\hbar^2}\int_0^t dt'\int_0^{t'} dt''\langle\psi_i|\hat{V}(t')\hat{V}(t'')\hat{\rho}^{(2)}_{k,k',k'',k'''}(t)|\psi_i\rangle \\ &-\frac{1}{\hbar^2}\int_0^t dt'\int_0^{t'} dt''\langle\psi_i|\hat{\rho}^{(2)}_{k,k',k'',k'''}(t)\hat{V}(t')\hat{V}(t'')|\psi_i\rangle. \end{aligned} \tag{A.16}$$

We cannot assume that $\hat{\rho}^{(2)}_{k,k',k'',k'''}$ commutes with H_0, as we did for N_k in the derivation of the quantum Boltzmann equation, so we must keep all of the $e^{iH_0t/\hbar}$ terms in the definitions of the time-dependent operators for the moment. In the following sections we compute each order of the expansion (A.13) separately.

A.3.1 Zero-Order Off-Diagonal Evolution

As before, we write $|\psi_i\rangle$ as a sum of Fock states $|\psi\rangle = \sum_n \alpha_n |n\rangle$, where $|n\rangle$ is a Fock state and α_n is the phase factor. Then the zero-order term is

$$d\langle\hat{\rho}^{(2)}_{k,k',k'',k'''}\rangle \;=\; \sum_{n,n'} \alpha^*_{n'}\alpha_n \left(\langle n'|(e^{iH_0t/\hbar}\hat{\rho}^{(2)}_{k,k',k'',k'''}e^{-iH_0t/\hbar}|n\rangle - \langle n'|\hat{\rho}^{(2)}_{k,k',k'',k'''})|n\rangle\right). \tag{A.17}$$

Applying the time-varying exponential factors to the Fock states gives us

$$\begin{aligned} d\langle\hat{\rho}^{(2)}_{k,k',k'',k'''}\rangle \;&=\; \sum_{n,n'} \alpha^*_{n'}\alpha_n (e^{i(E_k+E_{k'}-E_{k''}-E_{k'''})t/\hbar} - 1)\langle n'|\hat{\rho}^{(2)}_{k,k',k'',k'''}|n\rangle \\ &\simeq \frac{it}{\hbar}(E_k + E_{k'} - E_{k''} - E_{k'''}) \sum_{n,n'} \alpha^*_{n'}\alpha_n \langle n'|\hat{\rho}^{(2)}_{k,k',k'',k'''}|n\rangle \\ &= \frac{it}{\hbar}(E_k + E_{k'} - E_{k''} - E_{k'''})\langle\psi_i|\hat{\rho}^{(2)}_{k,k',k'',k'''}|\psi_i\rangle. \end{aligned} \tag{A.18}$$

Thus, if there are nonzero $\hat{\rho}^{(2)}$ terms, these will rotate in phase with angular frequency proportional to the degree of violation of energy conservation.

A.3.2 First-Order Off-Diagonal Evolution

We start by working on the first-order term. Inserting the definition of $\hat{V}$, we have

$$\begin{aligned} &\langle\psi_i|[\hat{\rho}^{(2)}_{k,k',k'',k'''}(t), \hat{V}(t')]|\psi_i\rangle = \\ &\quad \sum_{k_1,k_2,k_3} \frac{U}{2}\langle\psi_i|[e^{iH_0t}a^\dagger_k a^\dagger_{k'}a_{k''}a_{k'''}e^{-iH_0t}, e^{iH_0t'}a^\dagger_{k_4}a^\dagger_{k_3}a_{k_2}a_{k_1}e^{-iH_0t'}]|\psi_i\rangle, \end{aligned} \tag{A.19}$$

where we abbreviate the momentum-dependent matrix element simply as U. Agains, we write the initial state as a sum superposition of Fock state, then

$$\begin{aligned} &\langle\psi_i|[\hat{\rho}^{(2)}_{k,k',k'',k'''}(t), \hat{V}(t')]|\psi_i\rangle = \\ &\quad \sum_{n,n'} \alpha^*_{n'}\alpha_n \sum_{k_1,k_2,k_3} \frac{U}{2}(\langle n'|e^{iH_0t/\hbar}a^\dagger_k a^\dagger_{k'}a_{k''}a_{k'''}e^{-iH_0t/\hbar}e^{iH_0t'/\hbar}a^\dagger_{k_1}a^\dagger_{k_2}a_{k_3}a_{k_4}e^{-iH_0t'\hbar}|n\rangle \\ &\qquad -\langle n'|e^{iH_0t'/\hbar}a^\dagger_{k_1}a^\dagger_{k_2}a_{k_3}a_{k_4}e^{-iH_0t'/\hbar}e^{iH_0t/\hbar}a^\dagger_k a^\dagger_{k'}a_{k''}a_{k'''}e^{-iH_0t/\hbar}|n\rangle). \end{aligned} \tag{A.20}$$

For $n' = n$, this becomes

$$\sum_n |\alpha_n|^2 2(U_D \pm U_E) \Big(e^{i(E_k + E_{k'} - E_{k''} - E_{k'''})(t-t')/\hbar} N_k^{(n)} N_{k'}^{(n)} (1 \pm N_{k''}^{(n)})(1 \pm N_{k'''}^{(n)}) \\ - e^{-i(E_k + E_{k'} - E_{k''} - E_{k'''})(t-t')/\hbar} N_{k''}^{(n)} N_{k'''}^{(n)} (1 \pm N_k^{(n)})(1 \pm N_{k'}^{(n)}) \Big) , \tag{A.21}$$

where, as in Section A.1, U_D and U_E are the direct and exchange interaction constants, and the numbers $N_k^{(n)}$, $N_{k_1}^{(n)}$, etc., without hats, are the occupation numbers of the k-states in the Fock state $|n\rangle$. The $\pm$ signs here give the cases of bosons and fermions, as in the quantum Boltzmann equation. If $n' \neq n$, we are left with off-diagonal terms, either $\hat{\rho}^{(2)}$ or higher-order phase terms, namely a six-operator $\hat{\rho}^{(3)}$ term or an eight-operator $\rho^{(4)}$ phase term. We will discuss these below.

Performing a time integral for the case $n' = n$, we have

$$e^{i\omega t} \int_0^t dt' e^{-i\omega t'} \;=\; (1 + i\omega t + \ldots) \frac{1 - i\omega t + \ldots - 1}{-i\omega} \;\simeq\; t. \tag{A.22}$$

Thus, for a small time interval t, the first-order evolution from a diagonal state gives

$$\frac{d}{dt} \langle \hat{\rho}^{(2)}_{k,k',k'',k'''} \rangle = \tag{A.23}$$
$$\frac{2i}{\hbar} (U_D \pm U_E) \langle \psi_i | \left(\hat{N}_{k''} \hat{N}_{k'''} (1 \pm \hat{N}_k)(1 \pm \hat{N}_{k'}) - \hat{N}_k \hat{N}_{k'} (1 \pm \hat{N}_{k''})(1 \pm \hat{N}_{k'''}) | \psi_i \rangle \right) .$$

This term gives us phase coherence that accumulates proportional to the net scattering rate connecting the four states, but without any condition of energy conservation. This term will lead to a real change of the expectation value $\langle \hat{N}_k \rangle$ through the first order terms of Eq. (A.4). Since this term increases linearly with t, if the phase factors start out at zero value, the change in population in the first order terms of Eq. (A.4) will increase as t^2, which will be negligible on short time scales. But if the phase factors grow in time to have nonzero values, then they could contribute to the evolution of $\langle \hat{N}_k \rangle$.

As mentioned above, if we do not require $|n'\rangle = |n\rangle$ in equation (A.20), we will have terms with higher-order off-diagonal terms instead of just number operators $\hat{N}_k$. In this case we will have terms like the following:

$$\begin{aligned}&\langle n'|e^{iH_0t}a_k^\dagger a_{k'}^\dagger a_{k''}a_{k'''}e^{-iH_0t}e^{iH_0t'}a_{k_4}^\dagger a_{k_3}^\dagger a_{k_2}a_{k_1}e^{-iH_0t'}|n\rangle\\ -&\langle n'|e^{iH_0t'}a_{k_4}^\dagger a_{k_3}^\dagger a_{k_2}a_{k_1}e^{-iH_0t'}e^{iH_0t}a_k^\dagger a_{k'}^\dagger a_{k''}a_{k'''}e^{-iH_0t}|n\rangle.\end{aligned} \tag{A.24}$$

If none of the operators $a_{k_1}, a_{k_2}, a_{k_3}^\dagger$, or $a_{k_4}^\dagger$ act on the same k-states as the momenta in $\hat{\rho}^{(2)}_{k,k',k'',k'''}$, i.e., if all the operators in the interaction term commute with $\hat{\rho}^{(2)}_{k,k',k'',k'''}$, then these two terms will cancel.

To deal with the case when the interaction term does not commute with $\hat{\rho}^{(2)}_{k,k',k'',k'''}$, we must deal with a number of possibilities. The detailed calculation can be found in Appendix B of our paper [132]. The general result is that if there are nonzero $\rho^{(2)}$ factors, then these can contribute to the first-order evolution of $\hat{\rho}^{(2)}_{k,k',k'',k'''}$. These other $\rho^{(2)}$ off-diagonal factors always appear in sums, such as

$$\sum_{k_1,k_2} f(N_k, N_{k'}, N_{k''}, N_{k'''})\hat{\rho}^{(2)}_{k,k',k_1,k_2}, \tag{A.25}$$

where $f(N_k, N_{k'}, N_{k''}, N_{k'''})$ is some function of the occupation numbers, which can be either positive or negative. We might in general expect that these sums will average to zero, but as we will see below, even if they do not, there will be an overall evolution term to suppress these $\rho^{(2)}$ factors.

A.3.3 Second-Order Off-Diagonal Evolution

We now proceed to the second-order terms (A.16). First, we examine the time integrals. We assume that the operators in the first $\hat{V}(t')$ undo whatever changes have been done by $\hat{V}(t'')$; otherwise we will not be left with $\langle\psi_i|\hat{\rho}^{(2)}_{k,k',k'',k'''}|\psi_i\rangle$. Terms which do not do this will involve higher-order off-diagonal phase correlation terms $\hat{\rho}^{(3)}$, $\hat{\rho}^{(4)}$, etc. These terms in principle can contribute to a second-order contribution to the evolution of $\langle\psi_i|\hat{\rho}^{(2)}|\psi_i\rangle$, but as with the first-order calculation, we take a perturbative approach that the $\hat{\rho}^{(2)}$ terms will

dominate over higher-order off-diagonal terms. What we are interested in now is any terms proportional to $\langle\psi_i|\hat{\rho}^{(2)}|\psi_i\rangle$, so that we can see what happens to existing off-diagonal phase accumulation.

If $\hat{V}(t')$ undoes whatever changes have been done to $|\psi_i\rangle$ by $\hat{V}(t'')$, then each of the three terms in (A.16) gives a factor $e^{i(E_{k_1}+E_{k_2}-E_{k_3}-E_{k_4})t'/\hbar} \times e^{-i(E_{k_1}+E_{k_2}-E_{k_3}-E_{k_4})t''/\hbar}$, but in the first case t' and t'' are integrated from 0 to t separately, while in the last two terms t' is integrated from 0 to t but t'' is integrated from 0 to t'. The first case gives a factor $(2\pi t/\hbar)\delta(E_{k_1}+E_{k_2}-E_{k_3}-E_{k_4})$. The second case can be written as

$$\begin{aligned}\int_0^t dt' \int_0^{t'} dt''\ e^{i\omega t'} e^{-i\omega t''} &= \int_0^t dt' \int_0^t dt''\ e^{i\omega t'} e^{-i\omega t''} - \int_0^t dt' \int_{t'}^t dt''\ e^{i\omega t'} e^{-i\omega t''} \\ &= \int_0^t dt' \int_0^t dt''\ e^{i\omega(t'-t'')} - \int_0^t dt' \int_0^{t-t'} dt'''\ e^{-i\omega(t-t')} e^{i\omega t'''} \\ &= \int_0^t dt' \int_0^t dt''\ e^{i\omega t'} e^{-i\omega t''} - \int_0^t dt'''' \int_0^{t''''} dt'''\ e^{-i\omega t''''} e^{i\omega t'''}.\end{aligned} \tag{A.26}$$

The second term on the right in the last line is equal to the term on the left, and therefore we have

$$\begin{aligned}\int_0^t dt' \int_0^{t'} dt''\ e^{i\omega t'} e^{-i\omega t''} &= \frac{1}{2}\int_0^t dt' \int_0^t dt''\ e^{i\omega t'} e^{-i\omega t''} \\ &= \frac{\pi t}{\hbar}\delta(E_{k_1}+E_{k_2}-E_{k_3}-E_{k_4}),\end{aligned} \tag{A.27}$$

i.e., 1/2 of the first case.

For convenience we write one term of the $\hat{V}$ sum as $\hat{V}_i = U a^\dagger_{k_4} a^\dagger_{k_3} a_{k_2} a_{k_1}$. After removing the time dependence, the second order term of interest is

$$\langle\psi_i|\left(\hat{V}_{i'}\hat{\rho}^{(2)}\hat{V}_i - \tfrac{1}{2}\hat{V}_{i'}\hat{V}_i\hat{\rho}^{(2)} - \tfrac{1}{2}\hat{\rho}^{(2)}\hat{V}_{i'}\hat{V}_i\right)|\psi_i\rangle. \tag{A.28}$$

This is the generalized Lindblad operator for a many-body system, used often in quantum optics [137]. If $\hat{V}_i$ and $\hat{V}_{i'}$ both commute with $\rho^{(2)}$, then this vanishes. Thus, all of the terms in $\hat{V}$ which do not include a creation or destruction operator with at least one of the four momenta k, k', k'', k''' in $\hat{\rho}^{(2)}$ do not contribute to any change of this dephasing term. This

makes sense, since only interactions with these states should contribute to this dephasing term.

We must therefore consider each type of $\hat{V}_i$ term that does not commute with $\hat{\rho}^{(2)}_{k,k',k'',k'''}$. We will take these in order: terms with one momentum the same as in $\hat{\rho}^{(2)}_{k,k',k'',k'''}$, terms with two momenta the same as in $\hat{\rho}^{(2)}_{k,k',k'',k'''}$, terms with three the same, and terms with four the same.

The interaction term $\hat{V}_i$ will not commute with $\hat{\rho}^{(2)}_{k,k',k'',k'''}$ if one of the four operators in $\hat{V}_i$ acts on one of the same momenta as the four in $\hat{\rho}^{(2)}_{k,k',k'',k'''}$. We assume that $\hat{V}_{i'}$ has the same four operators as in $\hat{V}_i$, so that all the changes in $|\psi_i\rangle$ made by $\hat{V}_i$ are reversed, as discussed above. In this case, (A.28) will have terms like the following:

$$a^\dagger_k a^\dagger_k a_k - \frac{1}{2} a^\dagger_k a_k a^\dagger_k - \frac{1}{2} a^\dagger_k a^\dagger_k a_k = -\frac{1}{2} a^\dagger_k, \tag{A.29}$$

which is true for both bosons and fermions, using the fermion property that a double creation operator vanishes. The remaining operator in (A.29) goes back into the definition of $\rho^{(2)}$, leaving behind three operators in each of $\hat{V}_i$ and $\hat{V}_{i'}$.

Setting $\vec{k}_1 = \vec{k}$ in $\hat{V}_i$, we can pick the momenta in $\hat{V}_{i'}$ four different ways to restore the same Fock state:

$$\begin{aligned} &a^\dagger_k a^\dagger_{k_2} a_{k_3} a_{k_4} a^\dagger_{k_4} a^\dagger_{k_3} a_{k_2} a_k + a^\dagger_k a^\dagger_{k_2} a_{k_4} a_{k_3} a^\dagger_{k_4} a^\dagger_{k_3} a_{k_2} a_k \\ &+ a^\dagger_{k_2} a^\dagger_k a_{k_3} a_{k_4} a^\dagger_{k_4} a^\dagger_{k_3} a_{k_2} a_k + a^\dagger_{k_2} a^\dagger_k a_{k_4} a_{k_3} a^\dagger_{k_4} a^\dagger_{k_3} a_{k_2} a_k. \end{aligned} \tag{A.30}$$

If U is a constant, this just gives a factor of 4 multiplying the $(U/2)^2$ prefactor that comes from the two $\hat{V}$ terms in second order; more generally it gives the prefactor $\frac{1}{2} U_D (U_D \pm U_E)$. There will be another four terms giving $\pm \frac{1}{2} U_E (U_D \pm U_E)$ if we take $\vec{k}_2 = \vec{k}$, thus giving $(U_D \pm U_E)^2$, which is the same matrix element as in the quantum Boltzmann equation (A.5).

Setting $\vec{k}_3$ or $\vec{k}_4$ in $\hat{V}_i$ equal to k gives two more sets of four terms, using

$$a_k a^\dagger_k a^\dagger_k - \frac{1}{2} a_k a^\dagger_k a^\dagger_k - \frac{1}{2} a^\dagger_k a_k a^\dagger_k = \pm \frac{1}{2} a^\dagger_k. \tag{A.31}$$

where the $+$ is for bosons and the $-$ is for fermions.

Thus, for the momentum k in $\hat{\rho}^{(2)}_{k,k',k'',k'''}$, we have a factor of the form

$$\frac{1}{2}(U_D \pm U_E)^2 \left[\pm \hat{N}_{k_1}\hat{N}_{k_2}(1 \pm \hat{N}_{k_3}) - \hat{N}_{k_2}(1 \pm \hat{N}_{k_3})(1 \pm \hat{N}_{k_4})\right].$$

Since $\vec{k}_1, \vec{k}_2, \vec{k}_3$, and $\vec{k}_4$ are dummy variables, we can switch $\vec{k}_4$ with $\vec{k}_2$ and $\vec{k}_3$ with $\vec{k}_1$, without changing the matrix element. We thus finally have, for the second-order term,

$$\begin{aligned}\frac{d}{dt}\langle\hat{\rho}^{(2)}_{k,k',k'',k'''}\rangle &= \frac{2\pi}{\hbar}(U_D \pm U_E)^2 \, \frac{1}{2}\sum_{k_2,k_3}\delta(E_k + E_{k_2} - E_{k_3} - E_{k_4}) \\ &\quad \times\langle\psi_i|\hat{\rho}^{(2)}_{k,k',k'',k'''}\left[\pm\hat{N}_{k_3}\hat{N}_{k_4}(1 \pm \hat{N}_{k_2}) - \hat{N}_{k_2}(1 \pm \hat{N}_{k_3})(1 \pm \hat{N}_{k_4})\right]|\psi_i\rangle + \ldots.\end{aligned} \tag{A.32}$$

where the ... indicates that there are three more terms of exactly the same form, for k', k'', and k''' in $\hat{\rho}^{(2)}_{k,k',k'',k'''}$.

Under the assumption of no long-range correlations in the system, we can factorize (A.32) into products of expectation values. We then have

$$\begin{aligned}\frac{d}{dt}\langle\hat{\rho}^{(2)}_{k,k',k'',k'''}\rangle &= \langle\hat{\rho}^{(2)}_{k,k',k'',k'''}\rangle\frac{2\pi}{\hbar}(U_D \pm U_E)^2 \, \frac{1}{2}\sum_{k_2,k_3}\delta(E_k + E_{k_2} - E_{k_3} - E_{k_4}) \\ &\quad \times\left[\pm\langle\hat{N}_{k_3}\rangle\langle\hat{N}_{k_4}\rangle(1 \pm \langle\hat{N}_{k_2}\rangle) - \langle\hat{N}_{k_2}\rangle(1 \pm \langle\hat{N}_{k_3}\rangle)(1 \pm \langle\hat{N}_{k_4}\rangle)\right] + \ldots.\end{aligned} \tag{A.33}$$

The population factor $\langle\hat{N}_{k_3}\rangle\langle\hat{N}_{k_4}\rangle(1 \pm \langle\hat{N}_{k_2}\rangle) - \langle\hat{N}_{k_2}\rangle(1 \pm \langle\hat{N}_{k_3}\rangle)(1 \pm \langle\hat{N}_{k_4}\rangle)$ does not vanish in equilibrium, unlike the comparable term in the quantum Boltzmann equation, because it does not have the balancing factors $\langle\hat{N}_k\rangle$ and $(1 \pm \langle\hat{N}_k\rangle)$. For fermions, this rate is always negative, leading to dephasing, while for bosons, it can be positive if the net scattering rate into one of the k-states is positive. Net scattering into a state can occur, for example, when there is macroscopic coherence due to Bose condensation, which gives a macroscopic number of particles in a single state. The case of Bose condensation will be discussed in the next section. At low density or high temperature, however, when $\langle N_k\rangle \ll 1$, the out-scattering term in (A.32) will dominate over the in-scattering term, since the in-scattering involves a product of two occupation numbers, while the out-scattering term has only a single occupation number. In other words, at low occupation per state, given a particle in state k, it is much more likely for that particle to scatter out of that state than for another to enter, in a given time interval. Therefore at low density the overall rate is always negative.

A.3.4 Summary of Dephasing Calculation Results

We have seen that on the one hand, that (A.23) implies that scattering does lead to deviation from a pure diagonal state, with an increase of the phase factor $\langle\hat{\rho}^{(2)}\rangle$ proportional to the net scattering rate. But in the case of fermions, or bosons at low density, that phase coherence can never build up; the result (A.33) is of the form

$$\frac{d}{dt}\langle\hat{\rho}^{(2)}\rangle = -\frac{\langle\hat{\rho}^{(2)}\rangle}{\tau}, \tag{A.34}$$

which gives exponential decay of the phase with a time constant τ; the value of τ is equal to the time constant for out-scattering found from the quantum Boltzmann equation. Moreover, in the low density limit, the phase build-up will always be negligible compared to the phase decay on average, because the build-up rate (A.23) is proportional to the square of the occupation number, while the decay term (A.33) is linear in the occupation number at low density.

Turning to the $\rho^{(4)}$ terms, which we found can also contribute to the evolution of $\langle\hat{N}_k\rangle$, it should not be hard to see that the same procedure applied to these phase factors will give the same behavior. In the above calculation for the dephasing, we could have just as easily inserted $\rho^{(4)}$, with the same result, but with eight scattering terms instead of four. In the same way, a first-order calculation like the one which gave us the result (A.23) for the accumulation of phase, presumably will also give us a term linear in t, but this phase accumulation will quickly be removed by the dephasing.

We can therefore say in general terms that the natural evolution of the system makes the many-body states tend rapidly toward becoming diagonal states, which was the assumption used implicitly in the iterative solution of the quantum Boltzmann equation. In equilibrium, (A.23) implies that there is no build up of phase factors, and the states resolve to diagonal states, that is, states in which only $\langle\hat{N}_k\rangle$ is relevant. If the system is far from equilibrium, there will be a tiny buildup of phase in the superposition of states which is constantly being destroyed by the out-scattering processes.

APPENDIX B

INTENSITY STABILIZED TI:SAPPHIRE LASER WITH FEEDBACK FROM A GRATING

In the experiments discussed in Chapter 5, 6 and 7 a homemade continuous wave Ti:Sapphire laser was used to excite the microcavity. Fig. 58(a) is a schematic of the layout of this laser, and Fig. 58(b) is a photo of this laser. The pump laser is a 5 W Verdi G Series semiconductor laser from Coherent. It delivers 5 W of power at 532 nm. The output beam (green line) of the pump laser is linearly polarized in the vertical direction. In order to maximize the transmission of the pump beam into the Ti:Sapphire crystal, the polarization of this beam is rotated into the horizontal direction by a half-wave plate (HWP). A plano-convex lens (L1) is used to focus the pump beam into the Ti:Sapphire crystal through a dichroic concave mirror (M2). This mirror and the other concave mirror M3 are identical, and are both from LAYERTEC. They have anti-reflection coatings on their back surfaces for 532 nm which give $< 0.25\%$ of reflection for the pump beam. Their front surfaces have a reflectivity larger than 99.8% for wavelengths in the range from 640 nm to 1000 nm. These two mirrors (M2 and M3) together with an end mirror (M4) and an output coupler (OC) form the cavity of the laser. The end mirror is a dielectric mirror which has nearly perfect reflectivity for wavelength in the range from 640 nm to 1000 nm. The output coupler transmits about 5% of the light incident on to it. The transmitted light is the output of the laser cavity. A birefringent filter (BRF) is placed into the beam path inside the cavity for the purpose of tuning the wavelength of the laser. The BRF introduces wavelength dependent polaritzation change of the cavity modes that transmit through it. As the polarization of the light is

changed, the transmission lose of the light in the cavity is also changed. The one that has minimum transmission loss becomes the dominate mode in the cavity. Therefore, a particular wavelength is selected. By rotating the BRF, the wavelength of the minimum loss mode is changed so does the wavelength of the output beam. In our laser (Fig. 58(b)), the wavelength can be tuned from about 720 nm to 900 nm. The output power at 730 nm is about 500 mW when the cavity is pumped by a 5 W beam from the pump laser.

The cavity length is minimized in order to increase the free spectral range of the laser, and therefore to reduce the mode-hopping in the laser. The cavity length of this laser is 45 cm, which gives a free spectral range of 330 MHz. By comparison, the cavity length of the Mirra from Coherent Inc. is about 200 cm, which gives a free spectral range of 76 MHz. Fig. 58(c) is the measured output intensities of the homemade laser at 733 nm. The output intensity of the homemade laser is oscillating at a frequency of 330 MHz with an amplitude of 30% of its average power. The frequency of this oscillation equals to the free spectral range of the laser, which indicates that this oscillation comes from the beating between adjacent modes in the laser cavity. By comparison, the output intensity of the Mirra laser, as shown in Fig. 58(d) is oscillating at multiple frequencies with an amplitude of 50% of its average power.

As discussed in Section 5.2.1, the fluctuation of the output intensity seen in Fig. 58(c) can be reduced by using a grating to feed part of output beam back into the laser cavity. In this case, a 1200 grooves/mm ruled diffraction grating is installed right after the output coupler (OC) of the laser cavity. This grating is set into the Littrow configuration (Fig. 59(a)) with respect to the beam coming from the laser. As shown in Fig. 59(a), the incident beam comes in along the normal direction of the grating grooves, the 1st-order diffraction of the grating is collinear and antiparallel to the incident beam. The zero-order diffraction of the grating is the final output of the laser. The spectrally-narrow 1st-order beam will go back into the cavity, to stimulate the cavity to lase at the its particular wavelength, and therefore eliminate other modes in the laser cavity.Fig. 59(b) is an image of the laser with the grating installed. The time dependence of the output intensity of the laser with grating feedback is shown in Fig. 59(c). Comparing to Fig. 58(c), the stability of the laser output has greatly improved.

However, a major disadvantage of doing grating feedback is that the output power re-

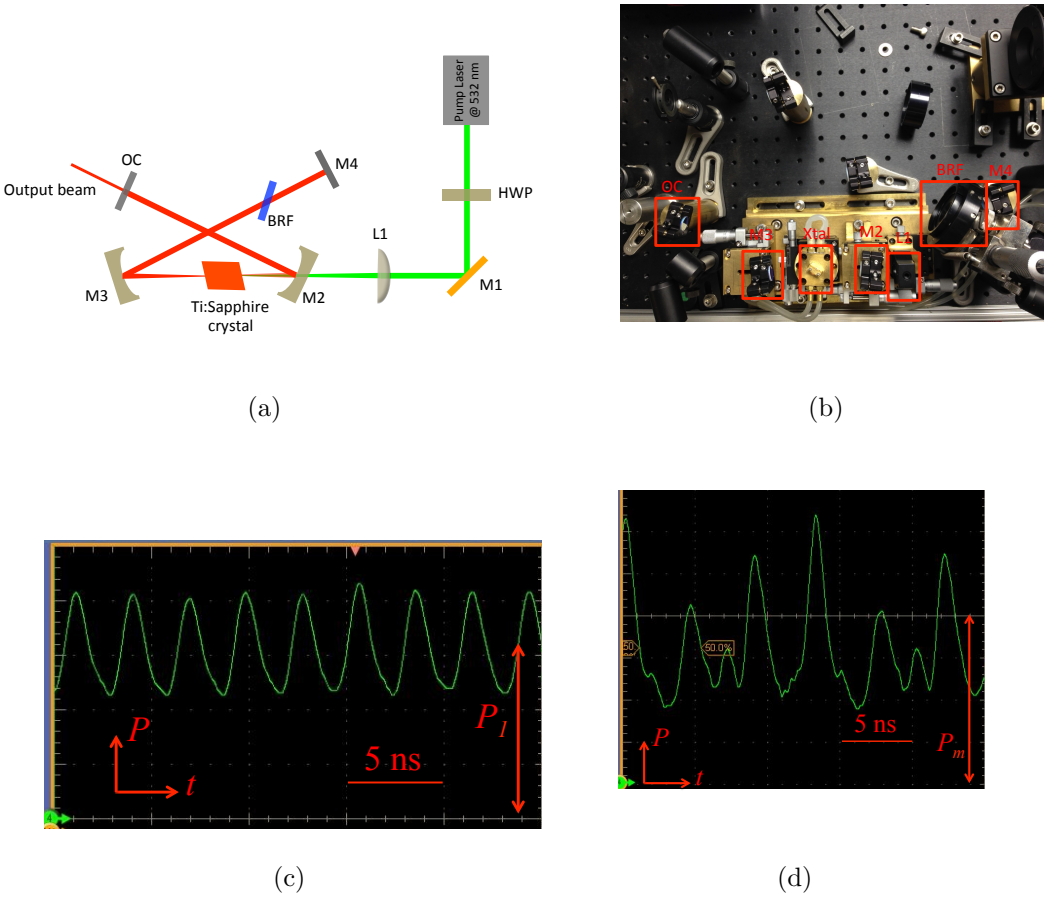

(a) (b)

(c) (d)

Figure 58: (a) Schematic of the Ti:Sapphire laser. (b) A photo of the homemade Ti:Sapphire laser. The components that corresponding to the drawings in (a) are enclosed by red rectangles. Xtal represents the Ti:Sapphire crystal. (c) Time dependence of the output power of the homemade laser at 733 nm. (d) Time dependence of the output power of the Mirra laser (P_m) from the Coherent Inc. at 733 nm.

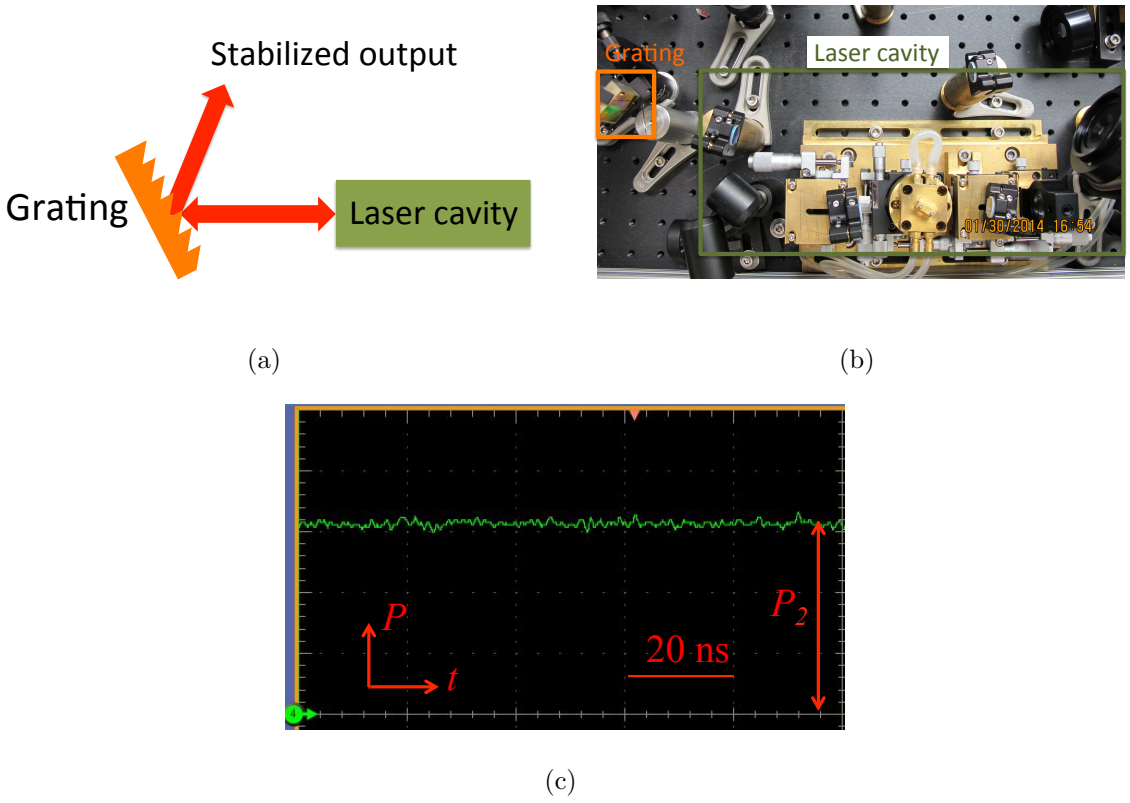

Figure 59: (a) Schematic of the Littrow configuration of grating feedback. (b) Image of the homemade Ti:Sapphire laser with a grating after the output coupler. (c) Output intensity of the laser at 733 nm after adding the grating feedback.

duced to only about 1/3 of that without grating feedback: the output power reduces to about 150 mW from 500 mW at 730 nm when the grating feedback was used. In our experiment, we found that having more pump power is more important than having very stable pump power. Therefore, in our experiments presented in Chapter 5, 6 and 7, the grating feedback was not used.

APPENDIX C

NUMERICAL METHOD OF RETRIEVING THE PHASE OF RING CONDENSATE FROM INTERFERENCE PATTERN

As mentioned in Section 6.1, one can extract the phase information of the ring condensate from the interference pattern with a method called digital off-axis holography [107, 108]. The procedure that I used to generate the phase map of the ring condensate (Fig. 43) from the interference pattern is illustrated in Fig. 60. A 2D fast Fourier transformation (FFT) was first applied to the interference pattern in Fig. 60(a). The image it generates is shown in Fig. 60(b), where the peak centers at the ($k_x = 0\ \mu\mathrm{m}^{-1}, \mathrm{k_y} = 0\ \mu\mathrm{m}^{-1}$) corresponds to the uniform background of the interference pattern which comes from the incoherent polaritons. The peaks at ($k_x = \pm 0.91\ \mu\mathrm{m}^{-1}, \mathrm{k_y} = 0\ \mu\mathrm{m}^{-1}$) correspond to the fringes in Fig. 60(a) which comes from the coherent polaritons. The distances from these two peaks to the origin of the reciprocal space is the in-plane component of the wave vector of the PL. These two frequency components are conjugate of each other; they carris the same information about the interference pattern. One can choose either one them for retrieving the phase information of the ring condensate. The effect of the in-plane wave vector is removed by shifting the chosen peak to the center of the reciprocal space (Fig. 60(b)). For example, in Fig. 60(c) the peak at $k_x = 0.91\ \mu\mathrm{m}^{-1}$ in Fig. 60(b) has been selected and shifted to ($k_x = 0\ \mu\mathrm{m}^{-1}, \mathrm{k_y} = 0\ \mu\mathrm{m}^{-1}$). Then a 2D inverse FFT is applied to Fig. 60(c) which generates the phase map shown in Fig. 60(d). This phase map shows the phase gradient of the interference pattern in Fig. 60(a), which is twice the phase gradient of the ring condensate. Therefore, in the ring condensate, there is a π phase shift when going around a closed loop in it.

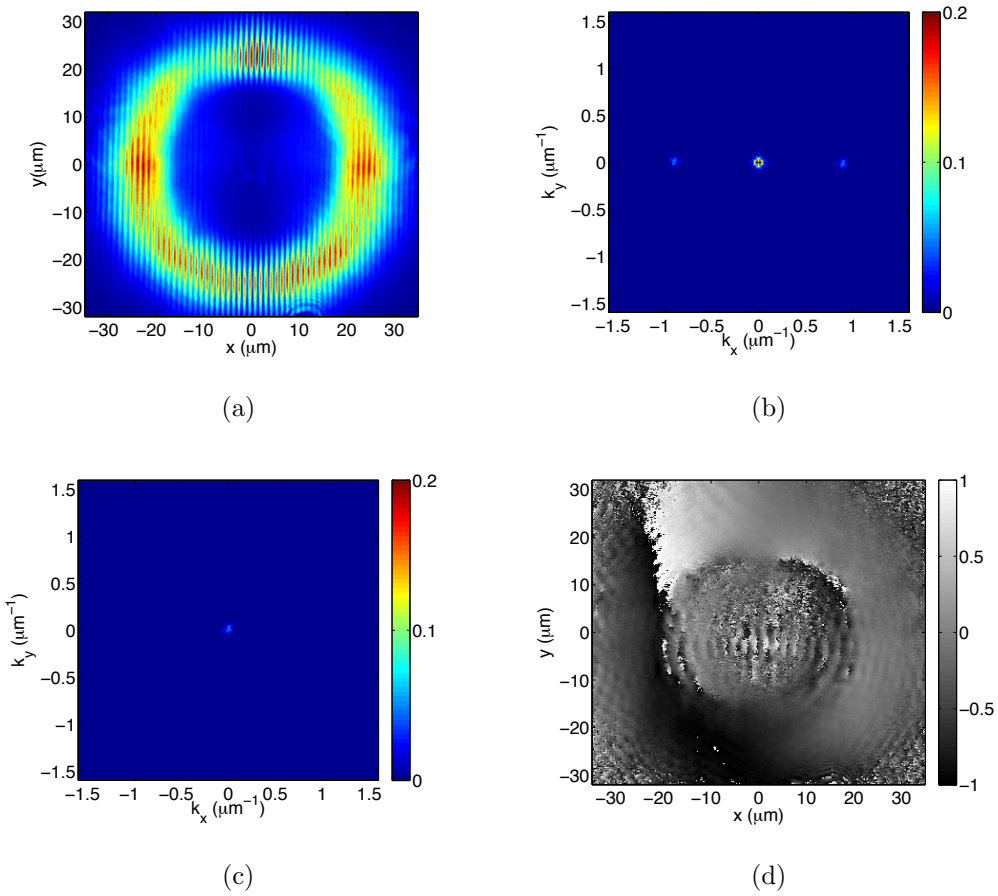

Figure 60: (a) Real-space image of a typical interference pattern of the ring condensate. (b) Fourier transformation of the interference pattern in (a). (c) The positive frequency component in (b) is selected and shifted to the center of the reciprocal space. (c) The phase map of (a) obtained by applying an inverse Fourier transformation of (c).

BIBLIOGRAPHY

[1] A. Einstein, Stizungsber. Press. Akad. Wiss. Phys. Math. Kl. **22**, 261 (1925).

[2] J. Bardeen, L. N. Cooper and J. R. Schrieffer, "Microscopic theory of superconductivity," Phys. Rev. **106 (1)**, 162-164 (1957).

[3] J. Bardeen, L. N. Cooper and J. R. Schrieffer, "Theory of superconductivity," Phys. Rev. **108(5)**, 1175-1204 (1957).

[4] P. Kapitza, "Viscosity of Liquid Helium below the λ-point," Nature **141**, 74 (1938).

[5] J. F. Allen and A. D. Misener, "Flow of Liquid Helium II," Nature **141**, 75 (1938).

[6] F. London, "The λ-phenomenon of liquid helium and the Bose-Einstein degeneracy," Nature **141**, 643 (1938).

[7] D. W. Snoke, J. P. Wolfe, and A. Mysyrowicz, "Evidence for Bose-Einstein condensation of excitons in Cu_2O," Phys. Rev. B **41**, 11171 (1990)

[8] J. L. Lin and J. P. Wolfe, "Bose-Einstein condensation of paraexcitons in stressed Cu_2O," Phys. Rev. Lett. **71**, 1222 (1993).

[9] T. Goto, M. Y. Shen, S. Koyama, and T. Yokouchi, "Bose-Einstein statistics of orthoexcitons generated by two-photon resonant absorption in cuprous oxide," Phys. Rev. B **55**, 7609 (1997).

[10] M. Y. Shen, T. Yokouchi, S. Koyanma, and T. Goto, "Dynamics associated with Bose-Einstein statistics of orthoexcitons generated by resonant excitons in cuprous oxide," Phys. Rev. B **56**, 13066 (1997).

[11] L. V. Butov et al., "Condensation of indirect excitons in coupled AlAs/GaAs quantum wells," Phys. Rev. Lett. **73**, 304 (1994).

[12] L. V. Butov, A. C. Gossard and D. S. Chemla, "Macroscopically ordered state in an exciton system," Nature **418**, 754 (2002)

[13] H. Deng et al., "Condensation of semiconductor microcavity exciton polaritons", Science **298**, 199 (2002).

[14] M. Richard et al., "Experimental evidence for non-equilibrium Bose condensation of exciton polaritons," Phys. Rev. B **72**, 201301(R) (2005).

[15] J. Kasprzak et al., "Bose-Einstein condensation of excition polaritons," Nature **443**, 409 (2006).

[16] S. Christopoulos et al., "Room-temperature polariton lasing in semiconductor microcavities," Phys. Rev. Lett. **98**, 126405 (2007).

[17] R. Balili et al., "Bose-Einstein condensation of microcavity polaritons in a trap," Science **316**, 1007 (2007).

[18] J. J. Hopfield, "Theory of the contribution of exciton to the complex dielectric constant of crystals," Phys. Rev. **112**, 1555 (1958).

[19] C. Weisbuch et al., "Observation of the coupled exciton-photon mode splitting in a semiconductor quantum microcavity," Phys. Rev. Lett. **69**, 3314 (1992).

[20] G. Tosi et al., "Sculpting oscillators with light within a nonlinear quantum fluid," Nature Physics **8**, 190-194 (2012).

[21] A. Askitopoulos et al., "Polariton condensation in an optically induced two-dimensional potential," Phys. Rev. **B** 88, 041308(R) (2013).

[22] B. Nelsen et al., "Dissipationless flow and sharp threshold of polariton condensate with long lifetime," Phys. Rev. X **3**, 041015 (2013).

[23] G. Liu, D. W. Snoke, A. Daley, L. N. Pfeiffer, and K. West, "A new type of half-quantum circulation in a macroscopic polariton spinor ring condensate," Proc. Nat. Acad. Sci. **112**, 2676 (2015).

[24] E. Wertz et al, "Spontaneous formation and optical manipulation of extended polariton condensate," Nat. Phys. **6**, 860 (2010).

[25] H. Deng et al., "Quantum degenerate exciton-polaritons in thermal equilibrium," Phys. Rev. Lett. **97**, 146402 (2006).

[26] K. G. Lagoudakis et al., "Quantized vortices in an exciton-polariton condensate", Nature Physics **4**, 706 (2008).

[27] A. Amo et al., "Collective fluid dynamics of a polariton condensate in a semiconductor microcavity", Nature **457**, 291 (2009).

[28] A. Amo et al., "Superfluidity of polaritons in semiconductor microcavities", Nature Physics **5**, 805 (2009).

[29] K. G. Lagoudakis et al., "Observation of half-vortices in an exciton-polariton condensate", Science **4**, 706 (2008).

[30] Utsunomiya et. al., "Observation of Bogoliubov excitations in exciton-polariton condensates", Nat. Phys. **4**, 700 (2008).

[31] D. Sanvitto et al., "Persistent currents and quantized vortices in a polariton superfluid", Nature Physcs **6**, 527 (2010).

[32] D. Sanvitto, "All-optical control of the quantum flow of a polariton condensate", Nature Photonics **5** 610-614 (2011).

[33] G. Roumpos et al., "Single vortex-antivortex pair in an exciton-polariton condensate", Nature Physics **7**, 129 (2011).

[34] A. Amo, "Polariton superfluids reveal quantum hydrodynamic solitons", Science **332** (6034), 1167-1170 (2011).

[35] F. Manni, Y Leger, Y. G. Rubo, R. Andre, B. Deveaud, "Hyperbolic spin vortices and textures in exciton-polariton condensates", Nat. Commun. 4, 2590 (2013).

[36] G. H. Wannier, "The structure of electronic excitation levels in insulating crystals", Physical Review **52**, 191 (1937).

[37] N. F. Mott, "Conduction in polar crystals. II. The conduction band and ultra-violet absorption of alkali-halide crystals", Trans. Faraday Soc. 34:500

[38] A. V. Kavokin, J. J. Baumberg, G. Malpuech and F. P. Laussy, *Microcavities*, 2007 Oxford University Press.

[39] D. Snoke, *Solid State Physics: Essential Concepts*, 2009 Pearson Education.

[40] S. Chuang, *Physics of Electronic Devices*, Wiley (1995).

[41] G. Bastard, E. E. Mendez, L. L. Chang, and L. Esaki, "Exciton binding energy in quantum wells", Phys. Rev. B **26**, 1974 (1982).

[42] S. Tarucha, H. Okamoto, Y. Iwasa and N. Miura, "Exciton binding energy in GaAs quantum wells deduced from magneto-optical absorption measurement", Solid State Comm. **52** (9), 815 (1984)

[43] W. Ossau et al., "Magneto-optical determination of the exciton binding energy in GaAs quantum wells", Surf. Sci. **174**, 188 (1986).

[44] R. Balili, *Bose-Einstein condensation of microcavity polaritons*, Thesis, University of Pittsburgh, 2009.

[45] V. E. Hartwell and D. W. Snoke, "Numerical simulations of the polariton kinetic energy distribution in GaAs quantum-well microcavity structures", Physical Review B **82**, 075307 (2010).

[46] P. Wen, "Phase diagram of Bose condensation of long-lifetime polaritons in equilibrium," **unpublised**.

[47] M. Wouters and I. Carusotto, "Excitations in non-equilibrium Bose-Einstein condensate of exciton polaritons", Phys. Rev. Lett. **99**, 140402 (2007).

[48] M. Steger et al, "Long-range ballistic motion and coherent flow of long-lifetime polaritons", Phys. Rev. B **88**, 235314 (2013).

[49] M. Steger et al, "Slow reflection and two-photon generation of microcavity excitonpolaritons", Optica **2**(1), 1 (2015).

[50] A. Einstein, Stizungsber. Press. Akad. Wiss. Phys. Math. Kl. **22**, 261 (1924).

[51] S. N. Bose, "Plank's law and the hypothesis of light quanta", Zeitschrift fur Physik **26**, 178 (1924).

[52] L. Pitaevskii and S. Stringari, *Bose-Einstein Condensation*, 2003.

[53] P. C. Hohenberg, "Existence of long-range order in one and two dimensions", Phys. Rev. **158**, 383 (1967)

[54] W. J. Mullin, "Bose-Einstein condensation in a harmonic potential", J. Low Temp. Phys. **106(5-6)**, 615 (1997).

[55] D. S. Petrov, M. Holzmann, and G. V. Shlyapnikov, "Bose-Einstein condensation in quasi-2D trapped gases", Phys. Rev. Lett. **84**, 2551 (2000).

[56] U. R. Fischer, "Existence of long-range order for trapped interacting bosons", Phys. Rev. Lett. **89**, 280402 (2002)

[57] U. R. Fischer, "Maximum length of trapped one-dimensional Bose-Einstein condensates", J. Low Temp. Phys. **138**, 723 (2005).

[58] A. Posazhennikova, "Colloquium: Weakly interacting, dilute Bose gases in 2D", Rev. Mod. Phys. **78**, 1111 (2006).

[59] C. Lai et. al, "Coherent zero-state and -state in an excitonpolariton condensate array", Nature **450**, 529 (2007)

[60] M. Maragkou et al., "Spontaneous nonground state polariton condensation in pillar microcavites", Phys. Rev. B **81**, 081308(R) (2010).

[61] W. Ketterle, "Nobel lecture: When atoms behave as waves: Bose-Einstein condensation and the atom laser," Rev. Mod. Phys., **74**(4), 1131 (2002).

[62] F. Dalfovo et al, "Theory of Bose-Einstein condensation in trapped gases", Rev. Mod. Phys. **71(3)** 463 (1999).

[63] A. Leggett, "Bose-Einstein condensation in the alkali gases: Some fundamental concepts", Rev. Mod. Phys. **73(2)**, 307 (2001).

[64] W. Ketterle, D. S. Durfee, D. M. Stamper-Kurn, "Making, probing and understanding Bose-Einstein condensates", arXiv:cond-mat/9904034.

[65] H. Deng, H. Huang and Y. Yamamoto, "Exciton-polariton Bose-Einstein condensation," Rev. Mod. Phys. **82**, No. 2, 2010.

[66] I. Carusoto and C. Ciuti, "Quantum fluids of light," Rev. Mod. Phys. **85**, 299 (2013).

[67] O. L. Berman, Y. E. Lozovik and D. Snoke, "Theory of Bose-Einstein condensation and superfluidity of two-dimensional polaritons in an in-plane harmonic potential", Phys. Rev. B **77**, 155317 (2008).

[68] D.W. Snoke, J.P. Wolfe, "Population dynamics of a Bose gas near saturation," Phys. Rev. B **39** 4030 (1989).

[69] F. C. Frank, and J. H. van der Merwe, "One-dimensional dislocations. I. Static theory," Proc. Roy. Soc. (London) A **198(1053)**, 216 (1949).

[70] F. C. Frank, and J. H. van der Merwe, "One-dimensional dislocations. II. Misfitting monolayers and oriented overgrowth," Proc. Roy. Soc. (London) A **198(1053)**, 216 (1949).

[71] J. W. Matthews, and A. E. Blakeslee, "Defects in Epitaxial multilayers I. Misfit dislocations", Journal of Crystal Growth **27**, 118 (1974).

[72] K. G. Lagoudakis, B. Pietka, M. Wouters, R. André and B. Deveaud-Plédran, "Coherent oscillations in an exciton-polariton Josephson junction", Phys. Rev. Lett. **105**, 120403 (2010).

[73] R. S. Markiewicz, J. P. Wolfe and C. D. Jeffries, "Strain-confined electron-hole liquid in germanium", Phys. Rev. B **15**, 1988 (1977).

[74] P. L. Gourley and J. P. Wolfe, "Thermodynamics of excitonic molecules in silicon," Phys. Rev. B **20** 3319 (1979).

[75] D. P. Trauernicht, J. P. Wolf and A. Mysyrowicz, "Thermodynamics of strain-confined paraexcitons in Cu_2O," Phys. Rev. B **34**, 2561 (1986).

[76] V. Negoita, D. W. Snoke and K. Eberl, "Stretching quantum wells: A method for trapping free carriers in GaAs heterostructures", App. Phys. Lett. **75**, 2059 (1999).

[77] G. L. Bir, and G. E. Pikus, *Symmetry and Strain Induced Effects in Semiconductors*, Wiley, New York, 1974.

[78] Landolt-Bòrnstein, *Numerical Data and Function Relationships in Science and Technology*, edited by O. Madelung and M. Schulz (Springer, Berlin, 1987), Vol. III. 22a.

[79] J. S. Blakemore, "Semiconductor and major properties of gallium arsenide," J. of App. Phys. **53(10)**, R123 (1982).

[80] R. Cottam and G. Saunders, J. Phys. C: Solid State Physics **6**, 2015 (1973).

[81] R. Balili et al., "Huge splitting of polariton states in microcavities under stress", Phys. Rev. B **81**, 125311 (2010).

[82] N.W. Sinclair et al., "Strain-induced darkening of trapped excitons in coupled quantum wells at low temperature," Phys. Rev. B **83**, 245304 (2011).

[83] G. Christmann et al., "Polariton ring condensate and sunflower ripples in an expanding quantum liquid", Phys. Rev. B **85**, 235303 (2012).

[84] M. Wouters, I. Carusotto, and C. Ciuti, "Spatial and spectral shape of inhomogeneous nonequilibrium exciton-polariton condensate", Phys. Rev. B **77**, 115340 (2008).

[85] P. Cristofolini et al., "Optical superfluid phase transitions and trapping of polariton condensates", Phys. Rev. Lett. 110, 186403 (2013).

[86] J. Kasprzak, Ph.D thesis, University of Joseph Fourier, 2006.

[87] C. Ryu, P. W. Blackburn, A. A. Blinova, M. G. Boshier, "Experimental realization of Josephson junctions for an atom SQUID", Phys. Rev. Lett. **111**, 205301 (2013).

[88] C. Ryu, et al., "Observation of persistent flow of a Bose-Einstein condensate in a toroidal trap", Phys. Rev. Lett. **99**, 260401 (2007).

[89] M. F. Andersen, et al., "Quantized rotation of atoms from photons with orbital angular momentum", Phys. Rev. Lett. **97**, 170406 (2006).

[90] A. Ramanathan, et al., "Superflow in a toroidal Bose-Einstein condensate: An atom circuit with a tunable weak link", Phys. Rev. Lett. **106**, 130401 (2011).

[91] K. C. Wright, R. B. Blakestad, C. J. Lobb, W. D. Phillips, G. K. Campbell, "Driving phase slips in a superfluid atom circuit with a rotating weak link", Phys. Rev. Lett. **110**, 025302 (2013).

[92] S. Beattie, S. Moulder, R. J. Fletcher, Z. Hadzibabic, "Persistent currents in spinor condensates", Phys. Rev. Lett. **110**, 025301 (2013).

[93] D. W. Hallwood, K. Burnett K, J. Dunningham, "Macroscopic superpositions of superfluid flows", New. J. Phys. **8**, 180 (2006).

[94] R. Kanamoto, et al., "Quantum superpositions of flow states on a ring", J. Opt. **13**, 064011 (2011).

[95] S. Eckel et al, "Hysteresis in a quantized superfluid atomtronic circuit", Nature **506**, 200 (2014)

[96] F. Manni, K. G. Lagoudakis, T. C. H. Liew, R. André and B. Deveaud-Plédran, "Spontaneous pattern formation in a polariton condensate", Phys. Rev. Lett. **107**, 106401 (2011).

[97] A. Dreismann et al., "Coupled counterrotating polariton condensates in optically defined annular potentials", Proc. Nat. Acad. Sci. U. S. A. **111** (24), 8770 (2014).

[98] V. K. Kalevich, et al., "Controllable structuring of exciton-polariton condensates in cylindrical pillar microcavities", Phys. Rev. B **91**, 045305 (2015).

[99] T. C. H. Liew, A. V. Kavokin, I. A. Shelykh, "Optical circuits based on polariton neurons in semiconductor microcavities", Phys. Rev. Lett. **101**, 016402 (2008).

[100] A. Amo, et al., "Exciton-polariton spin switch", Nat. Photonics **4**(6), 361 (2010).

[101] T. Gao, et al, "Polariton condensate transistor switch", Phys. Rev. B. **85**, 235102 (2012).

[102] G. Franchetti, N. G. Berloff, J. J. Baumberg, "Exploring quantum coherence of polaritons for ultra sensitive dectectors," arXiv:1210.1187 (2012).

[103] H. Cao et al., "Transition from a microcavity exciton polariton to a photon laser", Phys. Rev. A **55**, 4632 (1997).

[104] R. Butte et al., "Transition from strong to weak coupling and the onset of lasing in semiconductor microcavities", Phys. Rev. B **65**, 205310 (2012).

[105] A. Love et al., "Intrinsic Decoherence Mechanisms in the Microcavity Polariton Condensate", Phys. Rev. Lett. **101**, 067404 (2008).

[106] L. Ricci et al., "A compact grating-stabilized diode laser system for atomic physics", Opt. Comm. **117**, 541-549 (1995).

[107] T. Kreis, "Handbook of holographic interferometry: optical and digital methods," Wiley-VCH, 2004.

[108] Geal Nardin, "Phase-resolved imaging of exciton polaritons," Thesis, EPFL 2011.

[109] S. Sinha, R. Nath, and L. Santos, "Trapped two-dimensional condensates with synthetic spin-orbital coupling", Phys. Rev. Lett. **107**, 270401 (2011).

[110] M. Machida, T. Koyama, M. Kato, and T. Ishida, "Electronic structure of a half vortex", Physica C Supercond **412** (pt 1), 367 (2004).

[111] Y. G. Rubo, "Half vortices in exciton polariton condensates", Phys. Rev. Lett. **99**, 106401 (2007).

[112] F. P. Laussy, I. A. Shelykh, G. Malpuech, and A. Kavokin, "Effects of Bos-Einstein condensation of exciton polaritons in microcavities in the polarization of emitted light", Phys. Rev. B. **73**, 035315 (2006).

[113] I. A. Shelykh, Y. G. Rubo, G. Malpuech, D. D. Solnyshkov, and A. Kavokin, "Polarization and propagation of polariton condensates," Phys. Rev. Lett. **97**, 066402 (2006).

[114] G. Roumps et al., "Singnature of the microcavity exciton-polariton relaxation mechanism in the polarization of emitted light," Phys. Rev. B **79**, 195310 (2009).

[115] C. Ciuti, V. Savona, C. Piermarocchi, A. Quattropani, and P. Schwendimann, "Role of the exchange of carriers in elastic exciton-exciton scattering in quantum wells," Phys. Rev. B **58**, 7926 (1998).

[116] D. D. Solnyshkov, et al, "Nonlinear effects in spin relaxation of cavity polaritons," Semiconductors **41**(9), 1080-1091 (2007).

[117] Tassone, F., and Y. Yamamoto, "Exciton-exciton scattering dynamics in a semiconductor microcavity and stimulated scattering into polaritons," Phys. Rev. B **59**(16), 10830 (1999).

[118] M. I. Dyakonov, V. I. Perel', "Current-induced spin orientation of electrons in semiconductors," Phys. Lett. **35A**, 459 (1971).

[119] J. E. Hirsch et al., "Spin Hall effect," Phys. Rev. Lett. **83**, 1834 (1999).

[120] S. Murakami et al., "Dissipationless quantum spin current at room temperature," Science **301**, 1348 (2003).

[121] J. Sinova et al., "Universal intrinsic spin Hall effect," Phys. Rev. Lett. **92**, 126603 (2004).

[122] A. Kavokin et al., "Optical spin Hall effect," Phys. Rev. Lett. **95**, 136601 (2005).

[123] C. Leyder et al., "Observation of the optical spin Hall effect", Nature Phys. **3**, 628 (2007).

[124] M. Maragkou et al., "Optical analogue of the spin Hall effect in a photonic cavity," Opt. Lett. **36(7)**, 1095 (2011).

[125] E. Kammann et al., "Nonlinear optical spin Hall effect and long-range spin transport in polariton lasers," Phys. Rev. Lett. **109**, 036404 (2012)

[126] W. Langbein et al., "Elastic scattering dynamics of cavity polariton: evidence for time-energy uncertainty and polariton localization," Rev. Lett. **88**, 047401 (2002).

[127] M. D. Martin, "Polarization control of the nonlinear emission of semiconductor microcavities," Phys. Rev. Lett. **89**, 77402 (2002).

[128] I. Shelykh et al., "Semiconductor microcavity as a spin-dependent optoelectronic device", Phys. Rev. B **70**, 035320 (2004)

[129] G. Panzarini et al., "Exciton-light coupling in single and coupled semiconductor microcavities: Polariton dispersion and polarization splitting", Phys. Rev. B **59**, 5082 (1999).

[130] G. Christmann et. al., "Polariton ring condensates and sunflower ripples in an expanding quantum liquid," Phys. Rev. B **85**, 235303 (2012).

[131] E. Kammann et al., "Nonlinear optical spin Hall effect and long-range spin transport in polariton lasers", Phys. Rev. Lett. **109**, 036404 (2012).

[132] D. W. Snoke, G. Liu, and S. M. Girvin, "The basis of the second law of thermodynamics in quantum field theory," Ann. Phys., 2012.

[133] D.W. Snoke, *Essential Concepts of Solid State Physics*, (Addison-Wesley, 2009).

[134] G. Baym, *Lectures on Quantum Mechanics*, (Benjamin Cummings, 1969).

[135] For a review of experimental uses of the quantum Boltzmann equation, see D.W. Snoke, Ann. der Physik **523**, 87 (2011).

[136] D.W. Snoke, D. Braun, and M. Cardona, Phys. Rev. B **44**, 2991 (1991).

[137] E.g., H.-P. Breuer and F. Petruccione, *The Theory of Open Quantum Systems*, (Oxford University Press, 2002), p. 148.